



# **NAVAL POSTGRADUATE SCHOOL**

**MONTEREY, CALIFORNIA**

## **THESIS**

**INTER-ANNUAL VARIABILITY OF THE CALIFORNIA  
CURRENT SYSTEM AND ASSOCIATED  
BIOCHEMICAL CHARACTERISTICS FROM  
PROLONGED DATA SERIES**

by

DyAnna L. Rodriguez

June 2016

Thesis Advisor:  
Co-Advisor:

Peter C. Chu  
Tetyana Margolina

**Approved for public release; distribution is unlimited**

THIS PAGE INTENTIONALLY LEFT BLANK

<b>REPORT DOCUMENTATION PAGE</b>			<i>Form Approved OMB No. 0704-0188</i>	
Public reporting burden for this collection of information is estimated to average 1 hour per response, including the time for reviewing instruction, searching existing data sources, gathering and maintaining the data needed, and completing and reviewing the collection of information. Send comments regarding this burden estimate or any other aspect of this collection of information, including suggestions for reducing this burden, to Washington headquarters Services, Directorate for Information Operations and Reports, 1215 Jefferson Davis Highway, Suite 1204, Arlington, VA 22202-4302, and to the Office of Management and Budget, Paperwork Reduction Project (0704-0188) Washington, DC 20503.				
<b>1. AGENCY USE ONLY</b> (Leave blank)		<b>2. REPORT DATE</b> June 2016		<b>3. REPORT TYPE AND DATES COVERED</b> Master's thesis
<b>4. TITLE AND SUBTITLE</b> INTER-ANNUAL VARIABILITY OF THE CALIFORNIA CURRENT SYSTEM AND ASSOCIATED BIOCHEMICAL CHARACTERISTICS FROM PROLONGED DATA SERIES			<b>5. FUNDING NUMBERS</b>	
<b>6. AUTHOR(S)</b> DyAnna L. Rodriguez				
<b>7. PERFORMING ORGANIZATION NAME(S) AND ADDRESS(ES)</b> Naval Postgraduate School Monterey, CA 93943-5000			<b>8. PERFORMING ORGANIZATION REPORT NUMBER</b>	
<b>9. SPONSORING / MONITORING AGENCY NAME(S) AND ADDRESS(ES)</b> N/A			<b>10. SPONSORING / MONITORING AGENCY REPORT NUMBER</b>	
<b>11. SUPPLEMENTARY NOTES</b> The views expressed in this thesis are those of the author and do not reflect the official policy or position of the Department of Defense or the U.S. Government. IRB Protocol number ____ N/A ____.				
<b>12a. DISTRIBUTION / AVAILABILITY STATEMENT</b> Approved for public release; distribution is unlimited			<b>12b. DISTRIBUTION CODE</b>	
<b>13. ABSTRACT (maximum 200 words)</b> <p>This research investigates the California Current System (CCS) utilizing Synoptic Monthly Gridded World Ocean database (SMG-WOD) for temperature and salinity profiles, MODIS-A for surface chlorophyll-a (Chl-a) concentration, and climatological indices El Nino Modoki Index (EMI) and Multivariate El Nino Southern Oscillation Index (MEI), to compare inter-annual variations. The SMG-WOD produces 3D gridded fields with 1°×1° horizontal resolution and 28 vertical layers. The area of interest was 0°–54°N, 165°W–105°W from January 1945–December 2014. Because processes within 50 km of the coast are not well resolved by SMG-WOD, Chl-a data from MODIS-A with a 4.6 km resolution was used from July 2002–December 2014. Acceleration potential at the isopycnal surface of <math>\sigma_{\theta} = 26.9 \text{ kg/m}^3</math> relative to the 1000 dbar was calculated from the SMG-WOD. Composite and Empirical Orthogonal Function (EOF) analysis was conducted to identify patterns of maximum variance. Correlation coefficients were calculated to determine connections between inter-annual variability and EMI/MEI. Acceleration potential had small seasonal variability, while Chl-a concentration demonstrated large seasonal variability. When Principal Component (PC) 1 is positive, EMI index will be negative, resulting in an increased geostrophic flow in the CCS. For positive PC2, MEI is negative resulting in an offshore flow and thus enhanced coastal upwelling in the CCS. Positive PC1 correspond to negative EMI/MEI and elevated surface Chl-a concentration in the CCS.</p>				
<b>14. SUBJECT TERMS</b> California Current, inter-annual variability, acceleration potential, World Ocean Database (WOD), synoptic monthly gridded WOD (SMG-WOD), optimal spectral decomposition (OSD), composite analysis, empirical orthogonal function (EOF), climatological indices, El Nino Modoki Index (EMI), multivariate ENSO Index (MEI), MODIS-A, surface chlorophyll-a concentration			<b>15. NUMBER OF PAGES</b> 129	
			<b>16. PRICE CODE</b>	
<b>17. SECURITY CLASSIFICATION OF REPORT</b> Unclassified	<b>18. SECURITY CLASSIFICATION OF THIS PAGE</b> Unclassified	<b>19. SECURITY CLASSIFICATION OF ABSTRACT</b> Unclassified	<b>20. LIMITATION OF ABSTRACT</b> UU	

THIS PAGE INTENTIONALLY LEFT BLANK

**Approved for public release; distribution is unlimited**

**INTER-ANNUAL VARIABILITY OF THE CALIFORNIA CURRENT SYSTEM  
AND ASSOCIATED BIOCHEMICAL CHARACTERISTICS FROM  
PROLONGED DATA SERIES**

DyAnna L. Rodriguez  
Lieutenant, United States Navy  
B.S., United States Naval Academy, 2008

Submitted in partial fulfillment of the  
requirements for the degree of

**MASTER OF SCIENCE IN METEOROLOGY AND PHYSICAL  
OCEANOGRAPHY**

from the

**NAVAL POSTGRADUATE SCHOOL  
June 2016**

Approved by: Peter C. Chu, Ph.D.  
Thesis Advisor

Tetyana Margolina, Ph.D.  
Co-Advisor

Peter C. Chu, Ph.D.  
Chair, Department of Oceanography

THIS PAGE INTENTIONALLY LEFT BLANK

## ABSTRACT

This research investigates the California Current System (CCS) utilizing Synoptic Monthly Gridded World Ocean database (SMG-WOD) for temperature and salinity profiles, MODIS-A for surface chlorophyll-a (Chl-a) concentration, and climatological indices El Nino Modoki Index (EMI) and Multivariate El Nino Southern Oscillation Index (MEI), to compare inter-annual variations. The SMG-WOD produces 3D gridded fields with  $1^{\circ} \times 1^{\circ}$  horizontal resolution and 28 vertical layers. The area of interest was  $0^{\circ}$ – $54^{\circ}$ N,  $165^{\circ}$ W– $105^{\circ}$ W from January 1945–December 2014. Because processes within 50 km of the coast are not well resolved by SMG-WOD, Chl-a data from MODIS-A with a 4.6 km resolution was used from July 2002–December 2014. Acceleration potential at the isopycnal surface of  $\sigma_{\theta} = 26.9 \text{ kg/m}^3$  relative to the 1000 dbar was calculated from the SMG-WOD. Composite and Empirical Orthogonal Function (EOF) analysis was conducted to identify patterns of maximum variance. Correlation coefficients were calculated to determine connections between inter-annual variability and EMI/MEI. Acceleration potential had small seasonal variability, while Chl-a concentration demonstrated large seasonal variability. When Principal Component (PC) 1 is positive, EMI index will be negative, resulting in an increased geostrophic flow in the CCS. For positive PC2, MEI is negative resulting in an offshore flow and thus enhanced coastal upwelling in the CCS. Positive PC1 correspond to negative EMI/MEI and elevated surface Chl-a concentration in the CCS.

THIS PAGE INTENTIONALLY LEFT BLANK



# TABLE OF CONTENTS

<b>I.</b>	<b>INTRODUCTION.....</b>	<b>1</b>
<b>A.</b>	<b>MILITARY RELEVANCE.....</b>	<b>4</b>
<b>B.</b>	<b>THESIS ORGANIZATION.....</b>	<b>5</b>
<b>II.</b>	<b>OCEANOGRAPHY.....</b>	<b>7</b>
<b>A.</b>	<b>OCEANOGRAPHY OF CALIFORNIA CURRENT SYSTEM.....</b>	<b>7</b>
<b>B.</b>	<b>INTER-ANNUAL AND NON-SEASONAL VARIABILITY OF THE CALIFORNIA CURRENT SYSTEM.....</b>	<b>15</b>
<b>III.</b>	<b>DATA AND METHODOLOGY .....</b>	<b>23</b>
<b>A.</b>	<b>DATA .....</b>	<b>23</b>
1.	World Ocean Database Hydrographic Data .....	23
2.	Optimal Spectral Decomposition.....	29
3.	Chlorophyll-a Concentration Data.....	30
4.	Climatological Indices .....	32
5.	Multivariate El Nino/Southern Oscillation Index.....	32
6.	El Nino Modoki Indices .....	34
<b>B.</b>	<b>METHODOLOGY .....</b>	<b>40</b>
1.	Acceleration Potential at the Isopycnal Surface 26.9 kg/ m <sup>3</sup> for the SMG-WOD.....	40
2.	Composite Analysis.....	43
3.	Empirical Orthogonal Function Analysis.....	44
4.	Pearson Correlation Coefficient .....	45
<b>C.</b>	<b>MATLAB CODES .....</b>	<b>49</b>
<b>IV.</b>	<b>RESULTS AND DISCUSSION .....</b>	<b>53</b>
<b>A.</b>	<b>TOTAL TIME MEAN FOR ACCELERATION POTENTIAL (<math>\bar{\bar{\psi}}</math>).....</b>	<b>53</b>
<b>B.</b>	<b>CLIMATOLOGICAL MONTHLY ANOMALY FOR ACCELERATION POTENTIAL (<math>\tilde{\psi}</math>) .....</b>	<b>55</b>
<b>C.</b>	<b>EOF ANALYSIS FOR ACCELERATION POTENTIAL SYNOPTIC MONTHLY ANOMALY (<math>\hat{\psi}</math>).....</b>	<b>58</b>
<b>D.</b>	<b>CORRELATIONS BETWEEN PRINCIPAL COMPONENTS AND CLIMATOLOGICAL INDICES.....</b>	<b>64</b>
<b>E.</b>	<b>COMPOSITE ANALYSIS FOR CHLOROPHYLL-A CONCENTRATION.....</b>	<b>65</b>

F.	TOTAL TIME MEAN FOR CHLOROPHYLL-A CONCENTRATION ( $\bar{C}$ ).....	67
G.	CLIMATOLOGICAL MONTHLY MEAN FOR CHLOROPHYLL-A ( $\bar{C}$ ).....	70
H.	CLIMATOLOGICAL MONTHLY ANOMALY FOR CHLOROPHYLL-A CONCENTRATION ( $C$ ).....	75
I.	EOF ANALYSIS FOR CHLOROPHYLL-A CONCENTRATION SYNOPTIC MONTHLY ANOMALY ( $\hat{C}$ ).....	80
J.	CORRELATIONS BETWEEN PRINCIPAL COMPONENT 1 AND CLIMATOLOGICAL INDICES.....	83
V.	CONCLUSION .....	87
APPENDIX A. CLIMATOLOGICAL MONTHLY ANOMALY FOR ACCELERATION POTENTIAL ( $\tilde{\psi}$ ) MONTHS JANUARY– DECEMBER (1945–2014).....		93
APPENDIX B. CLIMATOLOGICAL MONTHLY MEAN FOR CHLOROPHYLL-A CONCENTRATION ( $\bar{C}$ ) MONTHS JANUARY– DECEMBER (2002–2014).....		97
APPENDIX C. CLIMATOLOGICAL MONTHLY ANOMALY FOR CHLOROPHYLL-A CONCENTRATION ( $C$ ) MONTHS JANUARY– DECEMBER (2002-2014). ....		101
LIST OF REFERENCES .....		105
INITIAL DISTRIBUTION LIST .....		111

## LIST OF FIGURES

Figure 1.	California Current System and Seasonal Variations. Adapted from Shanks and Eckert (2005). .....	8
Figure 2.	Currents of the California Current System. Source: Bennett (2016). .....	11
Figure 3.	Seasonal Representation of Atmospheric Sea Level Pressure. Source: Reid et al. (1958). .....	12
Figure 4.	Graphical Representation of Coastal Upwelling. Source: Roughgarden et al. (1988). .....	14
Figure 5.	Pacific Decadal Oscillation and North Pacific Gyre Oscillation Comparison of Upwelling. Source: Chhak and Di Lorenzo (2007). .....	17
Figure 6.	Anomalous Sea Surface Temperature during El Nino. Source: Weng et al. (2009). .....	19
Figure 7.	Anomalous Sea Surface Temperature during El Nino Modoki. Source: Weng et al. (2009). .....	20
Figure 8.	Averaged Global El Nino Continental Surface Temperatures. Source: JAMSTEC (2016). .....	36
Figure 9.	Averaged Global El Nino Modoki Continental Surface Temperatures. Source: JAMSTEC (2016). .....	37
Figure 10.	Averaged Global El Nino Modoki Rain Fall. Source: JAMSTEC (2016). .....	38
Figure 11.	Averaged Global El Nino Rain Fall. Source: JAMSTEC (2016). .....	39
Figure 12.	Time Series of El Nino Modoki and Multivariate El Nino Index. ....	40
Figure 13.	Graphical Depiction of Acceleration Potential. Source: McDougall (1989). .....	42
Figure 14.	Total Time Mean for Acceleration Potential at the $26.9 \text{ kg/m}^3$ Isopycnal Surface ( $\bar{\psi}$ ). .....	54
Figure 15.	Climatological Monthly Anomaly for Acceleration Potential ( $\tilde{\psi}$ ) (1945–2014). .....	57

Figure 16.	EOF Mode 1 and Mode 2 from Acceleration Potential Synoptic Monthly Anomaly ( $\hat{\psi}$ ).	60
Figure 17.	EOF Analysis of PC1 and PC2 from Acceleration Potential Synoptic Monthly Anomaly ( $\hat{\psi}$ ).	62
Figure 18.	Raw Chl-a Concentration Data for July 2002.	66
Figure 19.	Interpolated Chl-a Concentration Data for July 2002.	67
Figure 20.	Total Time Mean for Chl-a ( $\bar{\bar{C}}$ ) (2002-2014).	68
Figure 21.	Climatological Monthly Mean for Chl-a Concentration ( $\bar{C}$ ) (2002–2014).	71
Figure 22.	Climatological Monthly Anomaly for Chl-a Concentration ( $C$ ) (2002–2014).	76
Figure 23.	EOF Analysis of Mode 1 and Mode 2 from Chl-a Concentration Synoptic Monthly Anomaly ( $\hat{C}$ ).	81
Figure 24.	Principal Components of Synoptic Monthly Anomaly for Chl-a Concentration ( $C$ ).	83

## LIST OF TABLES

Table 1.	Instrument Types in the WOD. Adapted from Boyer et al. (2013). ....	25
Table 2.	Data Sources of WOD. Adapted from Boyer et al. (2013). ....	26
Table 3.	Depth Layers in SMG-WOD. ....	28
Table 4.	Absolute Value Correlation Coefficient. Adapted from Huntsberger et al. (1973). ....	46
Table 5.	Notation Table for Reference to Data Calculations. ....	47
Table 6.	Variances of the First Six Leading EOFs of Synoptic Monthly Anomaly ( $\hat{\psi}$ ). ....	59
Table 7.	Variances of the First Six Leading EOF's of Synoptic Monthly Anomaly ( $\hat{C}$ ). ....	80

THIS PAGE INTENTIONALLY LEFT BLANK

## **LIST OF ACRONYMS AND ABBREVIATIONS**

CC	California Current
CCS	California Current System
Chl-a	Chlorophyll-a Concentration
CU	California Undercurrent
DC	Davidson Current
EMI	El Nino Modoki Index/ Pseudo El Nino
ENSO	El Nino Southern Oscillation
MEI	Multivariate ENSO index
NCEI	National Centers for Environmental Information
NOAA	National Oceanic and Atmospheric Administration
NODC	NOAA National Oceanographic Data Center
OSD	Optimal Spectral Decomposition
PDO	Pacific Decadal Oscillation
PC	Principal Component
SMG	Synoptic monthly mean gridded
WOA	World Ocean Atlas
WOD	World Ocean Database

THIS PAGE INTENTIONALLY LEFT BLANK



## **ACKNOWLEDGMENTS**

This research would not have been possible without the support and guidance of my advisors, Professor Peter C. Chu and Dr. Tetyana Margolina. Thank you for your genuine compassion, support, and motivation. I will never forget our professional and personal relationship developed over the past year.

THIS PAGE INTENTIONALLY LEFT BLANK

## I. INTRODUCTION

This research seeks to identify, and explain inter-annual variability within the California Current System (CCS), using long-term series of monthly temperature and salinity fields, as well as monthly composites of remotely sensed chlorophyll-a concentration (Chl-a). In addition, two climatological indices are used to relate the patterns of the CCS inter-annual variability to El Nino Southern Oscillation (ENSO) and El Nino Modoki. While the influence of ENSO onto the eastern north Pacific circulation has been studied for years, the effect of El Nino Modoki in the region is still unclear.

The CCS is located in the eastern region of the North Pacific Gyre. The anticyclonic North Pacific Gyre extends across the entire Pacific Ocean basin from the North America to Japan. The northern eastward propagating current of the North Pacific Gyre is the North Pacific Current. As the North Pacific Current approaches the west coast of North America it branches north, as the Alaska Current and south as the California Current (CC) (Hickey 1979). The Alaska Current turns north and becomes part of the cyclonic Alaska Gyre. The CC moves southward along the west coast of North America and Baja California, Mexico, until it turns west and becomes the North Equatorial Current (Hickey 1979; Douglass et al. 2006). The CCS is comprised of three currents the CC, the California Undercurrent (CU), and the seasonal Davidson Current (DC). The CC is 300 km from the coast and moves subpolar waters toward the equator it is characterized by cold temperatures, low salinity, high dissolved oxygen, and is rich in nutrients (Hickey 1979). The CCS is driven by two main synoptic forcing patterns of pressure gradients and winds that consequently influence the surface waters. Pressure gradients in the region are set by a semi-permanent high pressure system, over central north Pacific, and a continental thermal low over North America (Talley et al. 2011; Reid et al. 1958). The location and intensity of the high- and low-pressure systems vary throughout the year creating a strengthening pressure gradient in the summer and a weak pressure gradient in the winter. There are two bands of the CC, nearshore and offshore. These bands appear throughout the year and are identified by their velocities and water properties. The nearshore band is located within 125 km of the coast and the offshore band is centered approximately 425 km from the coast

(Hickey 1979). The intensity of the bands is dependent on season and geographic location in relation to the coastline (Hickey 1979). The CU is a subsurface current approximately 200 m below the surface and moves tropical waters northward toward the poles (Hickey 1979). It is characterized by warmer temperatures, high salinity, low dissolved oxygen, and few nutrients (Hickey 1979). The DC is a seasonal current that is present during the winter. As an expression of the CU at the surface it exhibits many of the same water property characteristics as the CU (Hickey 1979).

The CCS and its forcing have seasonal variation. In the summer, the region is influenced by predominantly northwesterly winds and the pressure gradient tightens as the high pressure migrates toward the coast and the thermal low intensifies as a result of the increased solar heating of the continent. This gives rise to increased coastal upwelling as a result of Ekman transport and subsequently biological production and increased surface Chl-a (King et al. 2011). In the winter, the predominant wind pattern is southwesterly and the pressure gradient weakens (Hickey 1979). During the winter the high- and low-pressure system has lessened intensity and moved farther offshore that then decreases the coastal upwelling, and in some coastal regions upwelling has ceased and downwelling is the predominate circulation. In addition, the inshore band of the CC has decreased velocity or completely dissipated allowing for the CU to rise to the surface becoming the DC (Hickey 1979).

Other forms of variability on the CCS are inter-annual variability, and this is the focus of this research, specifically Pacific Decadal Oscillation (PDO), El Nino, El Nino Modoki, and North Pacific Gyre Oscillation (NPGO). PDO is a non-seasonal oscillation of the CCS and has an inter-decadal period of approximately 10 years (Mantua et al. 1997). El Nino is characterized by warmer than normal sea surface temperatures that transition from the eastern tropical Pacific to central tropical Pacific. PDO and El Nino are both more evident in the winter and impact the CCS with increased surface temperatures, increased precipitation resulting from the predominant southwesterly winds that relax coastal upwelling leading to more prevalent downwelling and decreased Chl-a (Mantua et al. 1997). PDO and El Nino signatures in the CCS can be similar spatially and temporally and difficult to differentiate. El Nino Modoki is characterized with colder than normal sea

surface temperatures in the east and west tropical Pacific and warmer than normal temperatures in central tropical Pacific. El Nino Modoki was first identified in 2004 by a Japanese researcher who coined the term “Modoki,” which means “similar but different” (Ashok et al. 2007). The impacts of El Nino Modoki to the CCS are not well known but share some characteristics with NPGO. NPGO is characterized by increasing northwesterly winds and increased coastal upwelling in the CCS and consequently increased Chl-a (Di Lorenzo et al. 2008).

The data sets analyzed in this research to identify potential variability were Synoptic Monthly Gridded-World Ocean Database (SMG-WOD) for temperature and salinity profile data, Moderate Resolution Imaging Spectroradiometer (MODIS) that is an instrument deployed on Aqua satellite (A) for surface Chl-a data (MODIS-A), Multivariate El Nino Southern Oscillation Index (MEI), and El Nino Modoki Index (EMI). The SMG-WOD is a product of the World Ocean Database (WOD) and is the world’s largest collection of free oceanographic data (Boyer et al. 2013). SMG-WOD was developed at Naval Postgraduate School and applies Optimal Spectral Decomposition (OSD) based on Fourier series expansion (Chu and Fan 2016). The SMG-WOD allows for investigation of long-term spatial and temporal variability of the CCS with a  $1^{\circ} \times 1^{\circ}$  horizontal resolution and 28 vertical layers (Chu et al. 2003a, b; 2004; 2015). The dataset is stored on the National Oceanic and Atmospheric Administration (NOAA) National Center for Environmental Information (NCEI) (NOAA/NCEI WOD) for public use (Chu and Fan 2016). For this research the region of the CCS [ $0^{\circ}$ – $54^{\circ}$ N,  $165^{\circ}$ W– $105^{\circ}$ W] was extracted from January 1945 to December 2014. SMG-WOD has a limiting factor of horizontal resolution near the coastline. In order to resolve the coastal features of the CCS, surface Chl-a data from MODIS-A was accessed. MODIS-A data provides a comprehensive global ocean bio-optical and biochemical properties (MODIS 2016; Hu 2012). The data is captured in 36 spectral bands and then composited over the span of multiple days and averaged into a monthly product, which is available for public use (MODIS 2016). The product is 4.6 km resolution of surface Chl-a concentration in mg/m<sup>3</sup> obtained from July 2002 to December 2014. One limiting factor of using satellite acquired data is sensitivity to environmental factors. The impacts to this research include the region north of  $45^{\circ}$ N is

blanked in all years from November to February as a result of winter and increased cloud, snow, and sea ice that limited the availability to measure the surface Chl-a (Hu 2012). Climatological indices are used in this research to explain the inter-annual variability of the CCS. Multivariate El Nino Southern Oscillation Index (MEI) is obtained from six observed variables and indicates ENSO oscillation patterns (Jacox et al. 2015; Ashok et al. 2007). El Nino Modoki Index (EMI) is calculated from different sea surface temperature anomalies in three regions: the east, west, and central tropical Pacific. The index characterizes El Nino Modoki oscillation patterns (Ashok et al. 2007).

Methodology to analyze the data was statistical analysis of the temperature and salinity data from the SMG-WOD, Chl-a from MODIS-A, and MEI/EMI climatological indices. For temperature and salinity data acceleration potential ( $\psi$ ) was calculated at the 26.9 kg/m<sup>3</sup> isopycnal surface to analyze the spatial the temporal variability for the CCS. The 26.9 kg/m<sup>3</sup> isopycnal surface may outcrop north of 54°N and defines the northernmost boundary. EOF is a statistical analysis method used when interested in finding a set of patterns that capture the maximum variance. It separates the temporal and spatial scales. A correlation coefficient were calculated between the acceleration potential ( $\psi$ ) fields, Chl-a concentration ( $C$ ) fields produced from the composite analysis and compared to the MEI and EMI climatological patterns.

#### **A. MILITARY RELEVANCE**

The eastern north Pacific is home to the United States Navy's Third Fleet. The Third Fleet encompasses the area from Washington south to California, west to Hawaii, and all the ocean in-between to include the CCS. This region is not a warfighting maritime domain, but it is the heart of all training for the West Coast Navy and is responsible for ensuring that the sea-going fleet is ready for combat. The main mission of Third Fleet is to provide safe, effective, relevant training to ensure Sailors have the essential skills to stimulate peace and succeed in combat (Third Fleet 2016). This is accomplished through multinational exercises such as Pacific Partnership, Fleet Weeks and Rim of the Pacific that are conducted throughout the year. Third Fleet is home to five carrier strike groups each consisting of a combination of cruisers, destroyers, frigates, submarines, supply ships, air

forces including F/A-18 Super Hornets, E-2C Hawkeyes, AV8B Harriers, AH-1z SuperCobras, and SH-60 Seahawks force, all of which will participate in the multinational exercises and most importantly expected to deploy across the globe at a moment's notice (Third Fleet 2016). The planning and manpower needed to implement large scale operations takes years of planning, and can cost the tax payers an incredible amount of money. Being able to plan months in advance is critical, especially in the early and mid-stages of development of an exercise of this magnitude. This research of the CCS is vital to the long-range outlook of large scale naval exercises within the Third Fleet. Understanding our environment and ocean currents within the CCS improves the Navy's ability to practice operating safely and effectively along our coastal waters and operational areas. This is accomplished by determining the long range impacts to inter-annual climatological patterns. The impact to the United States Navy is the ability to enrich the military community with cutting edge research providing military commanders, emergency managers, decision makers, and operational coordinators, with reliable information to make informed decisions without question, especially when the situation deals with predicting impacts of an infrequent and hard to predict environmental events, such as El Nino. Furthermore, it prevents the occurrence of modifications to operations and can save the military money in preventing exercises from getting canceled or shuffled around. Ultimately, it strengthens the ability to protect military interests of the United States and the allied partners who participate in the multinational exercises (Third Fleet 2016).

## **B. THESIS ORGANIZATION**

In Chapter II, oceanography of the CCS includes synoptic forcing and impacts, water mass characteristics, seasonal and inter-annual variability, and the impacts to the three associated currents. In Chapter III, information about the datasets used as well as the location of public accessible websites is studied. Methodology will also be detailed, along with all relevant equations. In Chapter IV, results are outlined and discussed in relation to inter-annual variability for both acceleration potential and Chl-a concentration using correlation coefficients. Chapter V contains a summary of findings and future work.

THIS PAGE INTENTIONALLY LEFT BLANK



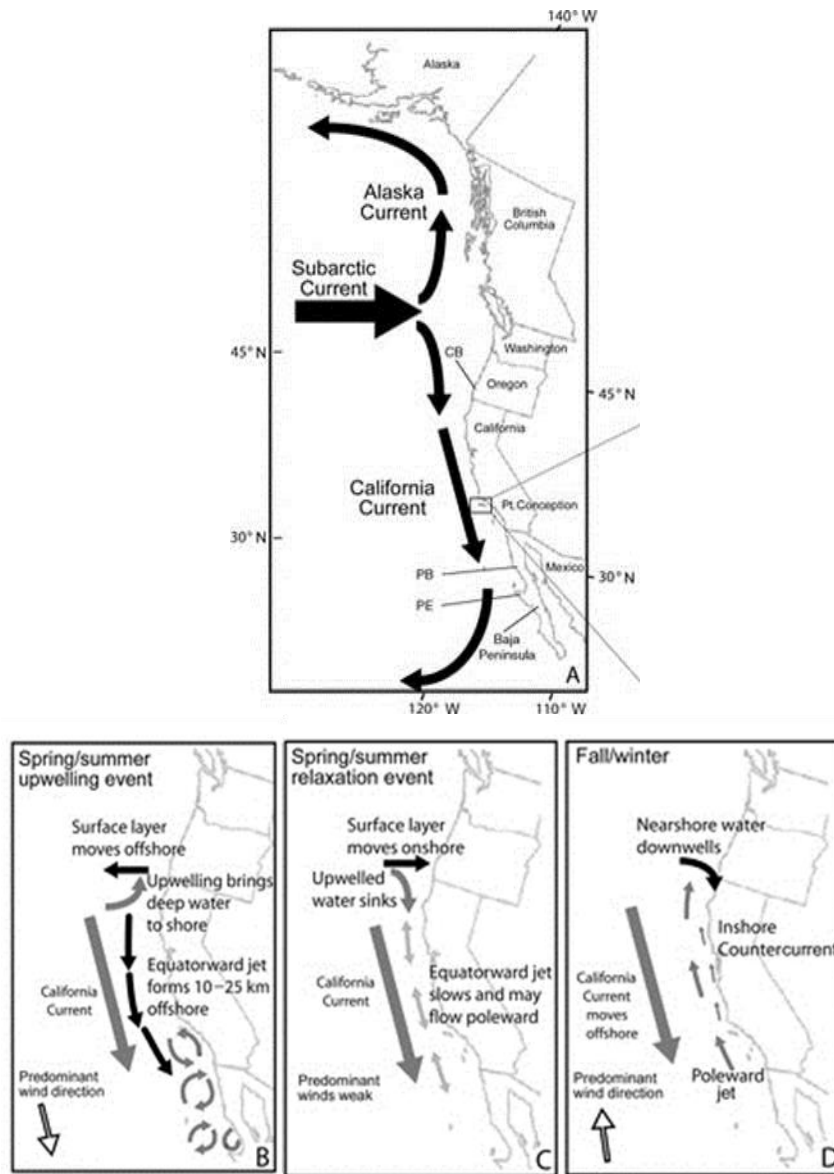
## **II. OCEANOGRAPHY**

### **A. OCEANOGRAPHY OF CALIFORNIA CURRENT SYSTEM**

In order to identify variability within the California Current System (CCS) it is crucial to understand the seasonal evolution and environmental forces (including winds) that drive the circulation. The CCS is located in the Eastern North Pacific and is considered the southward flow of the anticyclonic North Pacific Gyre and it is a vastly studied and region of the Pacific Ocean (Reid 1958). The CCS is greatly influenced by the coastline of western North America and is considered an eastern boundary current. The northern boundary of the current is approximately 45°N where the eastward propagating North Pacific Current approaches North America and branches in two directions, north separating the Alaska Current and the cyclonic Alaska Gyre from the North Pacific to the south this area is also known as the Transition Zone. The southward propagating branch of the North Pacific Gyre is where the CCS begins. The CCS flows southward toward the equator along the coast of North America and Baja California, Mexico, to the southern boundary of 15°N (Hickey 1979; Douglass et al. 2006). At the southern boundary of the CCS the current turns westward and becomes part of the cyclonic Pacific North Equatorial Current. In the CCS, the region nearest the coast typically experiences the greatest fluctuation of seasonal variability. On average the current is approximately, 1000 km from shore and relatively shallow in depth at 400 m and has an average flow rate of less than 25 cm/s but have been observed as high as 50 cm/sec by drifters (Reid 1965; Reid and Schwartzlose 1962; Reid et al. 1958; Davis 1985).

The CCS is not as simple as a continuous flow of equatorward subarctic water; it is a complex multifaceted system that is highly variable, and largely driven by seasonal wind fluctuations. The main features of the CCS includes other sub-currents, the equatorward (southward) flow of the California Current (CC), the California Undercurrent (CU) that is a subsurface poleward (northward) propagating current near the continental slope, and the Davidson Current (DC) that is also a poleward (northward) current that occurs seasonally during the winter and fall near and north of Point Conception, see Figure 1 (Hickey 1979; King et al. 2011; Davis 1985; Sverdrup and Flemming 1941).

Figure 1. California Current System and Seasonal Variations. Adapted from Shanks and Eckert (2005).



(A) The California Current System with the North Pacific Current approaching the West Coast of North America, the Alaska Current that feeds into the Alaska Gyre is the northward moving current along the West Coast of North America, and the southward moving current is the California Current that turns westward and near Baja California, Mexico. (B) The California Current has coastal upwelling circulation during spring and summer when the winds are strong and northwesterly. (C) In some conditions, coastal upwelling relaxes when northwesterly winds weaken. (D) In fall and winter, predominate winds are southwesterly and DC can be seen as an expression of the CU. This image was adapted from Shanks and Eckert (2005) images E, F, G, and H were not used.

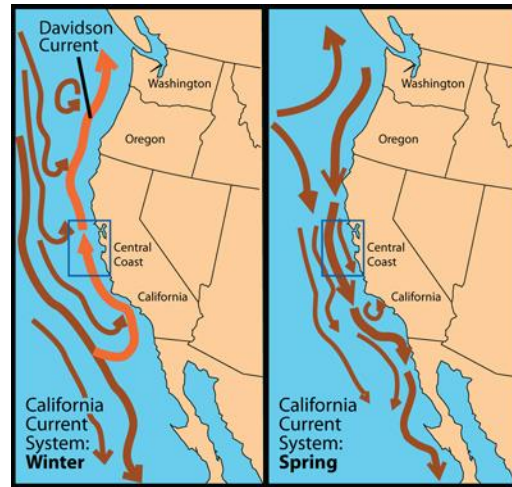
The CC is located approximately 300 km from the shore. It transports Pacific Subarctic water equatorward at velocities between 10–20 cm/sec, has low temperature and salinity, high in dissolved oxygen, and high in various nutrients. Due to the subarctic origin these waters typically make the coastal waters cooler. Another feature of the CC is the location of two distinct regions of southward propagating water, a nearshore flow and offshore flow (Hickey 1979). The two bands appear throughout the year and are identified by the apparent velocity intensifications. The nearshore band is located within 125 km of the coast and is more prevalent from February to October with the greatest velocities observed in April and May. The offshore band is generally wider and higher velocity than the inshore band. It is centered approximately 425 km from the coast from February to September and is strongest in August and September (late summer/fall). These bands within the CC will vary throughout the year in location and intensity depending on the geographical location and the season. The offshore region tends to migrate closer to the shore in the winter and can be as close as 200 km in January in some regions. The two bands are separated by a region of reduced velocity or potentially a reversal in direction to northward (Hickey 1979). However, there are periods where the nearshore flow is not present and this is during the fall and winter months. During the colder months, the nearshore flow can be replaced with a poleward propagating current, which is identified as the DC. This occurs most notably along the coast of California and Baja California, Mexico at differing times as the winter season develops. It is important to note that there are various counter-flows identified within the CC but primarily at the inshore region. The counter-flow can replace or displace the southward propagation and typically is observed north of Point Conception during the fall and winter seasons, and near Baja California, Mexico the counter-flow can occur in the fall and near the California Bight during fall, winter, and summer (Hickey 1979).

The CU is a subsurface current that transports Equatorial Pacific water at an average velocity of 10 cm/sec within 150 km of the coast and at a depth between 300–500 m, below the pycnocline and west of the continental slope (Hickey 1979). The CU is characterized by high temperature and salinity and phosphate and low dissolved oxygen and nutrients. The equatorial waters have been identified as far north as Washington State

but the intensity and signatures of the CU tend to dissipate as the current propagates to the north and toward the west (seaward) (Castro et al. 2001; Hickey 1979). The weakest flow occurs in March through May and only Point Conception has observed the CU in all seasons. The maximum flow intensity occurs in the summer through fall. When the flow of the CU increases it typically will reach the surface and is referred to as the DC (Hickey 1979).

The DC phenomenon is characterized by poleward flow in the nearshore regions of North America commonly observed north of Point Conception to approximately 48°N and confined around 80 km offshore. The DC is an expression of the CU as identified due to its similar water properties, however it only appears at the surface during the late fall and winter months (Pavlova 1966; Smith et al. 1976). The onset of the current is a result of weakening northerly winds, which can reverse to southerly or southwesterly in some locations, see Figure 2 (Hickey 1979; Reid et al. 1958). The winds reversal or weakening causes the coastal upwelling to relax and in turn reduces the suppression of the CU, which is present at the surface as the DC. However, the DC can occur during other seasons if the wind favors DC formation. The flow is typically weakest during the spring and is absent in April. The DC is strongest from November to January with a maximum velocity of 25 cm/sec. The arrival of the DC is observed by the drastic change in the change of the surface water properties from subarctic to equatorial origin (Hickey 1979).

Figure 2. Currents of the California Current System. Source: Bennett (2016).

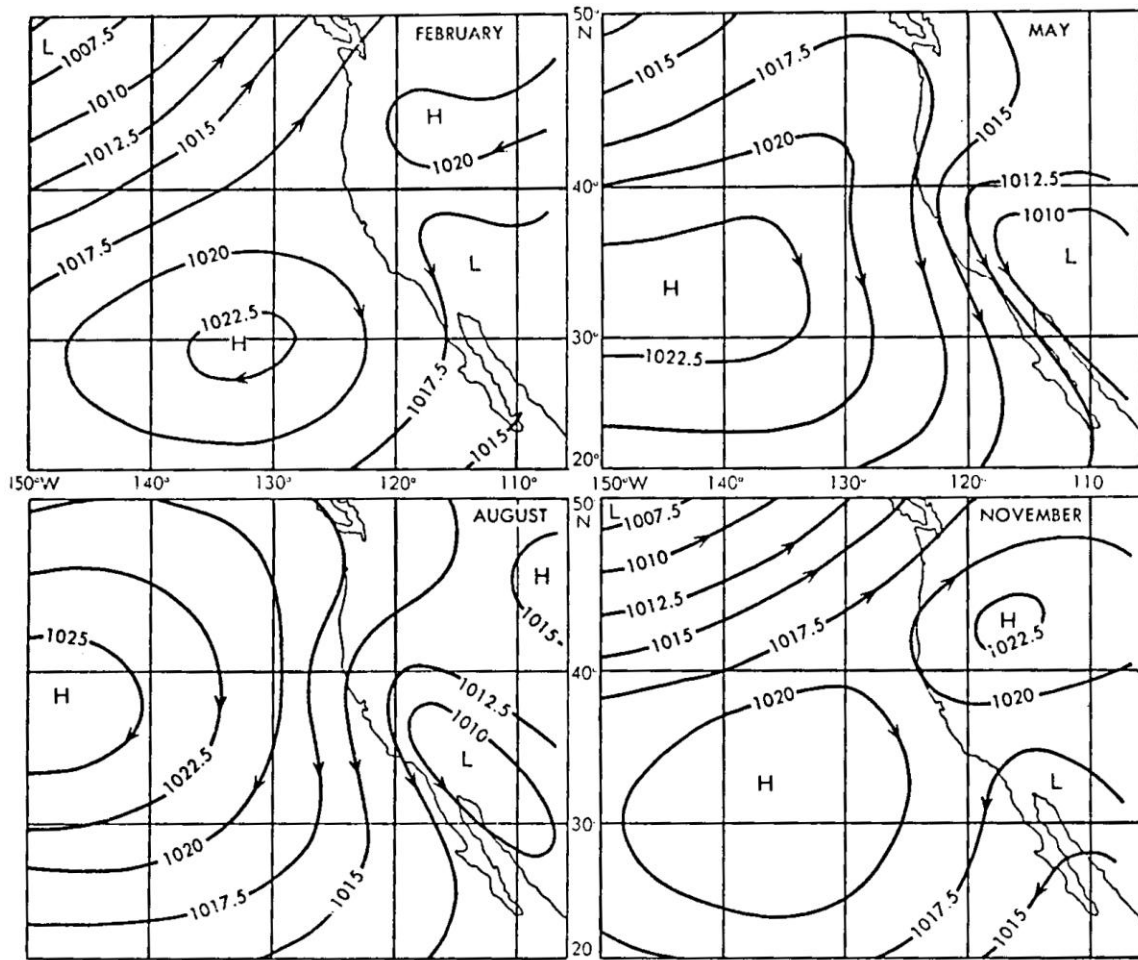


Left panel: The Davidson Current observed in the winter indicated with the orange arrows pointing poleward. Right panel: The California Current System during the spring indicated with the thick brown arrows pointing toward the equator (Bennett 2016).

The main forcing mechanism behind the CCS is atmospheric pressure and associated winds in addition to the coastline of Northern America. Figure 3 represents a seasonal chart of sea surface pressure within the vicinity of the CCS (Reid et al. 1958). The important feature to highlight is the strength of the pressure gradient between the semi-permanent North Pacific High and the continental thermal low over California (Hickey 1979). The thermal gradient is the main driving force for the surface winds in the region and the corresponding surface currents observed within the CCS (Hickey 1979). During the summer, August as depicted in Figure 3, the thermal low will deepen as the continental surface temperature increases with the intensifying solar radiation impacting the desert climate. In addition, during the summer months the North Pacific High migrates further to the west and intensifies, this creates a very strong gradient and the winds are generally northerly (toward the south) and strong (Hickey 1979). As the season progresses through fall, November as depicted in Figure 3, the continental thermal low weakens and the North Pacific High migrates toward the east (toward the shore) until winter, February as depicted in Figure 3, when the gradient is the weakest. The winds in fall are generally northerly but the intensity has lessened. In winter, the pattern is very different. The thermal continental low is very weak, as a result of minimal solar heating

and the North Pacific High migrates very close to the shore and is slightly more intense than as observed in fall. As a result of the decrease in the pressure gradient the northerly component of the winds will drastically weaken or reverse (Hickey 1979; Reid et al. 1958).

Figure 3. Seasonal Representation of Atmospheric Sea Level Pressure. Source: Reid et al. (1958).

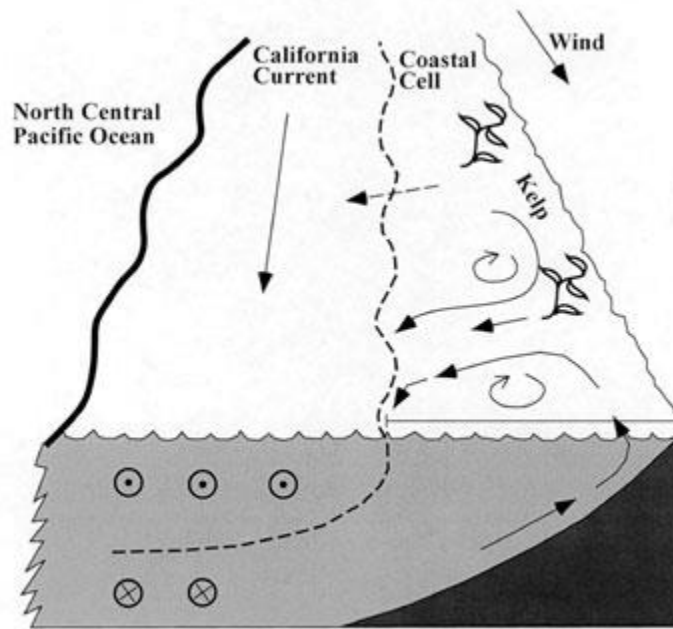


This figure shows the migration, development, and decay of the semi-permanent high-pressure system over the central Pacific and the continental thermal low pressure over California throughout the year. Upper left panel: February (winter season), Upper right panel: May (spring), Lower left panel: August (summer season), Lower right panel: November (fall season) (Reid et al. 1958).

The seasonal changes in location of the North Pacific High and the continental thermal low have a significant impact on the changes of the winds and concurrently on the surface currents. This is of particular importance for the CCS. When the region is influenced by the strong northerly winds, in combination with Coriolis force the surface waters are forced offshore, which is known as Ekman transport. As a result of the pressure gradient, geostrophic flow in the same direction as the wind (toward the equator) and Ekman transport the surface waters are removed from the coast and replaced with water from below the surface, and hence upwelling commences, see Figure 4 (Talley et al. 2011).

The coastal upwelling is a very important feature of the CCS because it brings to the surface waters that are rich in nutrients, and the reason biological productivity in the CCS is so abundant. The upwelling is strongest when the winds are northerly, and hence during the summer when the pressure gradient is strongest the winds are also very intense producing significant upwelling. In addition to nutrients, the upwelled waters cool the surface waters more, that contributes to the mild summers experienced near the coast where upwelling is strongest. The regions of upwelling are not uniform along the entire West Coast of North America. In southern regions, upwelling is stronger in spring, due to the increased surface temperature and the prolonged daytime heating as the season approaches summer, for example in Baja California, Mexico the coastal upwelling peaks in April and May. In northern regions, the upwelling is strongest in summer; for example, in southern and central California the upwelling peak is observed in May and June and off Oregon in August (Hickey 1979). Conversely, in the winter months, when the pressure gradient weakens, the winds weaken or reverse, so will the upwelling. As the upwelling relaxes during the winter months, when other CCS signatures are observed specifically, the DC develops as a surface expression of the CU (Hickey 1979).

Figure 4. Graphical Representation of Coastal Upwelling. Source: Roughgarden et al. (1988).



This figure represents coastal upwelling off the California coast in spring. The subsurface circles with dots represent poleward flow the circles with crosses represent equatorward flow. The dashed line separates the moving water masses and shows how the location of the California current can migrate near the coast (Roughgarden et al. 1988).

Seasonal variability and primary production within the CCS are linked to and based on the overall large scale wind patterns. Northwesterly winds produce the coastal upwelling. Primary production and Chl-a concentration are positively correlated, meaning when primary production is elevated the concentration of Chl-a will also be elevated (King et al. 2011). Primary production is also a function of the amount of nutrient resources available within the water column. Upwelled waters originate from nutrient rich subsurface waters; upon surfacing these waters are capable of sustaining increased primary production near the coast. Large amounts of upwelled water occur from February to September and as a result, primary production is very high (King et al. 2011). When primary production is high in oceanic systems during upwelling, the Chl-a concentration responds similarly. Conversely, when the upwelling is relaxed, during southerly winds or seasonally from November to February, the region will decrease in the primary production, and the Chl-a surface concentration will also decrease (King et al. 2011). The high-productive areas within the CCS are usually located where the upwelling



is supported for the majority of the year. In addition, the high productivity and greater Chl-a concentration is observed at higher latitudes as a result of increased seaward export of nutrients, enhanced upwelling, and elevated nutrients supply from land and river runoff. The correlation of primary production/Chl-a concentration to large-scale wind forcing variabilities has been shown in many studies. An example of such a correlation was observed during El Nino events (Thomas and Strub, 2001). In the significant 1957–1958 El Nino during the winter when the coastal surface temperatures transitioned from cool surface waters to the typical warm surface waters associated with El Nino a large decline in the primary production was observed (McGowan et al. 1998). This correlation has also been observed and studied for other strong El Nino events that have followed since particularly, 1977, 1989, and 1998 (King 2005). In general, primary production and Chl-a are sensitive and have a significant response to the variability within the CCS.

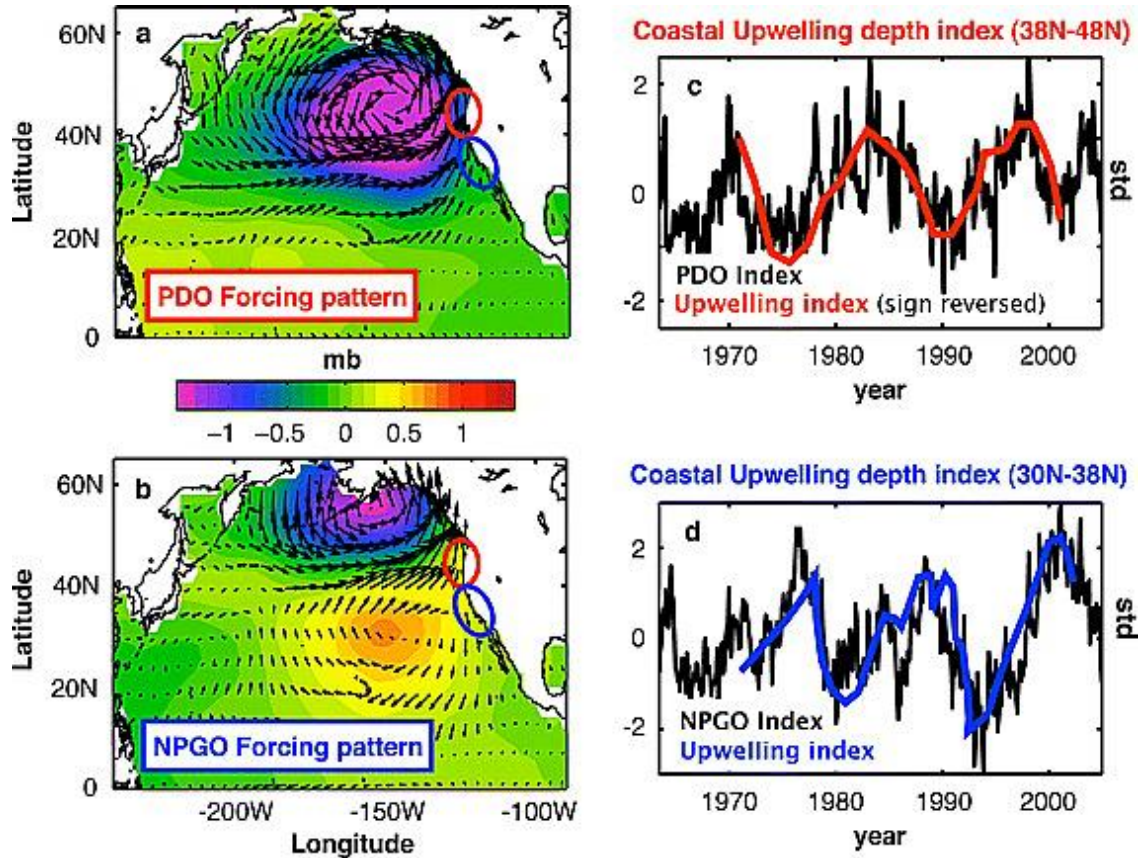
## **B. INTER-ANNUAL AND NON-SEASONAL VARIABILITY OF THE CALIFORNIA CURRENT SYSTEM**

The CCS is influenced not only by the atmospheric surface pressure and seasonal winds regimes but it is also greatly impacted by inter-annual, decadal and non-seasonal forcing. In this research we will focus on Pacific Decadal Oscillation (PDO), North Pacific Gyre Oscillation (NPGO), ENSO, and El Nino Modoki impacts specifically to the CCS.

For decadal time-scales the PDO is a part of large-scale climate variability (King et al. 2011). The PDO is a cycle that occurs on inter-decadal scale, around 1925, 1947, and 1977 (Mantua et al. 1997). Strengthening, north and south migration of the Aleutian Low pressure system primarily force PDO (Di Lorenzo 2008). The Aleutian Low pressure system is located in the North Pacific near the Alaskan Gulf and over the Aleutian Islands. During a positive phase of PDO the Aleutian Low system is stronger and displaced southward that reduces upwelling in the northern regions of the CCS and the Gulf of Alaska (Di Lorenzo 2008). In lieu of the upwelling that is characteristic of the CCS, the region can experience enhanced downwelling. Downwelling circulation induces costal convergence of water masses leading to higher than normal sea surface height and warmer than normal sea surface temperatures, see Figure 5 (King et al. 2011). As a result

of the higher sea surface height, the current will be directed poleward at the coastline from 25°N to 55°N and the CCS flow will weaken (Di Lorenzo 2008). The intensity of the upwelling season (spring and summer) is influenced by PDO but mostly in the northern regions of the CCS. The central North Pacific Ocean typically experiences sea surface temperature anomalies with a larger pool of cooler than average surface water (Mantua et al. 1997). In addition, near shore waters in the North Pacific will experience a warmer than average sea surface temperature. The signature of the PDO is most evident in the winter and is characterized by heavier than normal precipitation along the coast of Alaska, Washington, and Oregon (Mantua et al. 1997). This is as a result of the warmer ocean temperatures causing warm moist air in the region and increasing rainfall. The PDO and ENSO climate patterns are closely related spatially and temporally. This causes some confusion in differentiating PDO variability from ENSO variability (Mantua et al. 1997). How the PDO fluctuations impact biological variables remain unclear and may or may not impact the surface Chl-a concentration (Di Lorenzo et al. 2008).

Figure 5. Pacific Decadal Oscillation and North Pacific Gyre Oscillation  
Comparison of Upwelling. Source: Chhak and Di Lorenzo (2007).



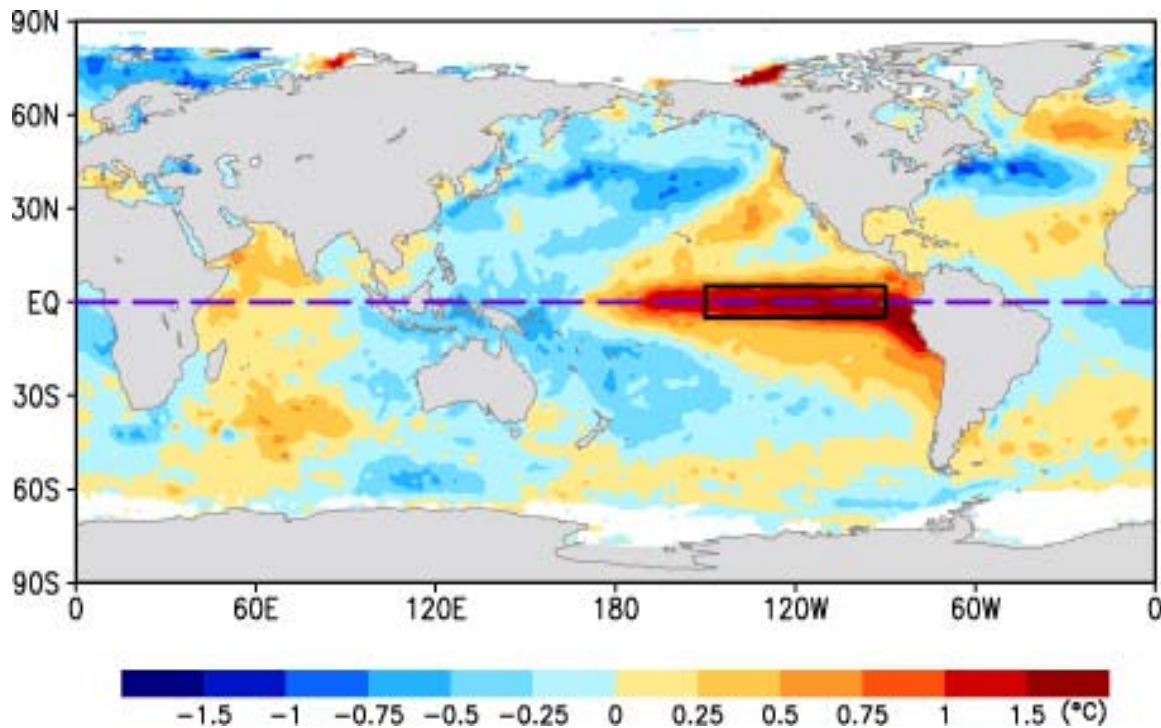
Images (a) and (b) depict wind strength (vectors) and the color bar indicates the sea level pressure in millibars. The warm colors indicate higher sea level pressure and cooler colors indicate lower sea level pressure. Picture (a) represents Pacific Decadal Oscillation and (b) represents North Pacific Gyre Oscillation. The associated coastal upwelling index is shown in (c) and (d). Where (c) shows upwelling depth index for Pacific Decadal Oscillation from 38°N to 48°N (red circle) and (d) is for the North Pacific Gyre Oscillation from 30°N to 38°N (blue circle). When the upwelling index is positive it represents stronger upwelling circulation (Chhak and Di Lorenzo 2007).

Another inter-decadal oscillation associated with the North Pacific is the NPGO. It is associated with changes in the sea surface height. Unlike PDO, it is forced by a change in the atmospheric sea level pressure with a north-south dipole pattern. In fact NPGO and PDO are statically independent from one another (King et al. 2011; Di Lorenzo et al. 2008). The dipole pattern changes the large-scale upwelling characteristics of the CCS. Specifically it influences the alongshore wind stress, which is the mechanism behind upwelling and increased nutrients at the surface. When the NPGO is positive it influences geostrophic circulation of the Alaskan Gyre and the North Pacific Subtropical

Gyre. Where the North Pacific Current diverges at the coast of North America into the Alaskan current, to the north, and the CC, to the south, the NPGO increases transport in all associated currents and gyres. In all regions of the CCS, the sea surface height decreases, increasing Ekman transport and consequently increasing upwelling along the coast. The effect of the more intense upwelling is observed south of 38°N (Mantua et al. 1997). In relation to the increased upwelling the fluctuation of decadal nutrients also increases, to include surface Chl-a concentration (Di Lorenzo et al. 2008). Thus, NPGO is a strong indicator of fluctuations in the mechanisms, which influence biological production. Interestingly, Di Lorenzo et al. (2008) observed strengthening of the NPGO mode since 2003, and correlated the response to anthropogenic forcing and global warming, and anticipated the dynamics driving NPGO to continue to influence the strength and frequency in the coming decades.

El Nino is a non-seasonal/inter-annual event characterized by weakening of the trade winds and in turn warming in the eastern equatorial Pacific that can extend through the central equatorial Pacific, see Figure 6. The signature of El Nino in the CCS is similar to PDO. El Nino predominantly impacts the winter season and the position of the Aleutian Low pressure system and is identified through atmospheric and oceanic forcing patterns (Jacox et al. 2015; Mantua et al. 1997). The CCS responses to El Nino are a strong depression in the thermocline, warming of the upper water layers, slowing of the current, and reduced biological productivity as a result of relaxed upwelling (Jacox et al. 2015). In addition, higher than normal precipitation and increased regional moisture content are observed in the winter season as a result of the warmer sea surface temperatures. The years associated with El Nino impacts are recorded back to the 1950s the top El Nino events since 1950 are 1957/1959, 1965/1966, 1972/1973, 1982/1983, 1986/1988, 1991/1993, 1997/1998, and the 1997/1998 being the strongest one as of now (Wolter and Timlin, 1998). The current, 2015/2016, is extremely strong and will be evaluated against the 1997/1998 when it is over.

Figure 6. Anomalous Sea Surface Temperature during El Nino. Source: Weng et al. (2009).

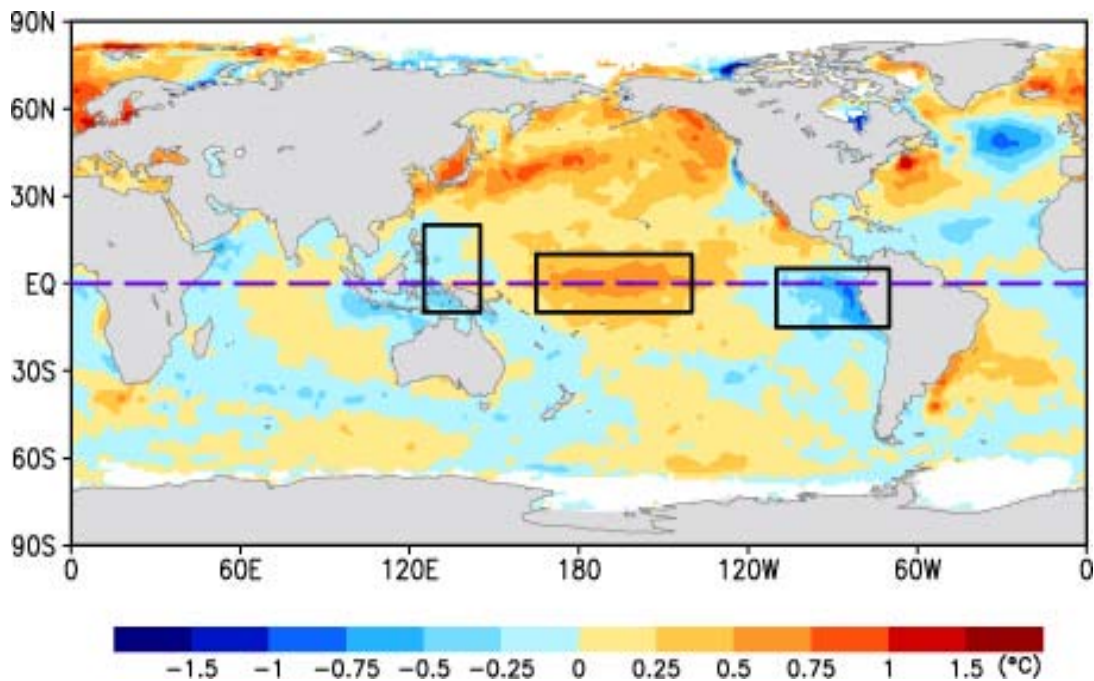


The color bar indicates summer sea surface temperature anomaly from the three largest El Niño events, 1982, 1987, and 1997. The warm colors indicate higher temperature anomaly and the cooler colors indicated lower temperature anomaly in degree Celsius. The black box outlines the region where the El Niño Index (MEI) is calculated from the sea surface temperatures (Weng et al. 2009).

Another new phenomenon that impacts the CCS seasonal cycles is El Niño Modoki (or pseudo El Niño, central Pacific El Niño, ENSO Modoki, which refers to the entire cycle). El Niño Modoki is also a coupled ocean-atmosphere phenomenon similar to the well-known ENSO (JAMSTEC 2016). The conventional ENSO pattern are very well recognized and have distinct signatures and impacts to the CCS as already discussed, see Figure 6 (JAMSTEC 2016). El Niño Modoki is characterized by the central equatorial Pacific has a warm sea surface temperatures and is flanked by colder sea surface temperatures on the east and west equatorial Pacific regions, see Figure 7, which is described in Ashok et al. (2007) as a tripolar signature due to the colder temperatures at either side of the Pacific equatorial region and the central Pacific warm region. Modoki is a Japanese word meaning “similar but different,” hence the naming of El Niño “Modoki” (Ashok et al. 2007). The signatures of El Niño Modoki are a new area of research and the

impacts to the CCS are currently not well identified. The tripole sea surface temperature pattern was first observed in 2004, a year that experts debate on whether to classify 2004 as an El Nino year based on the central Pacific warming and being sandwiched by colder regions to the east/west (Ashok et al. 2007). T. Yamagata was first to introduce the term Modoki in an effort to explain a cause to the abnormal summer conditions over Japan, which are not typical with ENSO summer weather phenomenon nor were they consistent with typical summer La Nina patterns (Ashok et al. 2007). The similarities of NPGO and El Nino Modoki characteristics are much more alike than many other observed climatological impacts to the CCS (King et al. 2011).

Figure 7. Anomalous Sea Surface Temperature during El Nino Modoki. Source: Weng et al. (2009).



The color bar indicates summer sea surface temperature anomaly from the three largest El Nino Modoki events, 1994, 2002, and 2004. The warm colors indicate higher temperature anomaly and the cooler colors indicated lower temperature anomaly in degree Celsius. The black boxes outline the region where the El Nino Modoki Index (EMI) is calculated from the sea surface temperatures (Weng et al. 2009).

The effects of El Nino Modoki impact the CCS region with decreased precipitation and sea surface temperatures, sea surface height. The impacts of this newly identified phenomenon to the CCS have yet to be investigated more observational data analysis is needed (Ashok et al. 2007). The reason this phenomenon is being distinguished from ENSO is because significant difference in the sea surface temperature characteristics in the central equatorial Pacific are not observed within the typical ENSO characteristics. The El Nino Modoki years occurred in 1986, 1990, 1991, 1992, 1994, 2002, and 2004 (Ashok et al. 2007).

THIS PAGE INTENTIONALLY LEFT BLANK



### **III. DATA AND METHODOLOGY**

#### **A. DATA**

National Oceanic and Atmospheric Administration's (NOAA) history reaches back 200 years of providing quality revolutionary research and environmental data to the prominent scientists of our time. This is no exception for the data utilized in the present research in providing the foundation to identifying and analyzing the variability of the CCS (NOAA 2016). Since NOAA's inception, the agency has undergone many migrations, divisions in an attempt to provide the pursuers of environmental data the capability to access data without constraints. Recently, NOAA's three core data centers have integrated into one National Center for Environmental Information (NCEI). The merge was enacted in an effort to preserve being considered as the leading international authority of world-wide environmental information and also to address the increasing demand for high-resolution environmental data (NOAA/NCEI 2016). It is crucial for research in variability of large scale oceanographic circulation features to have access to robust historical environmental data, including nutrient fields, and NOAA/NCEI provides the platform of accessibility to an international scientific community through the World Ocean Database (WOD) (Boyer et al. 2013).

##### **1. World Ocean Database Hydrographic Data**

The NOAA NCEI WOD is a suite of raw observational data that provides the world's largest collection of free oceanographic data and has been of great utility to large scale climate circulation research, operational forecasting communities such as the United States Navy, international oceanographic communities, including the Intergovernmental Program on Climate Change (IPCC) of the United Nations who emphasizes studying the effects and causes of global climate change (Boyer et al. 2013). The comprehensive quality-controlled measurements of historical ocean profiles include parameters such as: temperature, salinity, oxygen, phosphate, nitrate, silicate, chlorophyll, alkalinity, pH,  $p\text{CO}_2$ ,  $\text{TCO}_2$ , Tritium,  $\Delta^{13}\text{Carbon}$ ,  $\Delta^{14}\text{Carbon}$ ,  $\Delta^{18}\text{Oxygen}$ , Freons, Helium,  $\Delta^3\text{Helium}$ , Neon, and plankton (Boyer et al. 2013). The WOD profiles are a digital product available

online to anyone interested in ocean research, to include earth's climate, large scale circulation patterns, marine resource management, global operational forecasting of environmental systems, and ecosystem response to variabilities of the ocean and atmospheric. Understanding these areas of study is a function of the ability to analyze current and historical observational data in an effort in determining the ocean's role in the global climate system (Boyer et al. 2013). The WOD is comprised of observed oceanographic variables from observed depth levels in addition to standard depth levels, in this research only the observed depth levels were utilized to limit the overabundance of interpolated data fields. Table 1 provides a list of all instrument types contained in the WOD, including meteorological and sea state measurement data. To put into perspective the quantity of data contained within the WOD, it maintains 12.8 million temperature profiles and 5.4 million salinity profiles all are updated on a quarterly basis and made available to the international scientific community (Boyer et al. 2013). More specific information on resolution and instrument specifications can be found in Boyer et al. (2013, Chapters 2–16).

Table 1. Instrument Types in the WOD. Adapted from Boyer et al. (2013).

<b>DATASET</b>	<b>SOURCE</b>
OSD	Bottle, low-resolution Conductivity-Temperature-Depth (CTD), low-resolution XCTD data, and plankton data.
CTD	High-resolution Conductivity-Temperature-Depth (CTD) data and high-resolution XCTD data.
MBT	Mechanical Bathythermograph (MBT) data, DBT, micro-BT
XBT	Expendable (XBT) data.
SUR	Surface only data (bucket, thermosalinograph).
APB	Autonomous Pinniped Bathythermograph-Time-Temperature-Depth recorders attached to elephant seals.
MRB	Moored buoy data from TAO (Tropical Atmosphere-Ocean), PIRATA (moored array in the tropical Atlantic), MARNET, and TRITON (Japan-JAMSTEC).
PFL	Profiling float data.
DRB	Drifting buoy data from surface drifting buoys with thermistor chains.
UOR	Undulating Oceanographic Recorder data from a Conductivity/Temperature/Depth probe mounted on a towed undulating vehicle.
GLD	Glider data.

The data is obtained from diverse network of international ocean data sources to include: individual scientists, scientific research teams, institutional, national, and regional data centers, for specific programs and data sources see Table 2. For additional information on data sources see Boyer et al. (2013).

Table 2. Data Sources of WOD. Adapted from Boyer et al. (2013).

DATA SOURCE	SOURCE DESCRIPTION
IOC Global Oceanographic Data Archaeology and Rescue Project	Intergovernmental Oceanographic Commission (IOC) Project objective is to locate and rescue oceanographic data that is stored in digital or manuscript form and is at risk of being lost as a result of obsolete media source.
World Ocean Database Project	Digital data from oceanographic institutes is not at risk of being lost but also has not been submitted to the WDC system. This data is compared to existing data within the WDC system to check for duplicate dataset profiles.
Near-real time data sources	Database that reports “real-time” temperature and salinity profiles from various instruments types.
International Research Projects Data	Multiple data is included for various international projects obtained from CLIVAR and Carbon Hydrographic Data Office.
ICES Contribution	International Council for Exploration of the Seas (ICES) data is incorporated within the WOD dataset.
Declassified Naval Data Sets	At the end of the Cold War substantial amount of oceanographic data was declassified and has been submitted to the WOD. Other military agencies that provide data is United States Coast Guard, United States Navy, and Australian Navy.
Integrated Global Ocean Services—Volunteer Observing Ship Programs	Internationally coordinated programs that collect meteorological and oceanographic data from merchant ship.
NOAA Ship-of-Opportunity Program (SOOPP)	Instruments placed on Volunteer Observing Ships acquire surface meteorological data and XBT profiles by means of an automated system for acquiring and transmitting data via satellite.
SURTROPAC	French Ship-of-Opportunity Program that takes sea surface temperature, salinity, chlorophyll observations.
Underway CO <sub>2</sub>	Surface measurements of pCO <sub>2</sub> and TCO <sub>2</sub> are included from SOOP programs.

There are multiple hurdles in the process of acquiring oceanographic research data, first maintaining historical data in a system that can be processed and made useful to ocean scientists across the globe, second is the research monetary cost associated with

acquiring data is astronomical, and third is verifying the quality of the data being received.

The first hurdle is one of the most essential features of the WOD. All data received into the WOD system is stored in one location and is molded into one standard format. The standardization from a myriad of diverse sources (cruises, stations, gliders etc.) are compatible for online distribution to a multitude of programming languages and thus making the data accessible to as many users as possible (Boyer et al. 2013).

It is estimated that cost to replace all the historical data contained within the WOD is on the order of \$6.8 billion that is based solely on the operational costs of running the research vessels not including salaries of scientists or technicians, or the equipment cost (Boyer et al. 2013). The role of the WOD to advancing the field of oceanography is irreplaceable based on efficiency of researcher time, cost efficiency and the cost data processing alone. The monetary savings the WOD has provided would have otherwise not have been possible (Boyer et al. 2013).

The vast information within WOD is further improved with implementation of quality control flags. When data is received it is filtered and quality checked based on Type I or Type II statistical errors of normal distribution and data will be determined as “acceptable,” “unacceptable,” or “questionable.” The benefit of flagging flawed data is the user can choose to ignore all flags or partial flags in the interested data set (Boyer et al. 2013). This feature is important for researches interested in mesoscale features because the technique of flagging may smooth out important signatures within the data. The data within the WOD had undergone full quality controlled through April 2013 and data preceding had undergone an initial quality control through 2014 data submission. In addition, with the quality control temperature and salinity values receive the highest level of quality control. For the purposes of this research, all quality control flags were accepted. Justification for accepting all quality controlled flags is the minute signatures of mesoscale features are not significant in the examination of large scale circulation patterns such as the seasonal variations of the CCS over a prolonged time period (WOD 2016).

These aspects are why the WOD is regarded as the most complete datasets of oceanographic data and is predominantly of great utility to operational forecasting and scientific research communities (Boyer et al. 2013). One of the most widely used products developed from the WOD is Climatological Atlas of the World's Ocean (WOA) (Levitus 1982), which is classified as a climatological monthly mean and annual mean of the world's oceans temperature and salinity data (WOA Database 2016).

Chu and Fan (2016) developed an optimal spectral decomposition (OSD) method to produce a 3D synoptic monthly gridded (SMG) temperature and salinity dataset from the WOD (SMG-WOD). The SMG-WOD for this research is bounded by [0°–54°N, 165°W–105°W] from January 1945 to December 2014 and allows for investigation of the long-term spatial and temporal variability of the CCS with 1°×1° horizontal resolution and 28 vertical levels, the spacing of the levels is specified in Table 3 (Chu et al. 2003a,b; 2004; 2015). The dataset is stored on the NOAA/NCEI WOD for public use (Chu and Fan 2016). The SMG-WOD has the same spatial resolution as the WOA but in addition provides higher time resolutions (synoptic vs. climatological) and longer time frame of data (1945–2014 vs. 1982–2014).

Table 3. Depth Layers in SMG-WOD.

<b>Layer</b>	<b>Depth (m)</b>	<b>Layer</b>	<b>Depth (m)</b>	<b>Layer</b>	<b>Depth (m)</b>
<b>1</b>	0	<b>11</b>	250	<b>21</b>	1200
<b>2</b>	10	<b>12</b>	300	<b>22</b>	1300
<b>3</b>	20	<b>13</b>	400	<b>23</b>	1400
<b>4</b>	30	<b>14</b>	500	<b>24</b>	1500
<b>5</b>	50	<b>15</b>	600	<b>25</b>	1750
<b>6</b>	75	<b>16</b>	700	<b>26</b>	2000
<b>7</b>	100	<b>17</b>	800	<b>27</b>	2500
<b>8</b>	125	<b>18</b>	900	<b>28</b>	3000
<b>9</b>	150	<b>19</b>	1000		
<b>10</b>	200	<b>20</b>	1100		

For the purposes of this research, of investigating currents and circulations within the CCS temperature, salinity profile data were examined in determining variability using the methodology developed by Chu and Fan (2016). Coastal features of the CCS are not

well resolved in the temperature and salinity SMG-WOD data fields due to spatial resolution of  $1^\circ$ . To analyze the coastal features, surface Chl-a data at 4 km resolution were acquired to resolve the horizontal resolution, in addition to the ability to identify non-seasonal and seasonal variations. More detailed information of the Chl-a data and data processing is described in Section 3. The data process analysis, OSD, for the SMG-WOD methodology is outlined in Section 2.

## **2. Optimal Spectral Decomposition**

In order to analyze the profiles within the WOD, many different methods of interpreting and displaying the ocean environment have been developed. The new method developed by Chu et al. (2015), OSD, is based on the Fourier series expansion and has the ability to analyze ocean observational data without background error covariance matrix. This is accomplished with three phases: utilizing eigenvectors of the Laplacian operator as the basis functions depending solely on the basin geometry, boundaries conditions in the modeled field are the same as in the observational data (temperature, salinity) and most importantly, these are calculated before the data assimilation is processed (Chu et al. 2015). In the present research, OSD was used to establish a 3D gridded temperature and salinity fields ingested from the WOD profiles.

New ocean phenomena have been identified utilizing OSD attesting its value of future ocean research. Some of the research include: NPS thesis in determining variability of thermohaline structures, temporal and spatial features in the East Sea, and eastern Mediterranean sea, in oceanic data assimilation new ocean phenomena have been identified to include: bimodal structure of Chl-a blooms, recurrence of reversal of currents, drifting buoys near surface, propagation of long Rossby waves in the tropical North Atlantic, and temporal and spatial variability of global ocean heat content (Choi 2015; Karaaslan 2015; Chu et al. 2015; 2005a; 2005b; 2007; 2011; Sun et al. 2010). Past research indicates the value in this research in exploring variability of temperature, salinity, and Chl-a data in the CCS.

In the development of OSD, it is important to identify the necessary conditions that satisfy the basis functions and make them available prior to the data assimilation.

The conditions are: (i) satisfy the same homogeneous boundary ( $\Gamma$ ) condition of the assimilated variable (temperature, salinity) anomaly within the ocean domain at the grid points  $[c_a(\mathbf{r}_n) - c_b(\mathbf{r}_n)]$ , (ii) they need be orthonormal, and (iii) independent of the assimilated variable (Chu et al. 2015). The third condition is how the basis functions are available before the data assimilation.

$$c_a(\mathbf{r}_n) - c_b(\mathbf{r}_n) = f_n s_K(\mathbf{r}_n), \quad s_K(\mathbf{r}_n) \equiv \sum_{k=1}^K a_k \phi_k(\mathbf{r}_n), \quad (1)$$

where  $(\phi_k)$  are basis functions,  $(K)$  is the mode truncation and represents  $(f_n)$  the observational contribution into the grid points. In order to have the three necessary conditions met, the most convenient way is with the use of eigenvectors of the horizontal Laplacian operator as the basis function,  $(\phi_k)$ , and is a unit vector normal to the lateral boundary ( $c-c_b$ ). In ocean data analysis, the first and third conditions of OSD, distinguish the eigenvectors from the commonly used empirical orthogonal functions (EOF). The nature of observational data contains a high level of noise. In an effort to provide stability and filter out errors within the observational data, the rotation matrix provides the needed adjustment to the formulation in the data assimilation as described in Chu et al. (2004). For more detailed OSD methodology approach see Chu et al. (2015).

The feasibility of OSD was investigated in Chu et al. (2015) by using a double model comparison via the Parallel Ocean Program (POP) model. The internationally employed POP model is a generic ocean circulation model and has the ability to solve 3D simple equations for ocean dynamics. In addition, it provides users an in depth description of computational grid for space and time (Smith and Gent 2002). More detailed information can be found on POP model and its application to OSD verification in Chu et al. (2015) and Smith and Gent (2002).

### 3. Chlorophyll-a Concentration Data

Limitations of SMG-WOD horizontal resolution of coastal features were difficult to identify. For a comprehensive analysis of the CCS coastal features, Chl-a data were used specifically to identify the coastal circulations. The data was obtained from Moderate Resolution Imaging Spectroradiometer (MODIS), an instrument deployed on



Aqua satellite (A). MODIS-A measures radiance and or reflectance from top-of-atmosphere in various spectral bands in the near-infrared and visible wavelengths (MODIS 2016; Hu 2012). The MODIS-A is predominantly utilized for the observing Earth's surface (land and ocean) and provides comprehensive data on global ocean bio-optical and biogeochemical properties in an effort to study dynamics of oceanic and atmospheric processes. The platform is sun synchronous, near polar orbit at 705 km altitude that covers the Earth every one to two days (MODIS 2016). The surface images are captured in 36 spectral bands at various resolutions, for more specific information on spectral bands see MODIS technical manual on the data website (MODIS 2016). The data is then composited over the span of multiple days and then averaged into a monthly product available for public use. For the purposes of this research, Level 3 standard mapped images, with 4.6 km resolution was utilized (MODIS 2016). The MODIS-A Chl-a data cover the period from July 2002 to present, however to maintain consistency with the WOD quality controlled data, 2015 and 2016 were omitted. The data were accessed through a public domain as a monthly NetCDF file through the MODIS-A (2016) website. The website and data were acquired in January 2016, and as of April 2016 the same data is available at a different online address NASA (2016). A batch download was used through a custom MATLAB script, that allowed for downloading one file at a time, the data was then portioned out for the CCS region to match the boundaries of the WOD data [0°–54°N, 165°W–105°W] and the resulting data was then saved for analysis. One limitation of obtaining data from satellite is that it is sensitive to cloud cover and reflection from sun glint off the ocean surface that results in areas where Chl-a concentration is sparse or non-existent (Hu 2012). This is corrected by interpolating the data for consistent coverage over the region.

It is important to note that the product download of the Chl-a contained regions of missing data (which appear as white in the images, see Figure 14). The cropped out regions are specific to the Eastern Pacific Subarctic (PSAE) over the months of November through February north of 48°N (Watson and Casey 2007). The missing data is an artifact of how the data is obtained from the MODIS-A satellite. For satellites it is difficult to attain surface Chl-a measurements when there are significant environmental

limiting factors prohibiting the observation of the ocean surface. For lower latitude regions the environmental limiting factors is minimal and can be interpolated over a few days or weeks to produce a product with little bias influencing results (Djavidnia et al. 2010). However, in the high latitude regions, the environmental factors that are characteristic to the winter season and latitude, such as clouds, snow sea ice coverage, and aerosol concentration in the atmosphere impact the results of the MODIS-A interpolation methods used in other regions of the globe. When interpolation is applied to the PSAE it introduces significant bias in the product. The PSAE is not the only region the environmental factors impact the product (Watson and Casey 2007). This is a common issue among other satellite programs, not just MODIS-A. In order to reduce bias and increase the quality of the product across the other regions of the globe with adequate coverage, these regions of significant environment factors are omitted from the dataset (Watson and Casey 2007; Djavidnia et al. 2010).

#### **4. Climatological Indices**

Inter-annual variability is best identified through climatological indices when abundant data is available and processed as in the WOD and MODIS databases. Climate indices are a useful approach because once a statistical method is applied, such as EOF analysis, the methodology used in this research, the results can indicate well known and easily identifiable climate patterns based on correlation percentages, in addition indices can indicate deviation from the normal climatological variations. In this research, the two climatological indices that are relevant to the Pacific Ocean's climatological circulations were applied, Multivariate El Nino/Southern Oscillation (ENSO) Index (MEI) and a new phenomenon being investigated El Nino Modoki (EMI). The descriptions and specific indices are explained in more in preceding sections.

#### **5. Multivariate El Nino/Southern Oscillation Index**

An El Nino event is characterized by weakening of the trade winds and in turn warming in the eastern equatorial Pacific can extend through the central equatorial Pacific, see Figure 6. The effect of El Nino events on the CCS has been identified to impact through atmospheric and oceanic forcing (Jacox et al. 2015). Atmospheric forcing

influences the CCS as a result of weakening of Pacific equatorial winds consequentially there is weakening detected in the upwelling circulation along the coast. The chain reaction from oceanic forcing in the CCS is noticed via depth changes in the CCS thermocline as the Pacific equatorial thermocline becomes more shallow so does the CCS thermocline. Overall, the CCS will experience warming of the upper water layers and slowing of the current, which suffocates biological productivity as a result of reduced upwelling (Jacox et al. 2015).

El Nino/Southern Oscillation ocean-atmosphere phenomenon is a globally recognized climatological feature. A lot of scientific observational research is being conducted to determine the prolonged impacts to the CCS. El Nino has drastic and lasting impacts on highly populated regions of the world and specifically to the Pacific Rim. As a result to the large scale impacts, the resources into studying ENSO have been significant. In an attempt to monitor the development, strength and occurrence of El Nino has been created with more emphasis on other variables than the traditional sea surface temperature and mean sea level pressure. This initiative to enhance indicators of ENSO has also lead to redefining the evolution of an El Nino event (Weng et al. 2009). The revised definition of El Nino was in an effort to better define an index for consistency of communication and diagnosis of potential El Nino events. The definition is based on a three month average of sea surface temperature departure greater than  $0.5^{\circ}\text{C}$  from the normal in the equatorial Pacific Ocean bounded by ( $5^{\circ}\text{N}$ – $5^{\circ}\text{S}$ ,  $170^{\circ}\text{W}$ – $90^{\circ}\text{W}$ ), the normal is based on the 1971 to 2000 baseline (NOAA El Nino 2016; Ashok et al. 2007; Weng et al. 2009). This change sparked the identification and clarification of the assumed El Nino years and also allowed for deviation from the conventional ideals and El Nino Modoki resulted.

The first El Nino index developed included the two identifiers for El Nino, sea surface temperature and mean sea level pressure, however since its inception, the El Nino climatological index has grown to include six observed variables from the tropical Pacific that include: sea level pressure, zonal and meridional components of the surface wind, sea surface temperature, surface air temperature, and total cloudiness fraction on the sky, which is known as the Multivariate El Nino/ Southern Oscillation Index (MEI) (NOAA

MEI 2016). Multivariate ENSO Index is not the only ENSO index available, other indices include Oceanic Nino Index (ONI) and is based on sea surface temperature anomalies in different regions of the equatorial Pacific region and monitors the current ENSO condition from a historical perspective (Ashok et al. 2007).

The MEI is calculated to the first un-rotated Principal Component (PC) for all six of the fields described. The variable fields were then merged by standardizing the total variance for each individual field. Finally, the first PC is extracted from the co-variance matrix. The MEI was selected for this research based on the diverse observational fields from oceanic and atmospheric available to identify ENSO within the CCS region.

MEI is based on six observable fields' sea level pressure, zonal and meridional components of the surface wind, sea surface temperature, surface air temperature, and total cloudiness fraction on the sky is calculated to the first un-rotated PC for all six of the fields.

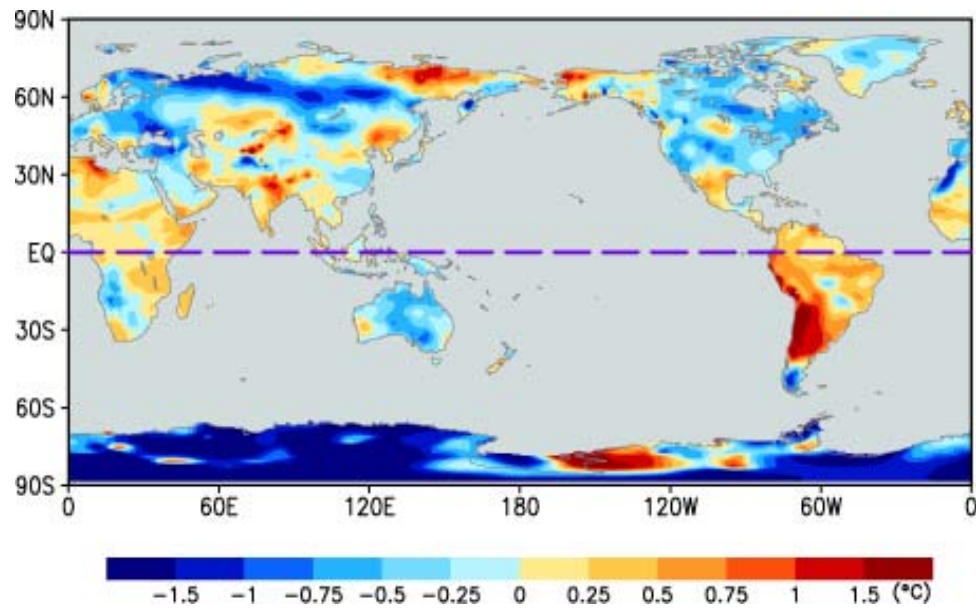
## **6. El Nino Modoki Indices**

El Nino Modoki (or pseudo El Nino, central Pacific El Nino, ENSO Modoki, which refers to the entire cycle), is a coupled ocean-atmosphere phenomenon similar to the well-known ENSO. The conventional ENSO pattern is characterized by strong irregular warming of the sea surface in the eastern equatorial Pacific that elongates through the central Pacific with colder temperatures in the western equatorial Pacific, see Figure 6 (JAMSTEC 2016). The signatures of El Nino are very well recognized and have distinct teleconnection patterns. The teleconnection patterns of El Nino Modoki are just being identified and are different than the teleconnections seen in conventional El Nino. Modoki is a Japanese word meaning “similar but different,” hence the naming of El Nino “Modoki” (Ashok et al. 2007). The new phenomenon is characterized by the central equatorial Pacific has a warm sea surface temperatures and is flanked by colder sea surface temperatures on the east and west equatorial Pacific regions, see Figure 7, described in Ashok et al. (2007) as a tripolar signature due to the colder temperatures at either side of the Pacific equatorial region and the central Pacific warm region. The tripole sea surface temperature pattern was first observed in 2004, a year that experts

debate on whether to classify 2004 as an El Nino year based on the central Pacific warming and being sandwiched by colder regions to the east/west (Ashok et al. 2007). T. Yamagata was the first to introduce the term Modoki in an effort to explain a cause to the abnormal summer conditions over Japan that are not typical with ENSO summer weather phenomenon nor were they consistent with typical summer La Nina patterns (Ashok et al. 2007).

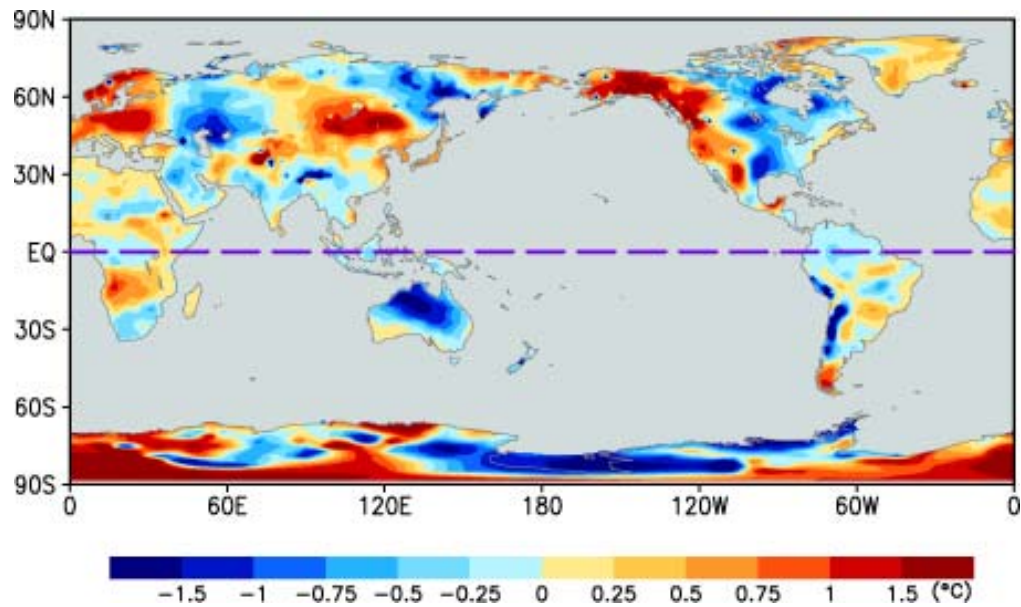
The effects of El Nino Modoki impact the precipitation, temperature, and global climate signals. The effects can be seen throughout the Pacific Rim and all over the globe as represented in Figure 8 and Figure 9. These figures are a comparison of the global impacts of El Nino, Figure 8, as compared to El Nino Modoki, Figure 9, on the continental surface temperature and rain fall. The impacts of El Nino Modoki are opposite of the impacts of the ENSO temperature and precipitation impacts. In addition, El Nino Modoki impacts both boreal summer (June, July, August, and September) and boreal winter (December, January, and February) seasons. During the boreal summer, the sea surface temperature in the central Pacific is warmer and is surrounded by colder sea surface temperatures to the east and west, with the eastern Pacific being more spread out. The boreal winter is similar to the summer with the exception of the colder regions covering a wider surface area of the western Pacific (Ashok et al. 2007). Typical weather associated with El Nino Modoki is characterized by more moisture in the higher latitude, as seen in Figure 10, owing to the West Coast of the United States experiencing dryer conditions as compared to El Nino, see Figure 11, which typically brings more significant rain fall to the same region (Ashok et al. 2007). The impacts of this newly identified phenomenon to the CCS have yet to be investigated more observational data analysis is needed (Ashok et al. 2007).

Figure 8. Averaged Global El Nino Continental Surface Temperatures. Source: JAMSTEC (2016).



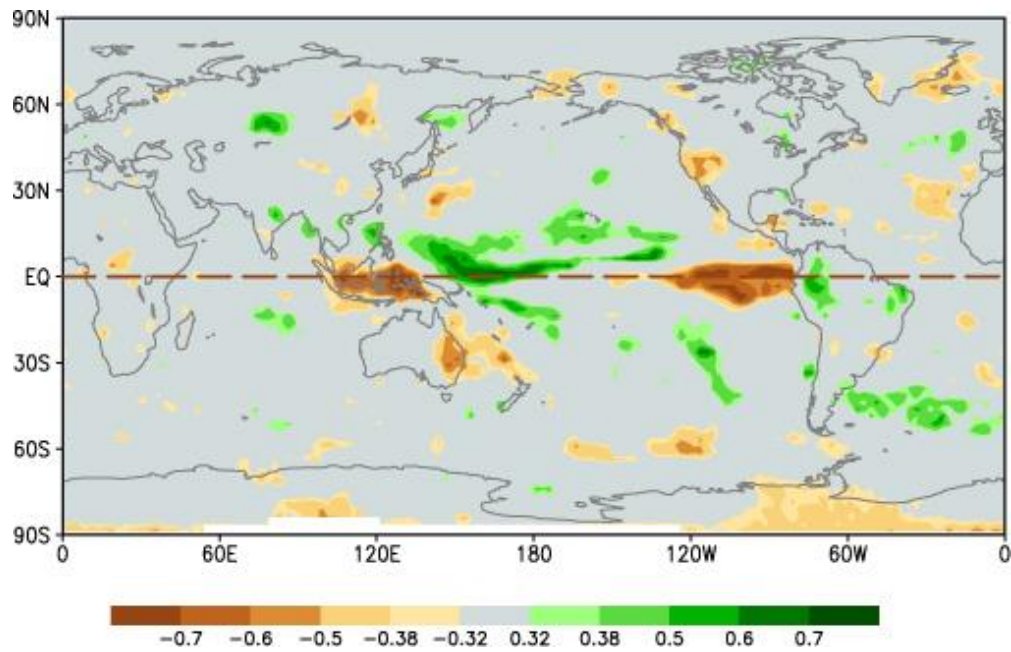
The color bar indicates averaged global summer surface temperatures of all recorded El Niño events. The warm colors indicate higher temperature averages and the cooler colors indicated lower temperature average in degree Celsius (JAMSTEC 2016).

Figure 9. Averaged Global El Nino Modoki Continental Surface Temperatures.  
Source: JAMSTEC (2016).



The color bar indicates averaged global summer surface temperatures of all recorded El Nino Modoki events. The warm colors indicate higher temperature averages and the cooler colors indicated lower temperature averages in degree Celsius (JAMSTEC 2016).

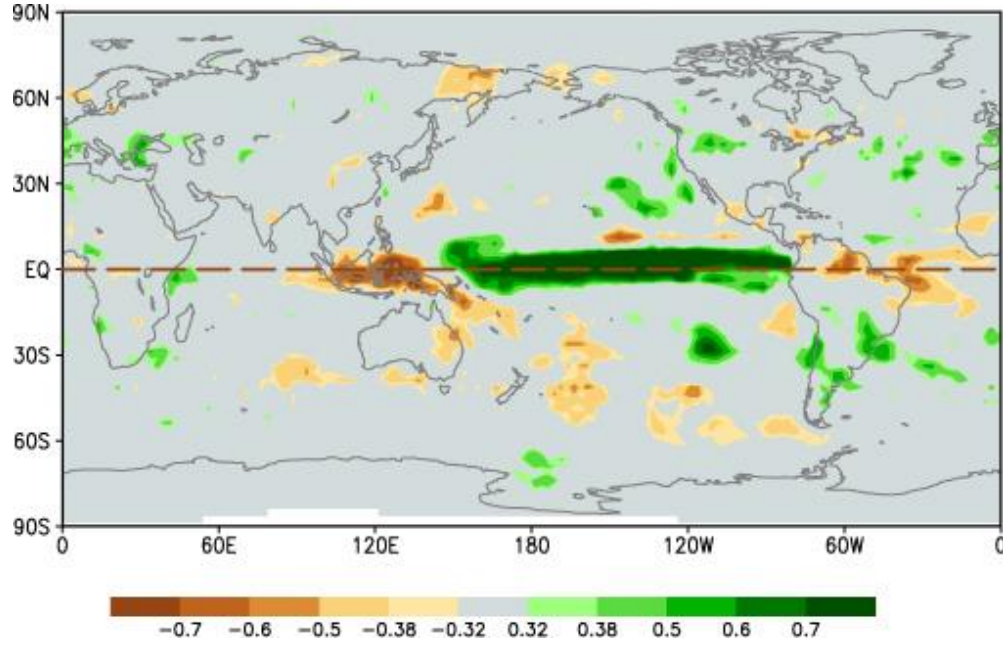
Figure 10. Averaged Global El Nino Modoki Rain Fall. Source: JAMSTEC (2016).



The color bar indicates averaged global rain fall of all recorded El Nino Modoki events. The brighter colors indicate higher rain fall averages and the darker colors indicated lower rainfall averages (JAMSTEC 2016).



Figure 11. Averaged Global El Nino Rain Fall. Source: JAMSTEC (2016).



The color bar indicates averaged global rain fall of all recorded El Nino events. The brighter colors indicate higher rain fall averages and the darker colors indicated lower rainfall averages (JAMSTEC 2016).

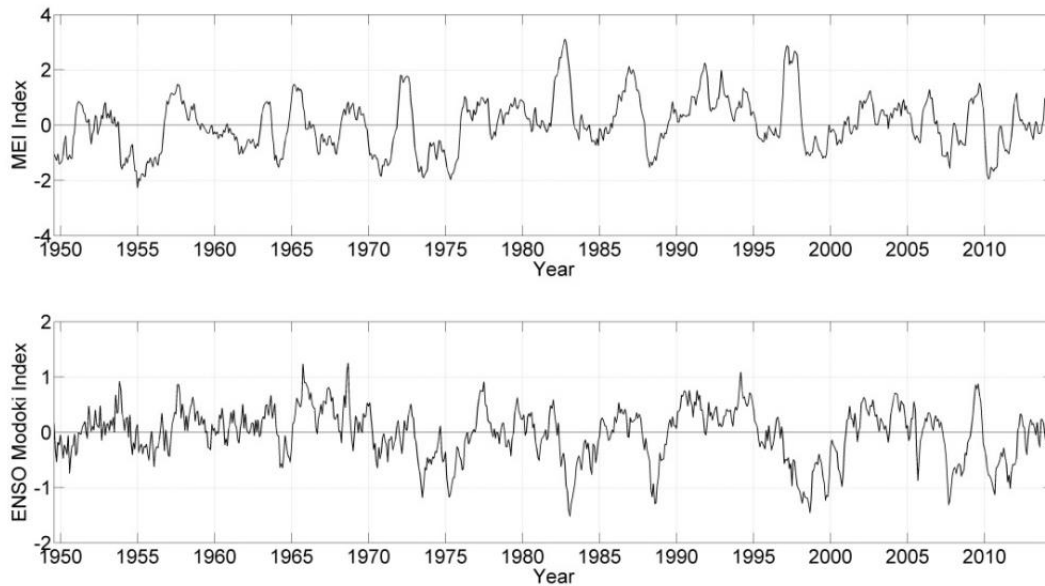
The reason this phenomenon is being distinguished from ENSO is because the tripolar sea surface temperature characteristics are not seen within the typical ENSO cycle, but it occurs frequently enough to be identified using EOF analysis and has high correlation with certain EOF modes and can be classified.

The data used in the present research to identify EMI for verification can be accessed through the JAMSTEC Modoki website monthly data link (2016). Ashok et al. (2007) were able to formulate an index for El Nino Modoki. The formulation represents the tripolar nature of the El Nino Modoki through sea surface temperature anomalies (SSTA).

$$EMI = [SSTA]_A - 0.5 * [SSTA]_B - 0.5 * [SSTA]_C. \quad (2)$$

Equation (2) identifies EMI through a data set of SSTA, each square bracket denotes the averaged SSTA for a specific region identified by A (10°S–10°N, 165°E–140°W), B (15°S–5°N, 110°W–70°W), and C (10°S–20°N, 125°E–145°E), respectively (Ashok et al. 2007). An EMI and MEI time series is shown in Figure 12 to indicate years of significant activity of El Nino or El Nino Modoki.

Figure 12. Time Series of El Nino Modoki and Multivariate El Nino Index.



This figure represents a time series of yearly (top) Multivariate El Nino Index and (bottom) El Nino Modoki Index. The x axis represents time in years from 1950 to 2015. The y axis indicates the index value and the farther away from zero the stronger the signature of the event.

## B. METHODOLOGY

The first step to analyze the variability within the CCS given the considerable amount of data available from 1945 to 2014 over the 28 vertical layers was to establish a reference layer within the water column that deviation would indicate the amount of variability present at a specified month in a specified year. Historically, and presently, it is an arduous and expensive undertaking to acquire observed measurements in the ocean in an effort to quantify velocity at all points throughout the ocean depths. Leading to utilizing density profiles for such an undertaking because density is much more readably and cheaply acquired data. The density profiles obtained from temperature and salinity data is calculated for estimating specific volume and ultimately acceleration potential (Talley 2011).

### 1. Acceleration Potential at the Isopycnal Surface $26.9 \text{ kg/m}^3$ for the SMG-WOD

Acceleration potential was first suggested by Montgomery (1937) as a method to identify a streamfunction at a surface where there exists mixing and movement of water

masses. The calculated streamfunctions show in a 2D flow pattern of the full 3D flow field relative to a reference surface within the water column (McDougall 1989). In McDougall (1989) acceleration potential defined as  $(\pi)$  however, in the current research acceleration potential will be denoted as  $(\psi)$ . Figure 13 is a graphical representation of acceleration potential referenced to pressure  $p = p_0$  in a surface of constant specific volume anomaly  $(\delta)$  a function of salinity, temperature and pressure:

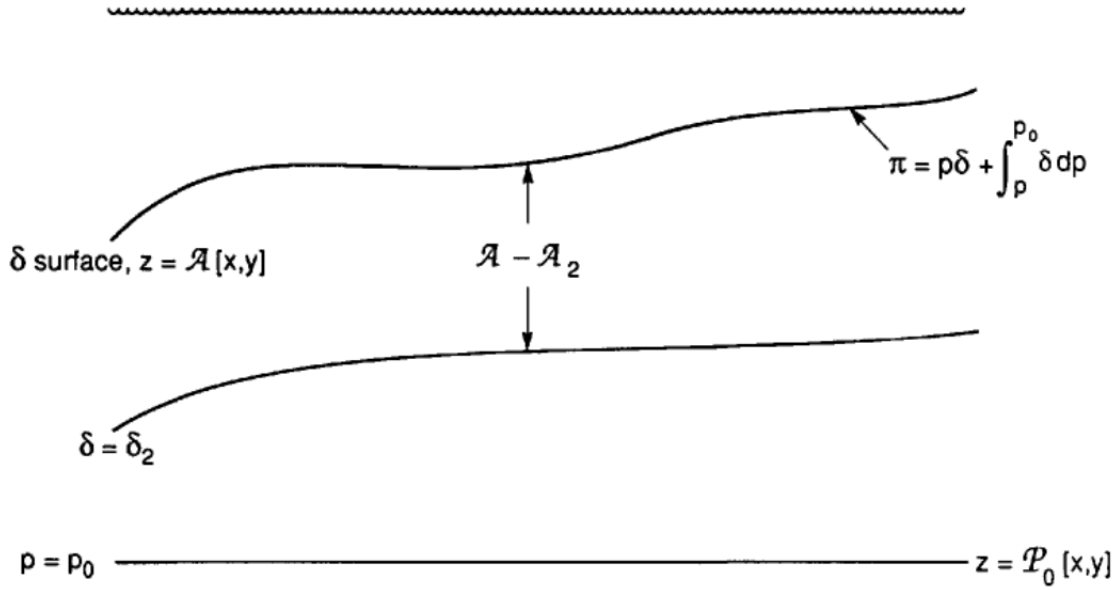
$$\delta(S, T, p) = \frac{1}{\rho(S, T, p)} - \frac{1}{\rho(35, 0, p)}, \quad (3)$$

from  $(\delta, \delta_0)$ , giving acceleration potential  $(\psi)$  to be defined as.

$$\psi = p\delta + \int_p^{p_0} \delta dp, \quad (4)$$

where  $\rho$  is density.

Figure 13. Graphical Depiction of Acceleration Potential. Source: McDougall (1989).



Acceleration potential is a method to identify a streamfunction at a surface where mixing and movement of water masses exist. Streamfunctions show a 2D flow pattern of the full 3D flow field relative to a reference surface within the water column. In this figure, acceleration potential defined as  $(\pi)$ ; however, in the current research, acceleration potential will be denoted as  $(\psi)$  in reference to pressure  $p = p_0$  in a surface of constant specific volume anomaly  $(\delta)$ .

By using the acceleration potential,  $(\pi)$ , it reveals the difference between the horizontal velocity field along the specific volume anomaly surface  $(\delta)$  at the isobaric surface,  $p = p_0$  and also in a constant density,  $\rho$ , surface. The significance of calculating the acceleration potential is that the geostrophic flow is the same streamfunction in the specific anomaly surface and will indicate variations from a reference level for a specified time and region. For in situ data, by indicating a relevant density surface it will represent the direction of the horizontal components of a 3D velocity field. The streamfunction will be similar to the velocity and therefore the 2D streamlines will be a good approximation to the total 3D physical flow (McDougal 1989).

In the current research, a monthly fluctuating acceleration potential  $(\psi)$  relative to 1000 dbar is calculated over the period of January 1945 to December 2014 to analyze the spatial and temporal variability of the CCS, from the SMG-WOD. The acceleration potential at the isopycnal surface of  $(\sigma_\theta)$  26.9 kg/m<sup>3</sup> was used here and denoted as

$\psi(\mathbf{r}_i, \tau_k, t_l)$  is a function of  $\mathbf{r}_i$  a vector indicating location on a 2D horizontal grid,  $i = 1, 2, \dots, I$ , and  $I$  is the total number of horizontal grid points,  $\tau_k$  is the year time sequence (1945, 1946, ..., 2014),  $t_l$  is the monthly sequence (1, 2, ..., 12). The notations used in the present research are shown in the Notation Table 5 with comments and appropriate equations.

This was calculated for the region of  $[0^\circ\text{--}53^\circ\text{N}, 165^\circ\text{W}\text{--}105^\circ\text{W}]$ . Due to the horizontal resolution of the SMG-WOD data of  $1^\circ \times 1^\circ$  the CU and regions near the coast are not resolved by the acceleration potential field. In addition, the region north of  $54^\circ\text{N}$  was not included in the calculations as a result of the isopycnal surface reaching the surface and thus rendering the data useless for the purposes of identifying a consistent surface as a basis to calculate seasonal and inter-annual variabilities.

## 2. Composite Analysis

A composite analysis (Chu et al. 1997; 1998; Chu 2011) is conducted to determine the Total Time Mean for the acceleration potential field ( $\psi$ ) and the Chl-a concentration data ( $C$ ). Here, the acceleration potential field is used to explain the methodology. The Chl-a synoptic mean fields  $C(\mathbf{r}_i, \tau_k, t_l)$  have been analyzed using the same approach for the acceleration potential and calculating  $C(\mathbf{r}_i, t_l)$ . See Notation Table 5 for a detailed list of equations and explanations.

The Climatological Monthly Mean is calculated by,

$$\bar{\psi}(\mathbf{r}_i, t_l) = \frac{1}{\Delta\tau} \sum_k \psi(\mathbf{r}_i, \tau_k, t_l) \quad . \quad (5)$$

The Total Time Mean calculation for the period of 1945 to 2014 is,

$$\bar{\bar{\psi}}(\mathbf{r}_i) = \frac{1}{12} \sum_{l=1}^{12} \bar{\psi}(\mathbf{r}_i, t_l) \quad . \quad (6)$$

The Climatological Monthly Anomaly ( $\tilde{\psi}(\mathbf{r}_i, t_l)$ ) is defined by,

$$\tilde{\psi}(\mathbf{r}_i, t_l) = \bar{\psi}(\mathbf{r}_i, t_l) - \bar{\bar{\psi}}(\mathbf{r}_i) \quad . \quad (7)$$

The Synoptic Monthly Anomaly ( $\hat{\psi}(\mathbf{r}_i, \tau_k, t_l)$ ), identifies inter-annual variability and is calculated as the deviation from the monthly mean ( $\bar{\psi}(\mathbf{r}_i, t_l)$ ) value,

$$\hat{\psi}(\mathbf{r}_i, \tau_k, t_l) = \psi(\mathbf{r}_i, \tau_k, t_l) - \bar{\psi}(\mathbf{r}_i, t_l). \quad (8)$$

Next the Synoptic Monthly Anomaly ( $\hat{\psi}(\mathbf{r}_i, \tau_k, t_l)$ ) is re-arranged into an  $I \times P$  matrix  $\hat{\psi}(\mathbf{r}_i, \tilde{t}_p)$ , where,  $p = 1, 2, \dots, P$ , where  $P$ , is the time in years (1945–2014) equaling 70 years, multiplied by 12 months, resulting with  $P = 840$  total number of months or total number of points in the matrix,  $i = 1, 2, \dots, I$ , where  $I$  is the total number of grid points where the acceleration potential is defined, resulting with  $I = 3188$  in the matrix.

### 3. Empirical Orthogonal Function Analysis

The objective of EOF is identifying a group of variables that represent the highest variance in observational data set through a linear set of the original variables (Chu et al. 1997). The technique has been in existence since the early 1950s and since then it has been a powerful statistical analysis tool for environmental research. The challenging task and important analysis tool when large amounts of data is involved is the ability to extract important patterns from measurements in a meaningful interpretation of atmospheric and oceanic processes, circulations, and variables, which EOF analysis provides.

The purpose of using EOF in this research was to find a liner combination of acceleration potential (and Chl-a) data that highlights the maximum variance. Here the EOF expansion is calculated for acceleration potential and Chl-a by

$$\hat{\psi}(\mathbf{r}_i, \tilde{t}_p) = \sum_j PC_j(\tilde{t}_p) E_j(\mathbf{r}_i), \quad (9)$$

where  $E_j(\mathbf{r}_i)$  is the  $j^{\text{th}}$  EOF mode with a unit of J/kg and  $PC_j(\tilde{t}_p)$  is the  $j^{\text{th}}$  non-dimensional principal component. In this research,  $j = 1, 2, \dots, J$  and where  $J=30$  is the cutoff number of the EOF modes. With Equation (9), the orthogonality property offers a comprehensive basis where the time-varying field is disconnected and limits the physical interpretability of individual EOFs. In order to obtain inter-annual variations of the acceleration potential field, an EOF analysis was conducted for the Synoptic Monthly Anomalies ( $\hat{\psi}$ ), which are deviations of Synoptic Monthly Means from Climatological Monthly Means and characterize inter-annual variability.

The limitations of EOF are the ability of physical interpretation of the patterns produced due to the strong constraints from orthogonality in space and time (Hannachi 2004). This has caused controversy because physical modes are not naturally orthogonal in nature and therefore may not be accurately represented in the data output (Simmons et al. 1983). This limitation can be minimized with the implementation of a rotated field to accommodate the real physical representation (Richman 1986). A drawback to EOFs is when they are utilized for dimensionality reduction of the observed data, specifically the truncation order applied to Equation (9). The truncation order, when applied, is obtained by setting the variance and choosing the leading EOF, which explains the total variance. Another limitation of EOF is the non-uniform distribution of data for a given area being analyzed. The non-uniformity or data sparse regions can influence the structure of the computed EOF. This limitation was mitigated because the data was compiled in a gridded system and thus reducing the issue of non-uniformity in data regions (Hannachi 2004).

#### **4. Pearson Correlation Coefficient**

Pearson's Correlation Coefficient was used to determine correlations between the inter-annual variability of acceleration potential at the intermediate level and climatological indices, and to estimate shared variance of the EOF modes for the acceleration potential and the Chl-a data. Pearson Correlation Coefficient is a dimensionless quantity of the linear covariation of variables; or in other words it measures the degree of similarity or deviation in a linear relationship of variables. Pearson Correlation Coefficient is usually between 1 and -1. A positive value signifies a positive linear correlation meaning when one variable increases the other variable will also increase. Negative values signify a negative linear correlation meaning when one variable increases the other variable decreases. A strong correlation is signified by how closely the coefficient is to either 1 or -1, if the value is exactly 1 or -1 then the variables have perfect linear relationship or perfectly correlated, however a zero value signifies no correlation and the variables have no linear relationship. All variables are in some way correlated, and the Pearson Correlation Coefficient will help identify a linear relationship of variables, a coefficient may have another form of correlation (for example: parabolic,

or curvilinear) but the Pearson Correlation Coefficient will still remain equal to zero (Huntsberger et al. 1973).

A simple calculation of the correlation coefficient, **r**, is shown in Equation (10) and the x and y signify the variables being compared. Table 4 identifies how the absolute value correlation coefficient value, **r**, would indicate a level or correlation, as suggested by Evans (1996) (Huntsberger et al. 1973).

$$\mathbf{r} = \frac{\sum (x - \bar{x})(y - \bar{y})}{\sqrt{\sum (x - \bar{x})^2 \sum (y - \bar{y})^2}} \quad (10)$$

Table 4. Absolute Value Correlation Coefficient. Adapted from Huntsberger et al. (1973).

Pearson Correlation Coefficient	Linear relationship
.00-.19	Very Weak
.20-.39	Weak
.40-.59	Moderate
.60-.70	Strong
.80-1.0	Very Strong



Table 5. Notation Table for Reference to Data Calculations.

Term	Notation	Equation/Comments	Equation Reference
El Nino Modoki	EMI	$EMI = [SSTA]_A - 0.5 * [SSTA]_B - 0.5 * [SSTA]_C$	(2)
Multivariate El Nino Index	MEI	-	-
Location on grid points	$\mathbf{r}_i$	2D location and $i$ is the horizontal grid points	-
Years	$\tau_k$	1945–2014	-
Months	$t_l$	1–12	-
Specific Volume anomaly, $m^3/kg$	$\delta$	$\delta(S, T, p) = \frac{1}{\rho(S, T, p)} - \frac{1}{\rho(35, 0, p)}$	(3)
Acceleration Potential, J/kg	$\psi$	$\psi = p\delta + \int_p^{p_0} \delta dp$ or $\pi = p\delta + \int_p^{p_0} \delta dp$	(4)
Acceleration Potential Synoptic Monthly Mean	$\psi(\mathbf{r}_i, \tau_k, t_l)$	Monthly value for all years and all months	
Acceleration Potential Climatological Monthly Mean	$\bar{\psi}(\mathbf{r}_i, t_l)$	$\bar{\psi}(\mathbf{r}_i, t_l) = \frac{1}{\Delta\tau} \sum_k \psi(\mathbf{r}_i, \tau_k, t_l)$ Total monthly mean for all months in all years	(5)
Acceleration Potential Total Time Mean	$\bar{\bar{\psi}}(\mathbf{r}_i)$	$\bar{\bar{\psi}}(\mathbf{r}_i) = \frac{1}{12} \sum_{l=1}^{12} \bar{\psi}(\mathbf{r}_i, t_l)$	(6)
Acceleration Potential Climatological Monthly Anomaly	$\tilde{\psi}(\mathbf{r}_i, t_l)$	$\tilde{\psi}(\mathbf{r}_i, t_l) = \bar{\psi}(\mathbf{r}_i, t_l) - \bar{\bar{\psi}}(\mathbf{r}_i)$ deviation of Climatological Monthly Mean from the Total Time Mean	(7)
Acceleration Potential Synoptic Monthly Anomaly	$\hat{\psi}(\mathbf{r}_i, \tau_k, t_l)$	$\hat{\psi}(\mathbf{r}_i, \tau_k, t_l) = \psi(\mathbf{r}_i, \tau_k, t_l) - \bar{\psi}(\mathbf{r}_i, t_l)$ deviation of Synoptic Monthly Mean from the Climatological Mean; characterized inter-annual variability	(8)
Chlorophyll-a Concentration,	$C$	All Chl-a concentration composite analysis was computed by the same	

Term	Notation	Equation/Comments	Equation Reference
mg/m <sup>3</sup>		methodology as acceleration potential.	
Chlorophyll-a Synoptic Monthly Mean	$C(\mathbf{r}_i, \tau_k, t_l)$	Similar to acceleration potential synoptic monthly mean	
Chlorophyll-a Climatological Monthly Mean	$\bar{C}(\mathbf{r}_i, t_l)$	Similar to Equation (5)	
Chlorophyll-a Total Time mean	$\bar{\bar{C}}(\mathbf{r}_i)$	Similar to Equation (6)	
Chlorophyll-a Climatological Monthly Anomaly	$\bar{e}(\mathbf{r}_i, t_l)$	Similar to Equation (7)	
Chlorophyll-a Synoptic Monthly Anomaly	$\hat{C}(\mathbf{r}_i, \tau_k, t_l)$	Similar to Equation (8)	
Empirical Orthogonal Function (EOF) Expansion	-	$\hat{\psi}(\mathbf{r}_i, \tilde{t}_p) = \sum_j PC_j(\tilde{t}_p) E_j(\mathbf{r}_i)$	(9)
EOF Modes	$E_j(\mathbf{r}_i)$	the j <sup>th</sup> EOF mode at a 2D location and $i$ is the horizontal grid points j = 1, 2, ..., J where J=30	(9)
Principal Components (EOF coefficients)	$PC_j(\tilde{t}_p)$	j <sup>th</sup> non-dimensional principal component	(9)
Pearson Correlation Coefficient	$\mathbf{r}$	$\mathbf{r} = \frac{\sum (x - \bar{x})(y - \bar{y})}{\sqrt{\sum (x - \bar{x})^2 \sum (y - \bar{y})^2}}$	(10)

## C. MATLAB CODES

All the calculations and plotting have been done within the Matlab framework (ref) using the following standard and custom toolboxes and functions:

Oceanographic characteristics, including potential density, potential temperature, spice, were calculated using functions from The SeaWater library of EOS-80 seawater properties v 1.1 2003/12/12 (ref).

The maps were plotted using custom functions and the M\_MAP mapping package (ref). The coastline was extracted from The Global Self-consistent, Hierarchical, High-resolution Geography Database (NOAA GSHHG 2016). The Sandwell and Smith Bathymetry with 2 min resolution (SCRIPS 2015) were used for plots.

The MODIS-A Chl-a data were batch download using the following code:

```
TimeResolution = 'Seasonal';
SpatialResolution = '4km'; % or '9km'—don't forget the apostrophes

global CA % the California Current region
CA.LonLimit = [-170 -100];
CA.LatLimit = [0 60];

WEBdata = 'http://oceandata.sci.gsfc.nasa.gov/cgi/getfile/'; % data
source

DATAin = ['http://oceandata.sci.gsfc.nasa.gov/MODISA/Mapped/' ...
    TimeResolution '/' ...
    SpatialResolution '/chlora/'];

% some other available websites with data are
% (change the <TimeResolution> and <SpatialResolution> variables above
to access these files):
%DATAin = 'http://oceandata.sci.gsfc.nasa.gov/MODISA/Mapped/Monthly/
9km/chlora/';
%DATAin = 'http://oceandata.sci.gsfc.nasa.gov/MODISA/Mapped/Seasonal/
4km/chlora/';
%DATAin = 'http://oceandata.sci.gsfc.nasa.gov/MODISA/Mapped/Seasonal/
9km/chlora/';

% create "time" variable depending to TimeResolution

YEARS = 2002:2016;

if strcmp(TimeResolution, 'Monthly'),
    MONTHS = 1:12;
```

```

elseif strcmp(TimeResolution,'Seasonal'),
    MONTHS = 2:3:11;
end;

if strcmp(SpatialResolution,'4km'),
    my = 1440; % latitude dimension
    mx = 1680; % longitude dimension
elseif strcmp(SpatialResolution,'9km'),
    my = 720;
    mx = 840;
end;
m_month = length(MONTHS);
m_year = length(YEARS);

igb = single(-32767);
%%
%% %% create the output netCDF file if does not exist
FileOut = ['CCS_chl_' TimeResolution '_' SpatialResolution '.nc'];
%
if ~exist(FileOut,'file')
    % Create a new NC file.
    ncidd=netcdf.create(FileOut,'clobber');
    % put global attribution
    netcdf.putAtt(ncidd,-1,'Description','California Current System: MODIS
Level-3 Standard Mapped chlorophyll a '); %
    netcdf.putAtt(ncidd,-1,'Author','DyAnna R., Tetyana M. ');
    netcdf.putAtt(ncidd,-1,'Created',datestr(now));

    % define dimensions
    latdim=netcdf.defDim(ncidd,'lat',my);
    londim=netcdf.defDim(ncidd,'lon',mx);
    mondim=netcdf.defDim(ncidd,'month',m_month);
    yeardim=netcdf.defDim(ncidd,'year',m_year);

    % define variables
    latid=netcdf.defVar(ncidd,'latitude','float',latdim);
    lonid=netcdf.defVar(ncidd,'longitude','float',londim);
    monid=netcdf.defVar(ncidd,'month','int',mondim);
    yearid=netcdf.defVar(ncidd,'year','int',yeardim);

    chlid=netcdf.defVar(ncidd,'Chlorophyll','float',[latdim,londim,mondim,y
eardim]);
    netcdf.putAtt(ncidd,chlid,'Description','Chlorophyll Concentration,
OCI Algorithm');
    netcdf.putAtt(ncidd,chlid,'units','mg m^-3');
    netcdf.putAtt(ncidd,chlid,'scale_factor',1);
    netcdf.putAtt(ncidd,chlid,'missing_value',igb);
    netcdf.putAtt(ncidd,chlid,'add_offset',0);

    % end define variable
    netcdf.endDef(ncidd);

    % Write some Variables

```

```

netcdf.putVar(ncidd,yearid,YEARS);
netcdf.putVar(ncidd,monid,MONTHS);
netcdf.close(ncidd);
else
    ncidd=netcdf.open(FileOut,'nowrite');
    chlid=netcdf.inqVarID(ncidd,'Chlorophyll');
    latid=netcdf.inqVarID(ncidd,'latitude');
    lonid=netcdf.inqVarID(ncidd,'longitude');
    netcdf.close(ncidd);
end;

%%

FileIn = 'checksum.txt'; % this file contains names of all files
available to download

urlwrite([DATAin FileIn],FileIn);

CS = importdata(FileIn);

TOTAL = 0; % will count uploaded files
%for k = 1:length(CS),

ncidd=netcdf.open(FileOut,'write');

Nff = [];

for k = 1:length(CS),
    disp(k)
    CS1 = CS{k};
    if strfind(CS1,'.nc')
        try
            p = strfind(CS1,' ');

            FileName = CS1(p(end)+1:end);

            urlwrite([WEBdata FileName], FileName)

            nid = netcdf.open(FileName,'nowrite');
            lonid_i = netcdf.inqVarID(nid,'lon');
            latid_i = netcdf.inqVarID(nid,'lat');
            chlid_i = netcdf.inqVarID(nid,'chlor_a');
            CHL = netcdf.getVar(nid,chlid_i);
            CHL(CHL==netcdf.getAtt(nid,chlid_i,'_FillValue')) = NaN;
            CHL = double(CHL);
            LON = netcdf.getVar(nid,lonid_i);
            LON(LON==netcdf.getAtt(nid,lonid_i,'_FillValue')) = NaN;
            LON = double(LON);
            LAT = netcdf.getVar(nid,latid_i);
            LAT(LAT==netcdf.getAtt(nid,latid_i,'_FillValue')) = NaN;
            LAT = double(LAT);

            TITLE = netcdf.getAtt(nid,netcdf.getConstant('NC_GLOBAL'),'title');

```

```

    time_coverage_start =
netcdf.getAtt(nid,netcdf.getConstant('NC_GLOBAL'),'time_coverage_start'
);
    time_coverage_end =
netcdf.getAtt(nid,netcdf.getConstant('NC_GLOBAL'),'time_coverage_end');
    SR =
netcdf.getAtt(nid,netcdf.getConstant('NC_GLOBAL'),'spatialResolution');
    CHL_units = netcdf.getAtt(nid,chlid_i,'units');

netcdf.close(nid)
delete(FileName)

TIME1 = datenum(time_coverage_start(1:10));
TIME2 = datenum(time_coverage_end(1:10));
TIMEvec = datevec(mean([TIME1 TIME2]));

YEARout = TIMEvec(1);
MONTHout = TIMEvec(2);

Ilon = find((LON>=CA.LonLimit(1)) & (LON<=CA.LonLimit(2)));
Ilat = find((LAT>=CA.LatLimit(1)) & (LAT<=CA.LatLimit(2)));

LONout = LON(Ilon);
LATout = LAT(Ilat);
CHLout = CHL(Ilon,Ilat);
CHLout(isnan(CHLout)) = igb;

netcdf.putVar(ncidd,latid,LATout);
netcdf.putVar(ncidd,lonid,LONout);
netcdf.putVar(ncidd,chlid,[0,0,MONTHout-1,YEARout-
YEARS(1)], [my,mx,1,1],single(CHLout'));

TOTAL = TOTAL + 1;
sprintf('%5s : %s year: %s month: %s',int2str(TOTAL), FileName,
int2str(YEARout), int2str(MONTHout))
catch ME
Nff = [Nff k];
end
end
end

netcdf.close(ncidd)
return

```

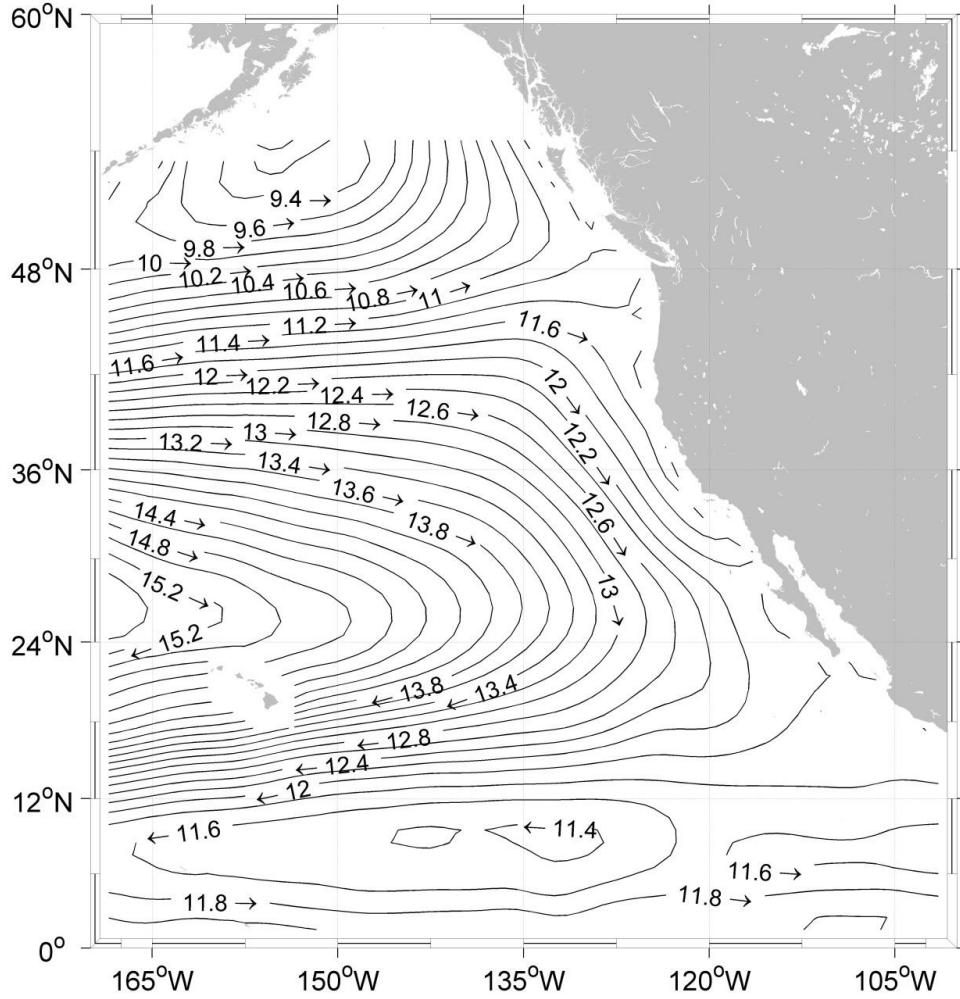
## IV. RESULTS AND DISCUSSION

Results and discussion are organized in a similar format to Chapter III with acceleration potential described first and Chl-a second. Although Synoptic Monthly Anomaly was the focus of this research in determining inter-annual variability, additional information is provided from composite analysis to gain a better overall picture and more complete comparative analysis of the differences between seasonal and non-seasonal fluctuations in the CCS. For both acceleration potential and Chl-a Total Time Mean as well as Climatological Monthly Anomaly is shown and described. Next, the EOF analysis to include Modes and PC analysis for Synoptic Monthly Anomaly is shown and described. Finally, the comparison of acceleration potential and Chl-a EOF analysis to climatological indices, EMI and MEI are described.

### A. TOTAL TIME MEAN FOR ACCELERATION POTENTIAL ( $\bar{\bar{\psi}}$ )

Total Time Mean is calculated for acceleration potential ( $\bar{\bar{\psi}}$ ) using Equation (6). Results are shown in Figure 14. The black lines indicate streamlines and the arrows represent the overall flow pattern. Tighter spacing between streamlines represents higher geostrophic velocity, as seen between 36°N–42°N, 165°W–150°W. Streamlines of wider spacing are regions of slower velocities as seen in 48°N–54°N, 165°W–150°W. It is important to note the blank area between 54°N and 60°N is a result of the isopycnal surface outcropping in some months, for more detail see Chapter III.

Figure 14. Total Time Mean for Acceleration Potential at the 26.9 kg/m<sup>3</sup> Isopycnal Surface ( $\bar{\bar{\psi}}$ ).



This image is Total Time Mean ( $\bar{\bar{\psi}}$ ) of the acceleration potential for the SMG-WOD data over a period of 1945–2014 at  $\sigma = 26.9 \text{ kg/m}^3$ . Labels are in J/kg. Note, that the arrow is only shown the flow direction and has not been scaled to the flow speed.

Three major features are identifiable in Figure 14, the southern part of the cyclonic Alaska Gyre, seen north of 42°N, the anticyclonic North Pacific Gyre, between 12°N and 43°N, and the northern portion of the cyclonic circulation in the northern tropical Pacific, between 0°N and 10°N. These North Pacific circulation patterns are well known and agree with earlier studies of large scale acceleration potential fields, for example Castro et al. (2001). Castro et al. (2001) used temperature and salinity data from Point Sur Cruises (1988–1990), WOCE cruises (1985, 1989, 1991, 1993, and 1994),



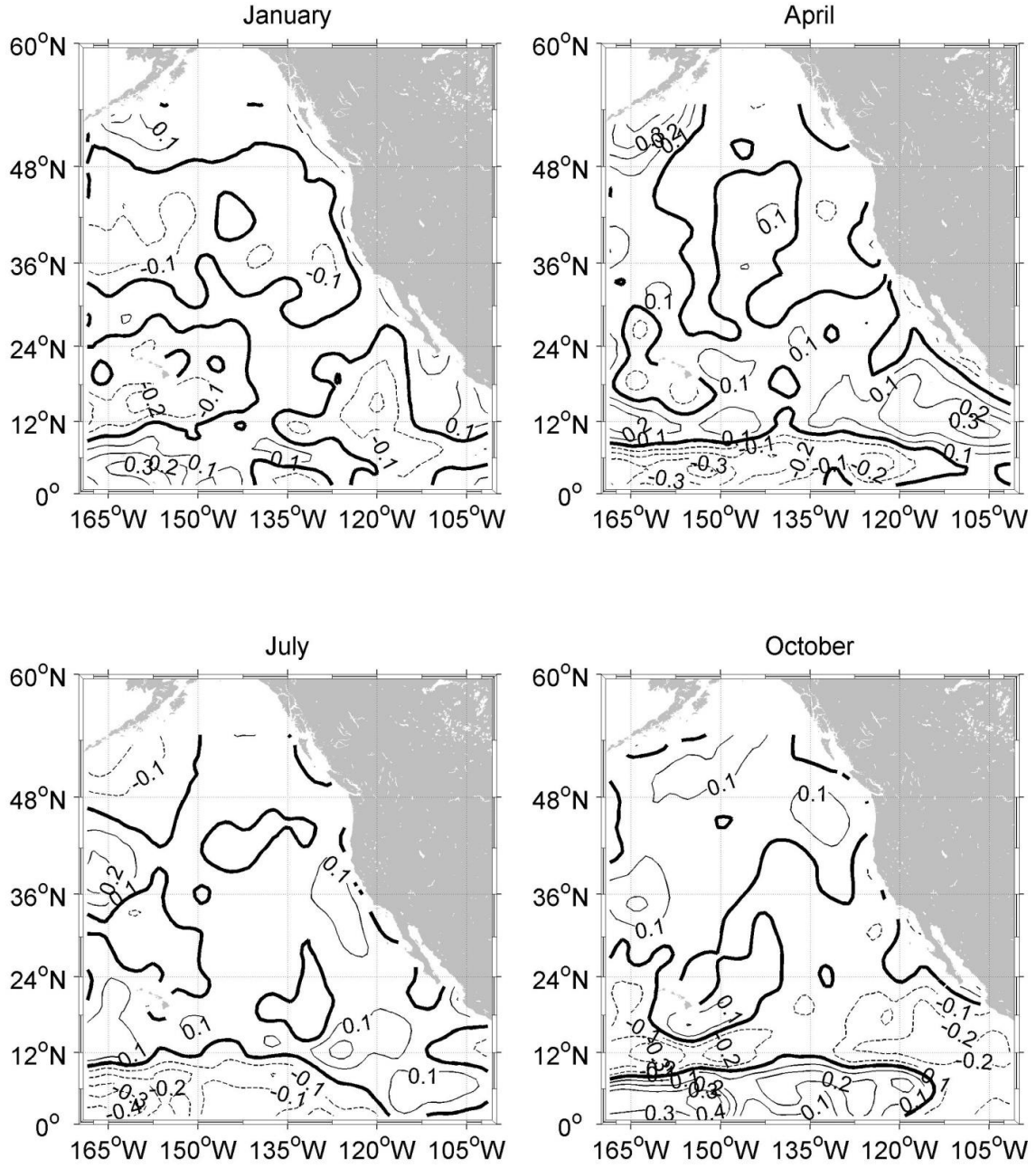
British Columbia Cruise May 10–14, 1990, Baja California Cruises 1970–1984, eastern tropical North Pacific (ETNP, 0°–30°N , 166°W–104°W), and Cruise January–July 1977. The similarities of Figure 14 and Castro et al. (2001) show well resolved large scale circulation patterns of the cyclonic Alaska Gyre and anticyclonic North Pacific Gyre. However, in Castro et al. (2001) the northern Pacific tropical cyclonic circulation is not as well identified, as compared to Figure 14, but the cyclonic circulation is very well defined. This is as a result of more years being averaged than in Castro et al. (2001) research in addition to higher spatial and temporal horizontal resolutions (1°x1°) utilized in this research from the SMG-WOD. Castro et al. (2001) acceleration potential results identify coastal features and circulations. In Figure 14, there is no signature of poleward motion along the West Coast of North America indicative of the CU or DC. This is expected in the current research, due to the limitation of horizontal resolution near the coast thus an expected discrepancy between the two fields. However, Castro et al. (2001) make note of the coastal features identified and specifically the poleward flow of water from Baja California, Mexico to British Columbia. The poleward current, in Castro et al. (2001), is identified as the CU due to its northward velocity and the water characteristics. Furthermore, an offshore current is identified as the CC as a result of its velocity direction and water characteristic matching that of the CC.

## **B. CLIMATOLOGICAL MONTHLY ANOMALY FOR ACCELERATION POTENTIAL ( $\tilde{\psi}$ )**

The Climatological Monthly Anomaly ( $\tilde{\psi}$ ) was calculated using Equation (7) and it is a deviation of Climatological Monthly Mean ( $\bar{\psi}$ ) from the Total Time Mean ( $\bar{\bar{\psi}}$ ). This field indicates mean seasonal variability from 1945 to 2014 and is calculated for each month. Figure 15 displays only four of the 12 months to highlight changes from one season to the next; Appendix A contains all 12 months. Only four months are described to represent the average condition in each of the seasons. The x and y axes are latitude and longitude respectively. The thick black lines indicate 0 J/kg meaning no departure from the seasonal mean. The thin black lines are streamlines and indicate deviation from the seasonal mean of geostrophic flow. The numerical values on the streamlines are acceleration potential in J/kg. The higher the value of acceleration potential indicates

higher departure from the climatological mean and the smaller the acceleration potential indicates less departure. A solid streamline indicates a positive acceleration potential anomaly and a dashed streamline indicates a negative acceleration potential anomaly. The maximum value of  $-0.4 \text{ J/kg}$  is seen in April between  $48^\circ\text{N}$  and  $54^\circ\text{N}$  along the Aleutian Islands and minimum acceleration potential of  $0.4 \text{ J/kg}$  between  $0^\circ$  and  $6^\circ\text{N}$  in the southwest tropical Pacific.

Figure 15. Climatological Monthly Anomaly for Acceleration Potential ( $\tilde{\psi}$ ) (1945–2014).



Climatological Monthly Anomaly of the acceleration potential ( $\tilde{\psi}$ , Jkg-1) on the 26.9 isopycnal level with respect to 1000 dbar surface: (top left) January, (top right) April, (bottom left) July, and (bottom right) October calculated from 1945–2014 that total one image for each month. See Appendix A for all 12 months.

Each month displays patchy patterns with no identifiable large scale features consistent with the Total Time Mean ( $\bar{\bar{\psi}}$ ). The amplitudes of the seasonal variability demonstrate a strong zonal dependency with maximum values in the tropical region and smaller amplitudes in the subtropical domain. The weaker geostrophic circulation in the tropical region southward of 12°N (see Figure 14), exhibits higher amplitudes and gradients, as well as more structured spatial patterns of the seasonal variability (Figure 15). More random patches of lower seasonal variability are characteristic of strong geostrophic currents in the North Pacific Subtropical Gyre (compare Figures 14 and 15).

In addition, the Climatological Monthly Anomaly ( $\tilde{\psi}$ ) is more than one order of magnitude smaller than the Total Time Mean ( $\bar{\bar{\psi}}$ ). This means that the CCS has weak seasonal variability, or in other words, the geostrophic circulation does not deviate very much within a year. The reason for the low seasonal variability given the highly variable seasonal fluctuations of the CCS may be attributed to the horizontal resolution along the coast and the inability to pick up the coastal fluctuations of upwelling, downwelling, and flow reversal of the CU and DC in the winter season.

### **C. EOF ANALYSIS FOR ACCELERATION POTENTIAL SYNOPTIC MONTHLY ANOMALY ( $\hat{\psi}$ )**

The EOF analysis was conducted on the Synoptic Monthly Anomaly ( $\hat{\psi}$ ) for acceleration potential, which is the deviation of the acceleration potential field from the Climatological Monthly Mean ( $\bar{\psi}$ ) and characterizes inter-annual variability. As described in Chapter III, the EOF analysis allows for separating a time-series of the two-dimensional acceleration potential field into its temporal (PCs) and spatial (EOF Modes) components. The EOF Modes represent the spatial patterns of the acceleration potential Synoptic Monthly Anomaly ( $\hat{\psi}$ ) that capture its maximum variance within the northern eastern Pacific region. The variance captured by the first six EOFs is shown in Table 6. In the current research, the analysis effort was concentrated on the Mode 1 and Mode 2. Mode 1 contained 35% of the total variance; which means about one third of the total inter-annual variability will be represented in this mode. Mode 2 contained 22% of the total variance. Mode 1 and Mode 2 combined contain 57% of the total variance

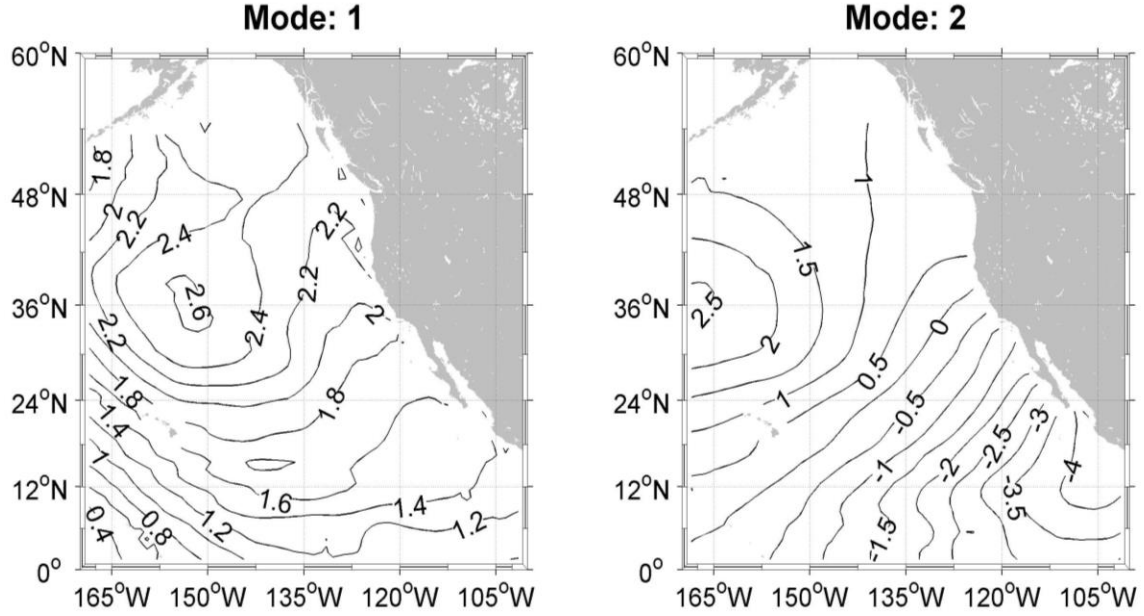
suggesting that over half of the inter-annual variability is represented in the first two Modes. The higher modes were not significant for identifying important patterns in the data.

Table 6. Variances of the First Six Leading EOFs of Synoptic Monthly Anomaly ( $\hat{\psi}$ ).

EOF $\hat{\psi}$	Variance	Cumulative Variance
1	0.35	0.35
2	0.22	0.57
3	0.13	0.70
4	0.09	0.79
5	0.06	0.85
6	0.06	0.91

Figure 16 represents EOF Mode 1 (left panel) and Mode 2 (right panel). The black lines are streamlines that represent patterns of inter-annual variability in geostrophic flow. Each Mode, when multiplied by a corresponding PC, indicates differences in the overall geostrophic flow characteristics such as intensity and direction for North Pacific and correspondingly on the CC. Tighter spacing of streamlines is representative of faster geostrophic flow. Wider spacing of streamlines is representative of slower geostrophic flow. The numerical values on the streamlines are acceleration potential in J/kg. The higher the value of acceleration potential indicates higher departure from the climatological mean and the smaller the acceleration potential indicates less departure.

Figure 16. EOF Mode 1 and Mode 2 from Acceleration Potential Synoptic Monthly Anomaly ( $\hat{\psi}$ ).



This image shows the first 2 EOF Modes of Synoptic Monthly Anomaly ( $\hat{\psi}$ ), at the acceleration potential ( $\hat{\psi}$ ,  $\text{J kg}^{-1}$ ) on the 26.9 isopycnal level with respect to 1000 dbar surface. The spacing of the isolines has been chosen as to better represent the spatial patterns in each EOF, and is equal to 0.1  $\text{J/kg}$  for Mode 1 and 0.5  $\text{J/kg}$  for Mode 2.

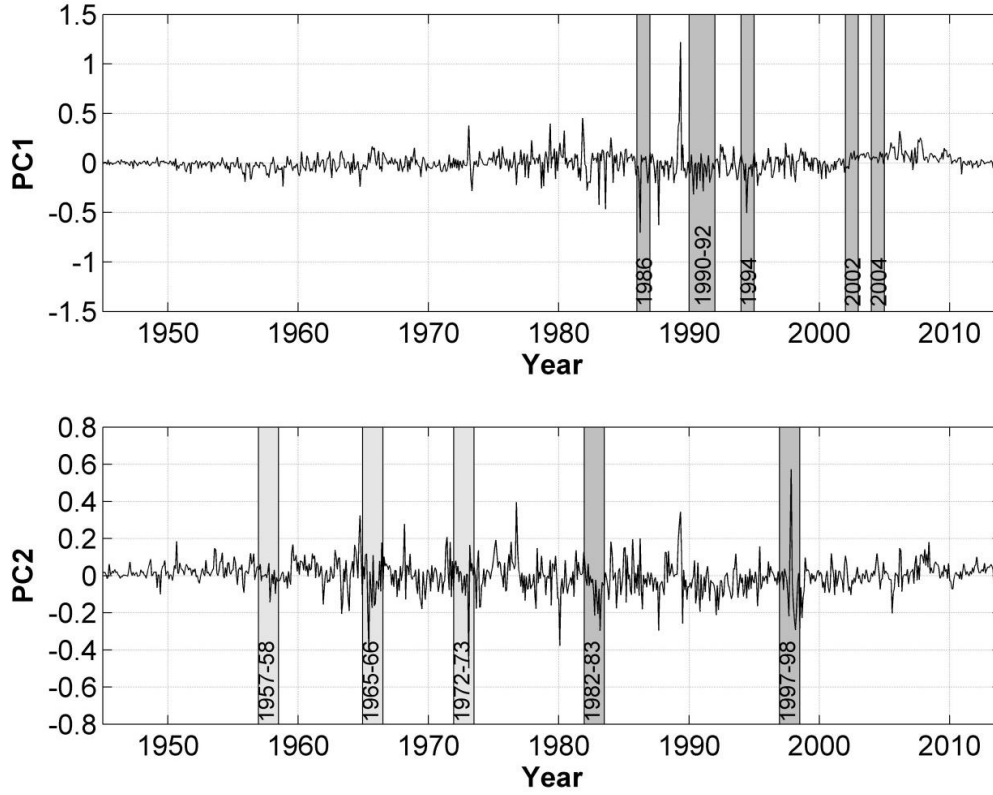
In Mode 1, (left panel in Figure 16) the tightest packing of streamlines is between 0°–18°N, 165°W–150°W also southwest of the closed streamline located at 24°N–36°N, 165°W–150°W. The widest spacing of streamlines in Mode 1 is between 6°N–24°N, 135°W–105°W. In EOF Mode 1, the highest acceleration potential 2.6  $\text{J/kg}$  is along the closed streamline near 36°N–40°N, 163°W–145°W and the lowest acceleration potential is 0.3  $\text{J/kg}$  located west of 165°N and at 0°. The 2.6  $\text{J/kg}$  closed streamline is located in the vicinity of the North Pacific Gyre and represents strengthening of the geostrophic flow of the gyre and consequently increasing the CC velocity for positive PC1. In the negative phase, the EOF Mode 1 pattern will weaken the acceleration potential gradients and thus decrease the geostrophic velocity in the CC. The intensity of the CC geostrophic flow is related to EOF Mode 1, due to the proximity of the closed streamline in relation to the North Pacific Gyre. As the streamlines get closer together the pressure gradient

increases and the geostrophic flow will thus increase. As the geostrophic flow increases in the North Pacific Gyre, the acceleration potential of the CC is also affected and will increase the geostrophic flow of the CC. Therefore the EOF Mode 1 represents the strengthening or weakening of the CC.

In Mode 2 (right panel in Figure 16) the tightest concentration of streamlines for Mode 2 is perpendicular to the coast of North America between 12°N–24°N, 125°W–105°W. The widest spacing of the streamlines is located in the northern Pacific, north of 30°N. For EOF Mode 2, highest acceleration potential is 2.5 J/kg and is located 36°N and 165°W, and the lowest acceleration potential anomaly is -4 J/kg located south of Baja California, Mexico at 6°N–24°N, 105°W. The positive phase of the geostrophic flow pattern indicates offshore flow and consequently coastal upwelling within the CC. The offshore or onshore geostrophic flow is determined by the location of the maximum and minimum values of the acceleration potential anomaly, after the EOF Mode is multiplied by a corresponding principal component. In a positive phase, there is a general pattern of offshore flow, with high acceleration potential value (2.6 J/kg) on the right, and lower acceleration values (-0.04 J/kg) on the left. The offshore flow in the anomaly field is also associated with enhanced upwelling in the coastal region of the CC. A negative phase represents a general pattern of the onshore flow, with higher acceleration potential anomaly values (up to 0.04 J/kg) to the right, and lower acceleration potential anomaly values (-2.6 J/kg) to the left. This pattern is associated with reduced upwelling or downwelling in the coastal region of the CC.

The EOF PC represents the temporal component of the acceleration potential Synoptic Monthly Anomaly ( $\hat{\psi}$ ). Figure 17 is a time series for the EOF PC computed for the acceleration potential Synoptic Monthly Anomaly ( $\hat{\psi}$ ). For both graphs the y axis represents the respective PC and the x axis represents the time in years. The grey horizontal lines on PC1 (Figure 17 top panel) indicate years of El Nino Modoki events and on PC2 (Figure 17 bottom panel) indicate years of strong El Nino events. In both graphs, the amplitudes are fairly low from 1945 to 1960. In addition, the MEI does not start calculating until 1950 due to the insufficient data available for accurate calculations of the index.

Figure 17. EOF Analysis of PC1 and PC2 from Acceleration Potential Synoptic Monthly Anomaly ( $\hat{\psi}$ ).



This image shows the first 2 PCs of Climatological Monthly Anomaly of the acceleration potential ( $\hat{\psi}$ ) on the 26.9 isopycnal level with respect to 1000 dbar surface.

PC1 has a maximum value of 1.2 and a minimum value of -0.6, see Figure 17. When PC1 is positive, the spatial variability or the respective EOF Mode 1 of acceleration potential signifies an anticyclonic gyre that strengthens the North Pacific Gyre and consequently enhances the CC, meaning the geostrophic flow anomaly is stronger. When PC1 is negative, the spatial variability of the acceleration potential represents a cyclonic gyre that weakens the geostrophic flow of the North Pacific Gyre and consequently reduces the geostrophic flow in the CC or in other words the acceleration potential anomaly is smaller.



Calculating the contribution of EOF Mode 1 to acceleration potential mean field is estimated as

$$\max \left[ PC_1(\tilde{t}_p) E_1(\mathbf{r}_i) \right] - \min \left[ PC_1(\tilde{t}_p) E_1(\mathbf{r}_i) \right]. \quad (11)$$

Since EOF Mode 1 has positive values at all points in the spatial domain, see Figure 16, than the calculation is,

$$\max_{(i,r)} \left[ PC_1(\tilde{t}_p) E_1(\mathbf{r}_i) \right] = \max_i \left[ PC_1(\tilde{t}_p) \right] \cdot \max_r \left[ E_1(\mathbf{r}_i) \right] = 1.2 \cdot 2.6 \text{ J/kg} = 3.12 \text{ J/kg}; \quad (12)$$

and,

$$\min_{(i,r)} \left[ PC_1(\tilde{t}_p) E_1(\mathbf{r}_i) \right] = \min_i \left[ PC_1(\tilde{t}_p) \right] \cdot \max_r \left[ E_1(\mathbf{r}_i) \right] = -0.6 \cdot 2.6 \text{ J/kg} = -1.56 \text{ J/kg}; \quad (13)$$

therefore,

$$3.21 \text{ J/kg} - (-1.56 \text{ J/kg}) = 4.68 \text{ J/kg}. \quad (14)$$

The Climatological Monthly Anomaly ( $\tilde{\psi}$ ) or seasonal variability, was calculated using Equation (12) and the absolute value of 0.04 J/kg, see Figure 15, giving

$$2(0.4 \text{ J/kg}) = 0.8 \text{ J/kg}. \quad (15)$$

The magnitude of inter-annual variability ( $\hat{\psi}$ ) (4.86 J/kg) is much larger compared to the seasonal variability ( $\tilde{\psi}$ ) (0.8 J/kg) as discussed in the previous subsection.

PC2 has a maximum value of 0.55 and a minimum value of -0.50, see Figure 17. When PC2 is positive, the spatial variability of acceleration potential represents offshore geostrophic flow that enhances coastal upwelling, meaning the upwelling of the CC is increased. When PC2 is negative, the spatial variability of acceleration potential represents onshore geostrophic flow that suppresses the coastal upwelling or enhances coastal downwelling, meaning the downwelling is more apparent in the coastal region of the CC, and potentially the DC as a surface expression of the CU may be present.

Calculating the contributions of EOF Mode 2 to acceleration potential mean field is different than the calculation for EOF Mode 1 since it can exhibit both positive and negative values; the extremes are estimated as

$$\begin{aligned}
\max_{\tilde{t}_p} [PC_2(\tilde{t}_p)] \cdot \max_{\mathbf{r}} [E_2(\mathbf{r}_i)] &= 0.55 \cdot 2.50 \text{ J/kg} = 1.38 \text{ J/kg}; \\
\min_{\tilde{t}_p} [PC_2(\tilde{t}_p)] \cdot \min_{\mathbf{r}} [E_2(\mathbf{r}_i)] &= -0.50 \cdot (-4.00 \text{ J/kg}) = 2.00 \text{ J/kg}; \\
\max_{\tilde{t}_p} [PC_2(\tilde{t}_p)] \cdot \min_{\mathbf{r}} [E_2(\mathbf{r}_i)] &= -0.50 \cdot 2.50 \text{ J/kg} = -1.25 \text{ J/kg}; \\
\min_{\tilde{t}_p} [PC_2(\tilde{t}_p)] \cdot \max_{\mathbf{r}} [E_2(\mathbf{r}_i)] &= 0.55 \cdot (-4.00 \text{ J/kg}) = -2.20 \text{ J/kg}.
\end{aligned} \tag{16}$$

The magnitude of EOF Mode 2 is equal to

$$2.0 - (-2.2) = 4.2 \text{ J/kg}, \tag{17}$$

which is comparable to the magnitude of EOF Mode 1 and is still significantly larger than the maximum seasonal variability ( $\tilde{\psi}$ ).

#### **D. CORRELATIONS BETWEEN PRINCIPAL COMPONENTS AND CLIMATOLOGICAL INDICES**

There is a connection between inter-annual acceleration potential in the CCS and climate variability. The connection is represented by the correlation coefficients (Chapter III) between the climate indices EMI and MEI and the acceleration potential PC1 and PC2.

At the 0.05 significance level, a correlation coefficient of -0.15 was calculated between PC1 and EMI. This statistically significant (but not strong) negative correlation suggests that during an El Nino Modoki event (positive EMI), PC1 will have a negative value. The environmental forcing with a positive EMI corresponds to the warming of the tropical central Pacific (El Nino Modoki indication) that causes lower gradients of the acceleration potential field. The lower gradients cause a weaker North Pacific Gyre (negative PC1). A weaker North Pacific Gyre causes slowing of the geostrophic flow in the CC.

The environmental forcing with a negative EMI corresponds to tropical central Pacific not warming (no indication of El Nino Modoki conditions) that causes higher gradients of the acceleration potential field. A higher pressure gradient causes a stronger

North Pacific Gyre (positive PC1). A stronger North Pacific Gyre causes increased geostrophic flow in the CC.

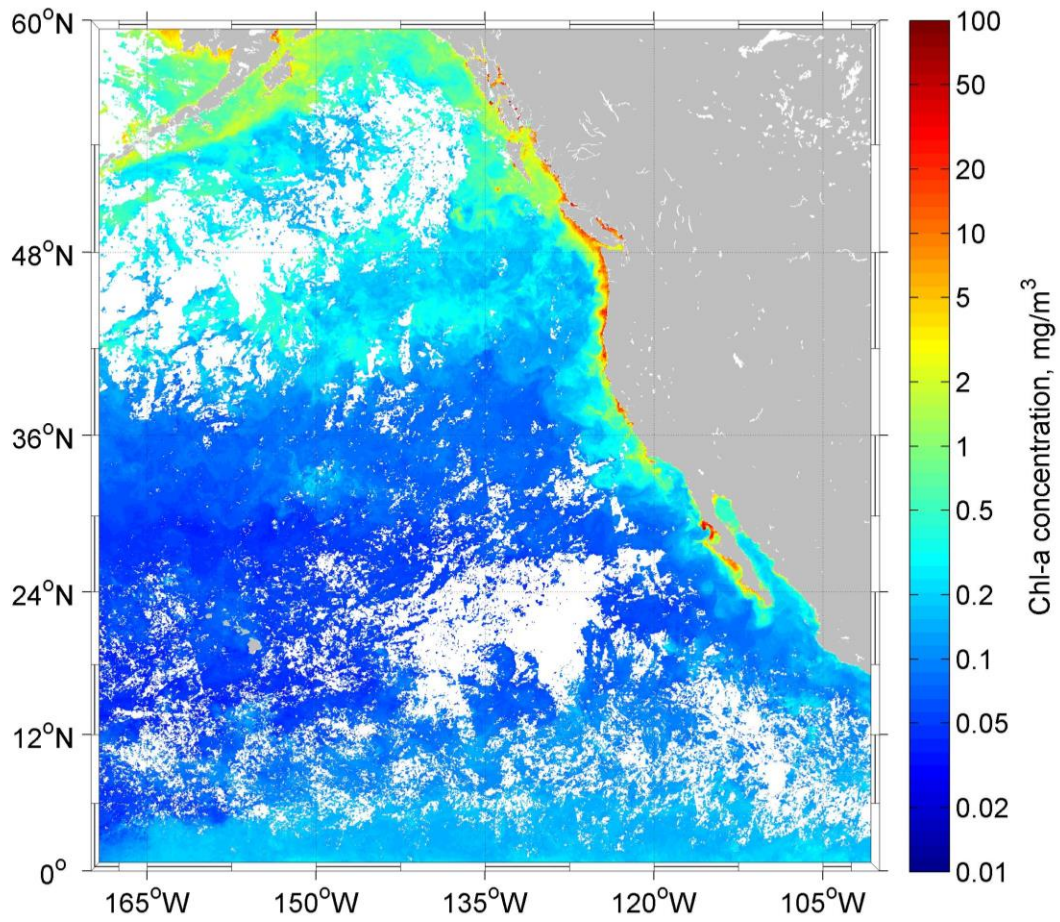
There was a correlation coefficient of -0.31 between PC2 and MEI at the 0.05 significance level, also indicating negative (statistically significant but not strong) correlation. This suggests that a positive MEI, when El Nino signatures are present, PC2 will have a negative value. The environmental forcing with a positive MEI corresponds to warming of the tropical eastern Pacific. The warming of the tropical eastern Pacific causes onshore geostrophic flow anomaly (negative PC2). Onshore geostrophic flow leads to coastal downwelling or reduced upwelling in the CC.

The environmental forcing with a negative MEI corresponds to tropical eastern Pacific with cooler waters. The cooler tropical eastern Pacific causes offshore geostrophic flow anomaly (positive PC2). Offshore geostrophic flow anomaly leads to enhanced coastal upwelling in the CC.

#### **E. COMPOSITE ANALYSIS FOR CHLOROPHYLL-A CONCENTRATION**

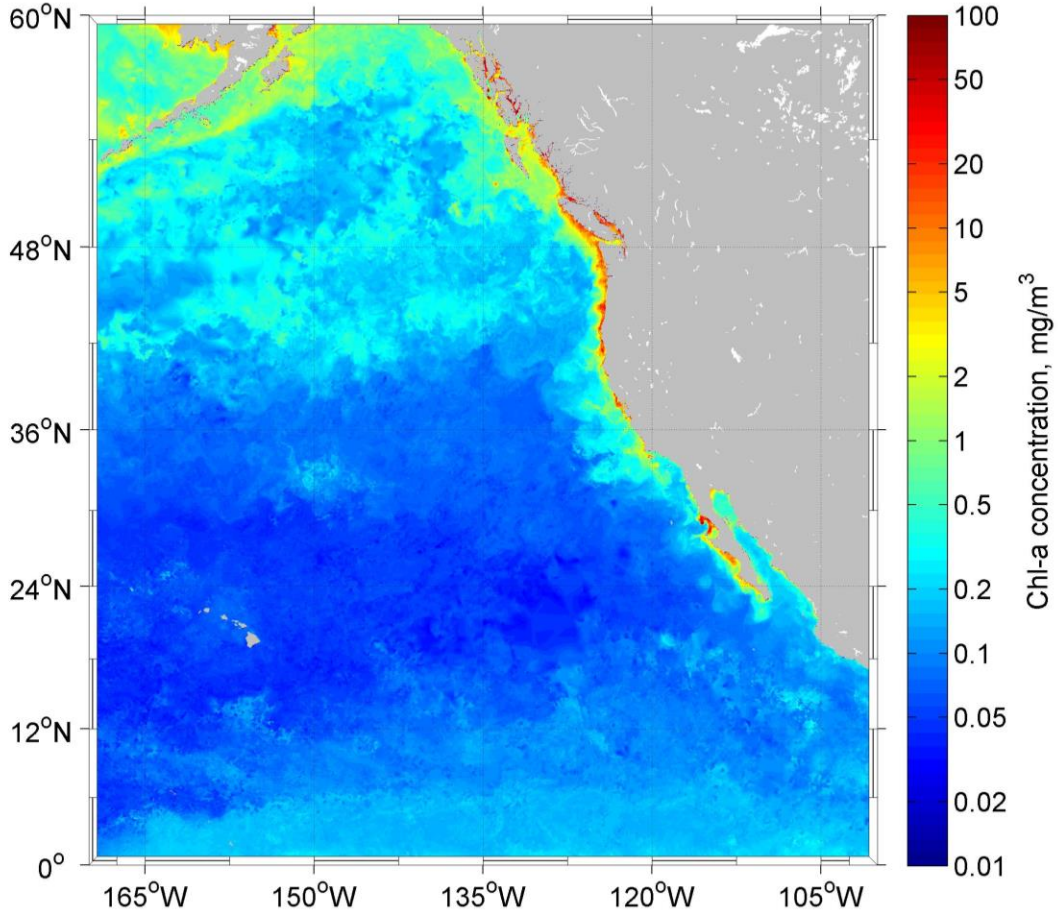
In order to resolve the coastal resolution of the SMG-WOD temperature and salinity dataset, Chl-a was obtained from MODIS-A. The product of the raw satellite data had sporadic areas of missing data due to environmental factors (indicated by white areas in Figure 18) that limited the measurement of the surface Chl-a from the MODIS-A satellite. Figure 18 shows the raw data downloaded from the website, white areas are very noticeable and limit the ability to easily analyze the image. In Figure 18, the color bar indicates actual Chl-a concentration in  $\text{mg}/\text{m}^3$  on a logarithmic scale. Warm colors (red and orange) indicate higher concentration, cool colors (green and blue) indicate lower concentrations, grey indicates land and white indicates areas where no data is available. For an in depth descriptions of limiting factors see Chapter III. Interpolation was used to fill in the white areas to provide a consistent image of the Chl-a concentration for better analysis and to avoid bias being introduced into the fields following the composite and EOF analysis, Figure 19. All the parameters are the same in Figure 19.

Figure 18. Raw Chl-a Concentration Data for July 2002.



Environmental factors such as a cloud, snow, sea ice, sun glint, and aerosol concentration impede the satellite's ability to obtain surface Chl-a concentration. These regions are indicated by the white.

Figure 19. Interpolated Chl-a Concentration Data for July 2002.



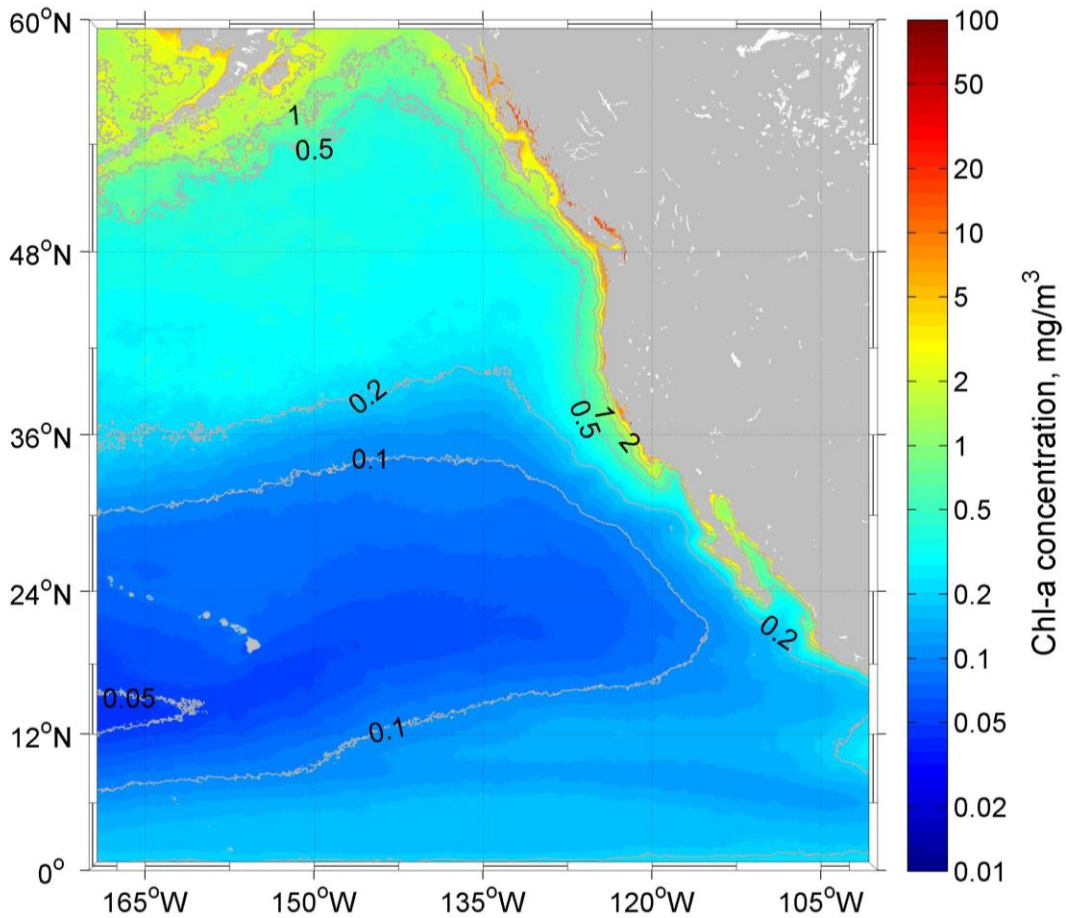
An interpolation procedure has been applied to the raw MODIS-A Chl-a concentration field, Figure 18, to fill in data gaps for further analysis.

#### F. TOTAL TIME MEAN FOR CHLOROPHYLL-A CONCENTRATION ( $\bar{\bar{C}}$ )

Total Time Mean is calculated for Chl-a concentration ( $\bar{\bar{C}}$ ) using Equation (6), with the exception of Chl-a in place of acceleration potential, results are shown in Figure 20. The color bar indicates Chl-a concentration with warm colors signifying higher concentration and cool colors signifying lower concentration on a logarithmic scale. The light grey lines are lines of constant Chl-a concentration in  $\text{mg/m}^3$  with  $0.1 \text{ mg/m}^3$

spacing. The highest Chl-a concentration occurs along the coast of North America from the Aleutian Islands south to Baja California, Mexico. The highest Chl-a concentration seen is  $13 \text{ mg/m}^3$  near San Francisco Bay and Monterey Bay at  $36^\circ\text{N}$ – $42^\circ\text{N}$ ,  $125^\circ\text{W}$ – $120^\circ\text{W}$ . In addition, the highest change of concentration also occurs along the coast. The lower Chl-a concentrations are observed in the central Pacific between  $6^\circ\text{N}$ – $30^\circ\text{N}$ ,  $165^\circ\text{W}$ – $110^\circ\text{W}$  with the lowest located  $12^\circ\text{N}$ – $18^\circ\text{N}$ ,  $165^\circ\text{W}$ – $155^\circ\text{W}$  with a value less than  $0.05 \text{ mg/m}^3$ .

Figure 20. Total Time Mean for Chl-a ( $\bar{\bar{C}}$ ) (2002-2014).



Total Time Mean of the Chl-a ( $\bar{\bar{C}}$ ) from MODIS-A data after interpolation was applied over a period of 2002–2014.

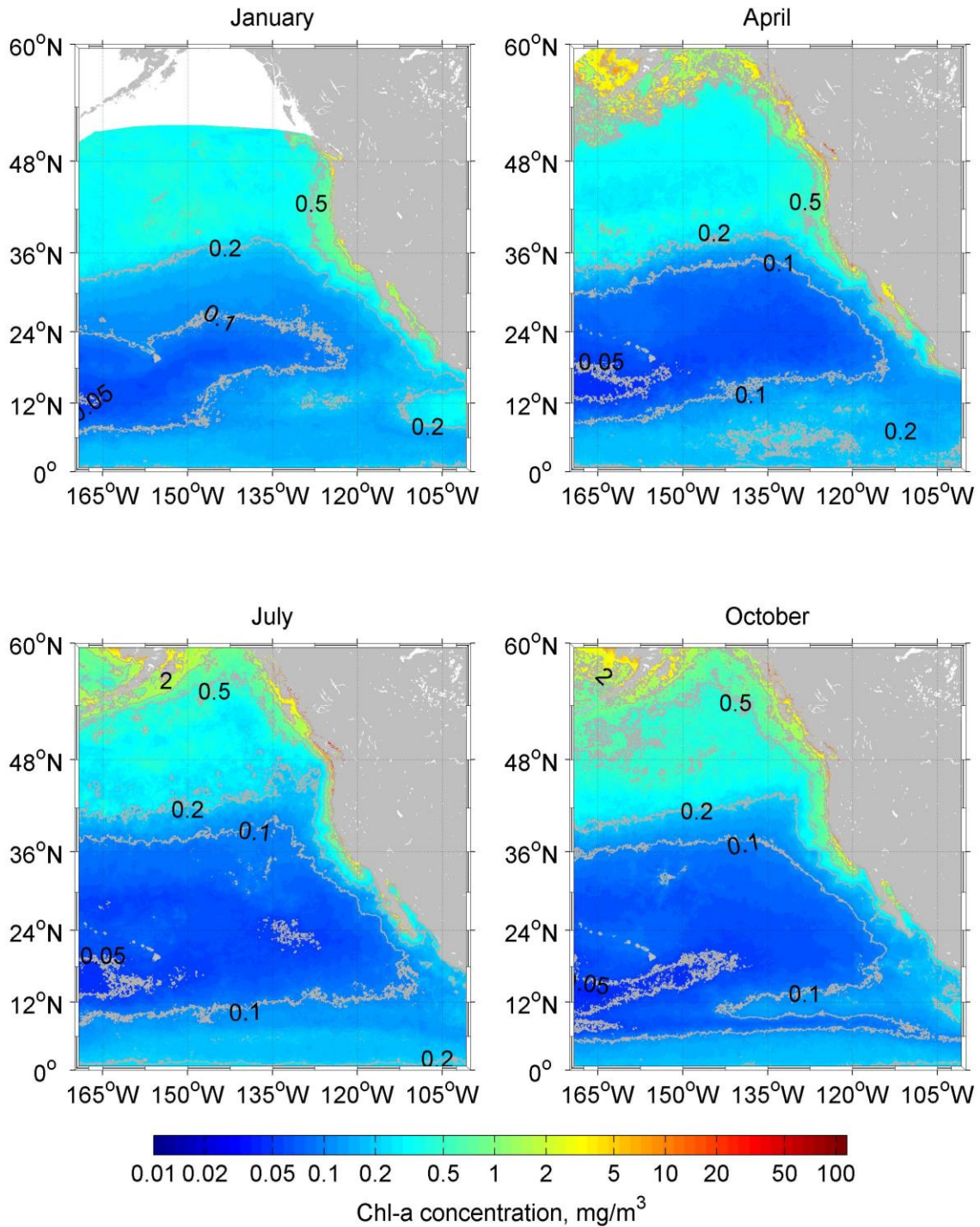
The three major features identified in the acceleration potential Total Time Mean ( $\overline{\overline{\psi}}$ ) are also visible in Figure 20. In the northern eastern Pacific, the cyclonic Alaska Gyre is identified north of 36°N. The cyclonic direction is distinguishable due to cyclonic gyres characterized by higher biological productivity resulting in increased surface Chl-a, for example see Talley (2011). Higher Chl-a concentration in cyclonic circulation is similar to the mechanics of coastal upwelling. With cyclonic circulation, there is surface divergence, as the surface waters are removed it is replaced by more nutrient rich subsurface waters, for example see Talley (2011). The maximum Chl-a in the Alaska Gyre is 0.4 mg/m<sup>3</sup>. In the central Pacific, the anticyclonic North Pacific Gyre is located between 6°N–30°N and extends east toward West Coast of North America. The anticyclonic direction is distinguishable due to anticyclonic gyres having a lower productivity resulting in lower Chl-a at the surface, for example see Talley (2011). The lower Chl-a is similar to the mechanics of coastal downwelling. In anticyclonic circulation, there is surface convergence that causes the surface waters to be pushed to deeper levels and limits high biological production, for example see Talley (2011). The minimum Chl-a in the North Pacific Gyre is consistent with the lowest value in the field, 0.04 mg/m<sup>3</sup>. The third major feature identified in Figure 20 is the northern portion of the cyclonic circulation in the northern tropical Pacific between 0°N–6°N. The cyclonic circulation in this region does not produce Chl-a values as high as the Alaska Gyre despite the cyclonic circulation as a result of the lower nutrient content in tropical regions, for example see Talley (2011). A significant difference between the acceleration potential Total Time Mean ( $\overline{\overline{\psi}}$ ) and Chl-a Total Time Mean ( $\overline{\overline{C}}$ ) is the high variability along the coast, which is expected as a result of higher spatial resolution (4 km) of the MODIS-A dataset. Another difference of the Chl-a Total Time ( $\overline{\overline{C}}$ ), is that the streamlines are not as smooth as in the acceleration potential, Figure 14. This is a result of a smaller time frame being averaged with Chl-a, 12 years as opposed to 70 years, and the higher spatial resolution.

## G. CLIMATOLOGICAL MONTHLY MEAN FOR CHLOROPHYLL-A ( $\bar{C}$ )

The Climatological Monthly Mean ( $\bar{C}$ ) was calculated using Equation (5) with the exception of Chl-a in place of acceleration potential. Climatological Monthly Mean ( $\bar{C}$ ) is a result of averaging for each month in all 12 years giving 12 total figures. To highlight the major seasonal differences January, April, July, and October are shown in Figure 21, all 12 months are in Appendix B. The color bar indicates Chl-a concentration in  $\text{mg}/\text{m}^3$  with warm colors signifying higher concentration and cool colors signifying lower concentration. The light grey lines are lines of constant Chl-a concentration in  $\text{mg}/\text{m}^3$ . In Figure 21, three major features can be identified, cyclonic Alaska Gyre, anticyclonic North Pacific Gyre, and the cyclonic circulation of the northern tropical Pacific. The maximum Chl-a concentration values are found along the coast from the Aleutian Islands south to Baja California, Mexico. This was expected and is the reason for the analysis of surface Chl-a concentration along the coast. In addition to the highest values observed along the coastline, the strongest gradient or largest change in concentration is found within a 100 kilometers from the coast line in all months. This is also anticipated as a result of the strong seasonal fluctuations in upwelling or downwelling and biological productivity in proximity to the coastline. The lowest concentration of Chl-a is found in the central Pacific, in the vicinity of the North Pacific Gyre where the value never goes below or above  $0.02 \text{ mg}/\text{m}^3$ . This is consistent with the expectation of the anticyclonic North Pacific Gyre maintaining lower Chl-a concentration due to its anticyclonic rotation and converging surface properties.



Figure 21. Climatological Monthly Mean for Chl-a Concentration ( $\bar{C}$ ) (2002–2014).



Climatological Monthly Mean of Chl-a concentration ( $\bar{C}$ ) for January (top left), April (top right), July (bottom left), and October (bottom right) calculated from 2002–2014 that total one image for each month. See Appendix B for all 12 months.

In Climatological Monthly Mean ( $\bar{C}$ ) it is important to note there are significant seasonal differences in Chl-a concentrations near the coastline in the CC but also in the Alaska Gyre, North Pacific Gyre, and the northern tropical region.

In the North Pacific Gyre, the Chl-a field is not well structured and has a small surface area as outlined by the  $0.1 \text{ mg/m}^3$  isoline. The area of the North Pacific Gyre will increase as the season progress toward summer. In January, (Figure 21 top left panel) the majority of the area is at a concentration level of  $0.1 \text{ mg/m}^3$  with a patch of lower concentration of  $0.05 \text{ mg/m}^3$  near  $12^\circ\text{N}$  and  $165^\circ\text{W}$ . The lower Chl-a concentration is a result of the North Pacific Gyre being an area of low biological production from anticyclonic rotation and surface waters being suppressed. As the season progress to spring, (April Figure 21 top right panel) the North Pacific Gyre increases in area both northward/southward and toward the east as indicated by the  $0.1 \text{ mg/m}^3$  isoline and now covers the area of  $10^\circ\text{N}$ – $30^\circ\text{N}$ ,  $111^\circ\text{W}$ – $165^\circ\text{W}$ . The Chl-a concentration for the majority of the enlarged area has remained the same with the exception of the  $0.05 \text{ mg/m}^3$  isoline area has increased toward the east and now covers  $12^\circ\text{N}$ – $18^\circ\text{N}$ ,  $150^\circ\text{W}$ – $165^\circ\text{W}$ . In summer, the North Pacific Gyre continues to increase and now covers an area of  $10^\circ\text{N}$ – $36^\circ\text{N}$ ,  $109^\circ\text{W}$ – $165^\circ\text{W}$ . The patch of  $0.05 \text{ mg/m}^3$  has remained about the same size, however, another area of the  $0.05 \text{ mg/m}^3$  has developed near  $24^\circ\text{N}$ ,  $135^\circ\text{W}$  and has extended to the coast of North America and follows the coastline. By October, (Figure 21 bottom right panel) the North Pacific Gyre has continued to increase in area and now covers from  $5^\circ\text{N}$ – $36^\circ\text{N}$ ,  $109^\circ\text{W}$ – $165^\circ\text{W}$ . The  $0.05 \text{ mg/m}^3$  isoline area is also elongated to the east, south of Hawaii. After October the size of the North Pacific Gyre decreases drastically to the area described in January, for images see Appendix B. The increasing area of the North Pacific Gyre during the summer is due to the predominating northwesterly wind that enhances the anticyclonic rotation and allows for the gyre to expand to the north, south, and east toward the coast.

The Alaska Gyre is highly variable in Chl-a concentration from month to month. In January, (Figure 21 top left panel), it is difficult to analyze the variability due to the missing data as a result of environmental factors limiting the surface measurement, however some Chl-a values are identifiable. South of  $48^\circ\text{N}$  the majority of the Chl-a concentration is around  $0.3 \text{ mg/m}^3$  with a few patchy areas of  $0.4 \text{ mg/m}^3$ . Spring is one of

the most productive seasons for the Alaska Gyre (Talley 2011). In April, (Figure 21 top right panel) is when the first indications of increased Chl-a are observed. The maximum Chl-a concentration is approximately 20 mg/m<sup>3</sup> seen along the Canadian coast. While most of the production is occurring along the coast, the open waters have maintained a consistent level of 0.3 mg/m<sup>3</sup>. The increase in Chl-a concentration is high and drastically changed during this period from increased solar radiation, and the increase of nutrients available after the winter season. As spring passes into summer, depicted in July, (Figure 21 bottom left panel) the Chl-a concentration has decreased, but is still significant with a maximum value of about 20 mg/m<sup>3</sup>; the average concentration level has decreased. The reason for the decrease in the Chl-a concentration despite incoming solar radiation is that most of the nutrients that are available during the spring have been consumed. The production rate cannot be sustained throughout the summer. The large difference between July and October (Figure 21 bottom right panel) is that the central region of the Alaska Gyre has more patches of higher Chl-a of 0.5 mg/m<sup>3</sup>. The Chl-a concentration in the central Alaska Gyre regions starts to grow in August through October (see Appendix B). This is due to the weakening in the North Pacific Gyre, which occurs in the winter, see for example Talley (2011). As the North Pacific Gyre circulation shrinks and retreats south, the Chl-a concentration increases slightly from month to month because the circulation of the Alaska Gyre has increased, filling in the area that was occupied by the opposing flow. These mechanics allow for the Chl-a to penetrate farther offshore. After October, the analysis of the Chl-a concentration becomes difficult as a result of data missing.

The CC region is no different than the other regions described. In January, (Figure 21 top left panel) the highest concentration of Chl-a is observed along the coast. The maximum value of 7 mg/m<sup>3</sup> is observed in the San Francisco Bay located at 37°N, 122°W. The minimum values are observed along the coast but further offshore with a value of 0.5 mg/m<sup>3</sup>. The Chl-a concentration closer to the coast appears to be following the topography, the bays and points, along the California coastline. This is common and expected, there are regions along the coastline where upwelling and biological production are more dominate (Talley 2011). These regions of enhanced upwelling occur even during periods where downwelling dominates the region. The most common locations of these upwelling sites

and regions of increased surface Chl-a is Point Conception, located at 34°N, 120°W, Monterey Bay, located at 37°N, 122°W, San Francisco Bay, located at 38°N, 122°W, and Cape Mendocino located at 42°N, 127°W (Talley 2011). Upwelling sites are most noticeable in winter because the predominating wind pattern shifts to southwesterly and coastal upwelling is not favored in most coastal regions. Off the coast of Washington, there is another region of high biological production and surface Chl-a, however this is as a result of increased nutrient availability from the outflow of river runoff. As the season progresses from winter into spring, the coastline region increases in biological production and increased surface Chl-a. The maximum value of Chl-a is 23 mg/m<sup>3</sup> observed near the San Francisco and Monterey Bay region located at 37–38°N, 122°W. The difference between the winter and spring is that the extent of the 0.5 mg/m<sup>3</sup> isoline area has decreased or moved toward the east, closer to the coast. During spring, the predominate wind regime is in the process of shifting back to northwesterly and promotes coastal upwelling by surface waters moving offshore, however in April, (Figure 21 top right panel) the costal offshore movement is suppressed. This is occurring concurrently with the North Pacific Gyre increasing in area and strength, as described and also as indicated by the decreased surface Chl-a within the North Pacific Gyre. As the North Pacific Gyre grows and strengthens over the summer, it compresses the CC toward the coast even more as indicated by the Chl-a 0.5 mg/m<sup>3</sup> isoline being pushed eastward in Figure 21 bottom left panel. In July, the coastal upwelling are in full effect, however the 0.5 mg/m<sup>3</sup> isoline has continued to be suppressed by the still strengthening and expanding North Pacific Gyre. Also visible are regions of increased Chl-a concentration from major upwelling sites as evident on Figure 21 bottom left panel near Point Conception (34°N, 120°W), San Francisco Bay (38°N, 122°W), and Cape Mendocino (42°N, 127°W). In fall, (Figure 21 bottom right panel) the northwesterly winds have relaxed and are moving toward the southwest direction that consequently impacts the North Pacific Gyre circulation and the width of the CC. In October, all responses to the shifting seasons are observed by decreased Chl-a values in the North Pacific Gyre and consequently the CC 0.5 mg/m<sup>3</sup> isoline is bulging westward. There are still significant Chl-a values near the coast with the highest value of 18 mg/m<sup>3</sup> located in

the San Francisco and Monterey Bay region (37–38°N, 122°W) that indicates the region is still impacted by upwelling and contains nutrient rich waters.

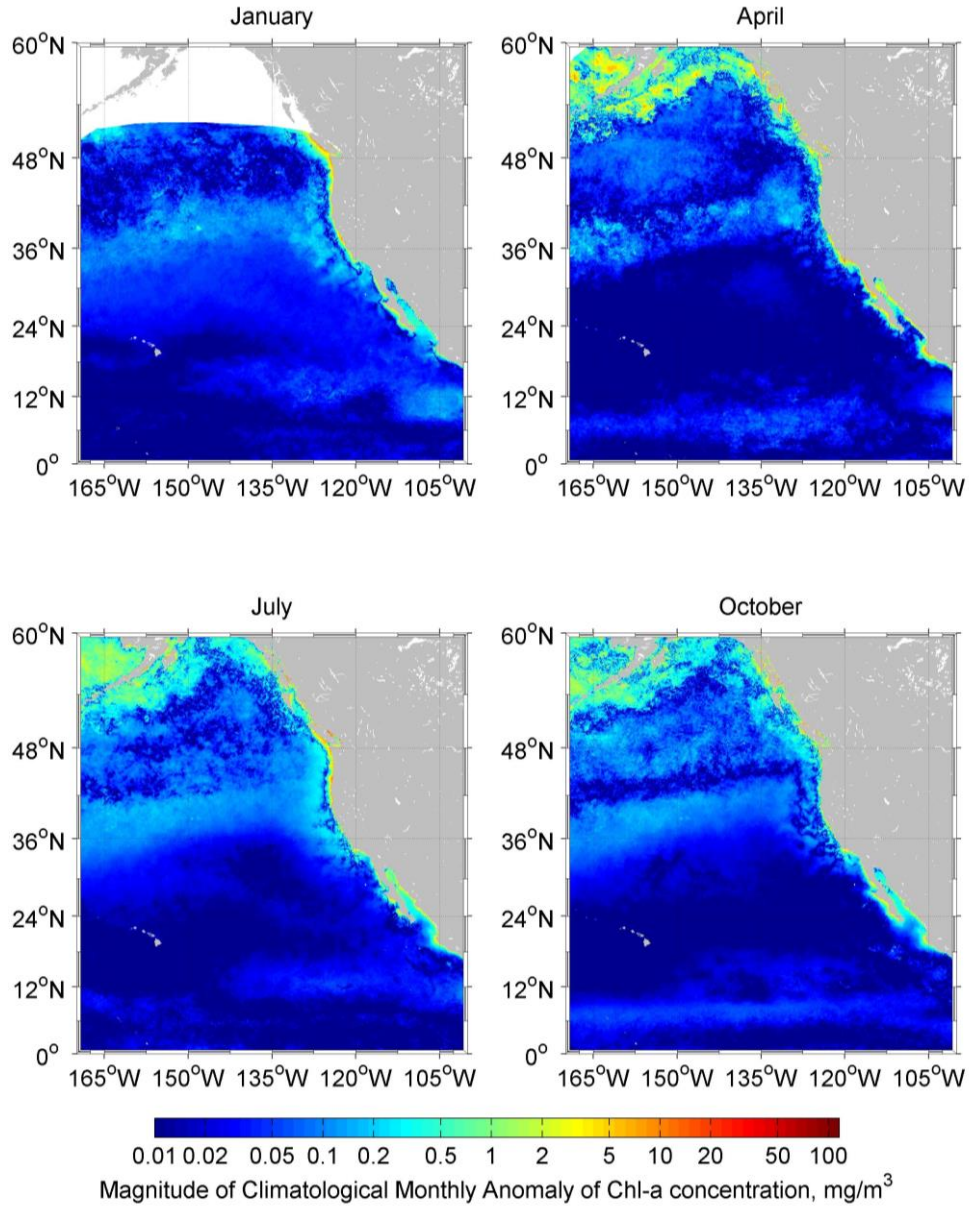
In the tropical North Pacific, the Chl-a is relatively low throughout the year due to tropical waters being low in nutrients. In January, (Figure 21 top left panel) there is a band of 0.2 mg/m<sup>3</sup> isoline expanding to the west from 105°W–111°W and centered at 12°N. As spring approaches as represented in April, the band of higher Chl-a water is moved westward to 135°W, Figure 21 top right panel. In the summer, as indicated by July (Figure 21 bottom left panel) the patch of higher Chl-a concentration has dissipated completely and the region now contains the majority concentration of 0.15 mg/m<sup>3</sup>. As the season progresses toward fall, depicted in October (Figure 21 bottom right) a band of lower concentration water, 0.15 mg/m<sup>3</sup> has developed from the coast of Mexico at 12°N and is expanding west toward 141°W. This band of 0.15 mg/m<sup>3</sup> surface water started in August (for image see Appendix B) and continued to move to the west for a few months until December where the structure of the band is visible. Another interesting feature in October is an area of 0.2 mg/m<sup>3</sup> isoline developed at 105°W and 12°N. This is the start of the band that was identified in January at the same location. Throughout the winter season the 0.2 mg/m<sup>3</sup> isoline band increases in area and continues to migrate to the west.

#### **H. CLIMATOLOGICAL MONTHLY ANOMALY FOR CHLOROPHYLL-A CONCENTRATION ( $C$ )**

The Climatological Monthly Anomaly (  $C$  ) was calculated using Equation (7) with the exception of Chl-a in place of acceleration potential. Climatological Monthly Anomaly (  $C$  ) is the departure of the Climatological Monthly Mean (  $\bar{C}$  ) from the Total Time Mean (  $\bar{\bar{C}}$  ). The graphs in Figure 22 are the magnitudes of the departures from the Total Time Mean (  $\bar{\bar{C}}$  ) based on Chl-a fluctuations from month to month from (2002–2014). To highlight the major departures from the Total Time Mean (  $\bar{\bar{C}}$  ) the Climatological Monthly Anomaly (  $C$  ) values for January, April, July, and October are shown in Figure 22, all 12 months can be found in Appendix C. The color bar indicates Chl-a concentration in mg/m<sup>3</sup>

with warm colors signifying higher concentration departure and cool colors signifying lower concentration departure.

Figure 22. Climatological Monthly Anomaly for Chl-a Concentration (  $C$  ) (2002–2014).



Climatological Monthly Anomaly of Chl-a concentration (  $C$  ) is shown for January (top left), April (top right), July (bottom left), and October (bottom right) calculated from 2002–2014 that total one image for each month. See Appendix C for all 12 months.

In Figure 22, there are four points of interest, the band of high Chl-a seasonal variability located at 36°N, the variability in the southern tropical Pacific, variability found along the Alaska coast and Aleutian Islands, and the variability within the CC. The maximum values of Chl-a concentration seasonal variability are found along the coast from the Aleutian Islands south to Baja California, Mexico in addition to the strongest gradient or largest change in concentration within a few kilometers from the coast line. This was anticipated as a result of strong seasonal fluctuations in upwelling or downwelling and biological productivity in proximity to the coastline. The greater the variability or departure from the Total Time Mean ( $\overline{\overline{C}}$ ), the warmer the colors, thus the coastline has the highest variability of Chl-a and contains the warmer (red and yellow) colors. This is consistent with the Climatological Monthly Mean ( $\overline{C}$ ) analysis where the Chl-a concentration had a range of 22.5 mg/m<sup>3</sup> depending on the season. The lowest variability of Chl-a concentration is found in the central Pacific, in the vicinity of the North Pacific Gyre where the value never rises above 0.1 mg/m<sup>3</sup>. This is consistent with the Climatological Monthly Mean ( $\overline{C}$ ) analysis where the range of Chl-a fluctuation was less than 0.05 mg/m<sup>3</sup> for all 12 months.

The region of variability located along 36°N is an interesting feature that appears throughout all 12 months. It is geographically in the vicinity of the North Pacific Current that moves from the western Pacific across eastward and interacts with the coast of North America. The stripe of variability maintains the same approximate location and variability of approximately 0.2 mg/m<sup>3</sup> for the majority of the 12 fields. In January, (Figure 22 top left panel) the stripe is slightly south of 36°N arches north and recurves south as it flows into the CC. As the season progresses from winter toward spring, (April, Figure 22 top right panel) the strip becomes less solid and is patchier, but maintains the same approximate location. In July, (Figure 22 bottom left panel) the stripe has migrated slightly north and is located at 36°N–42°N, however the patchiness has smoothed out to a consistent strip across the North Pacific region. From summer to fall, (October, Figure 22 bottom right panel) the consistency of the stripe has decreased and become less noticeable as the area approached the West Coast of North America and even less noticeable as the season continues through the winter (see Appendix C for images)

through January when the stripe is very prominent again. The stripe can be attributed to the seasonal migration of the North Pacific Gyre as described in the Climatological Monthly Mean, Section G of Chapter IV. The North Pacific Gyre strength and location changes and increases through the spring and summer as a result of the predominating wind shifting to the northwest and consequently enhance the North Pacific Gyre strength and area of impact. When and how this fluctuation occurs within a year is variable, but still consistent to maintain low variability values. Meaning the variability in the predominating wind patterns' strength and intensity directly impacts the strength and location of the North Pacific Gyre, which is highlighted in the Climatological Monthly Anomaly fields, Figure 22.

The migration of the North Pacific Gyre can also be observed in the fluctuation of another stripe that is located at the southern boundary. The southern stripe has a higher variability but not as high as seen at 36°N. The secondary strip is located at 12°N and extends across the tropical Pacific basin. The stripe is approximately 0.1 mg/m<sup>3</sup> on average for all fields, however in January (Figure 22 top left panel) the stripe is not as noticeable as the same patch of higher Chl-a concentration variability feature that was identified in the Climatological Monthly Mean ( $\bar{C}$ ) at 12°N, 105°W. As the season progresses from winter (January) to spring, the patch has moved to the east and elongated across the basin, however there is still some resemblance of the patch at the same location (12°N, 105°W) but at a value less than 0.1 mg/m<sup>3</sup> observed in January. In summer, July, (Figure 22 bottom left panel) the patch has dissipated and the elongated pattern is extending at 6°N from 105°W–41°W. In October, the stripe now extends completely across the Pacific basin and in addition migrated slightly south to 6°N. The slight southern migration of the tropical waters is in correlation of when the North Pacific Gyre is covering the largest area and has significant downwelling and reduced Chl-a concentration.

The Alaska Gyre experiences the most variability during the transition from winter, January, (Figure 22 top left panel) to spring, April, (Figure 22 top right panel) with a maximum value of 3 mg/m<sup>3</sup> along the Aleutian Islands. This mirrors the pattern observed in the Climatological Monthly Mean ( $\bar{C}$ ), and as the season transitions to



summer, July, (Figure 22 bottom left panel) the variability decreases significantly with a maximum value of  $0.75 \text{ mg/m}^3$  along the Aleutian Islands. From July to October (Figure 22 bottom right panel) the variability is similar to the summer. After October, the variability cannot be determined north of  $54^\circ\text{N}$  as a result of missing data in the region.

The highest departure from the Total Time Mean ( $\overline{\overline{C}}$ ) is observed in the CC region. There is a difference between Climatological Monthly Mean ( $\overline{C}$ ) and the Climatological Monthly Anomaly ( $C$ ), the variability remains very close to the coast and there is little variability off shore. In January (Figure 22 top left panel) the most variability is observed consistently along the coastline of Washington, California, and Baja California, Mexico. The maximum values of  $7 \text{ mg/m}^3$  are seen near the San Francisco Bay and Monterey Bay regions located at  $37\text{--}38^\circ\text{N}$ ,  $122^\circ\text{W}$ , and  $7 \text{ mg/m}^3$  near Washington. The fact that there is not much variability but directly near the coastline, confirms the discussion of the CC being highly variable seasonally. As the seasons progress from winter to spring, April, (Figure 22 top right panel) the variability along the coastline decreases significantly and only a small region, in very close proximity to the coastline identifies variability. The exceptions are Point Conception located at  $34^\circ\text{N}$ ,  $120^\circ\text{W}$  and along Baja California, Mexico where the maximum variability is  $7 \text{ mg/m}^3$ . The high variability near Point Conception indicates there are different mechanisms occurring in this region as compared to the overall average. Since Point Conception is an upwelling center, it makes sense that variability would be observed in this region as in the transition from spring into summer where upwelling is typically observed. In summer, July, (Figure 22 bottom left panel) most to the variability is observed north of Cape Mendocino located at  $42^\circ\text{N}$ ,  $127^\circ\text{W}$  at value of  $15 \text{ mg/m}^3$ . The changes occurring south of the Cape are consistent with the Total Time Mean ( $\overline{\overline{C}}$ ) and the fluctuations in the region north of the Cape experiences higher variability than the other regions during the summer seasons. As the season progresses through summer and into fall (October, Figure 22 bottom right panel) the variability continues to decrease with the major hotspots of variability maintaining at Point Conception and in proximity to San Francisco Bay and Monterey Bay throughout all months (see Appendix C).

## I. EOF ANALYSIS FOR CHLOROPHYLL-A CONCENTRATION SYNOPTIC MONTHLY ANOMALY ( $\hat{C}$ )

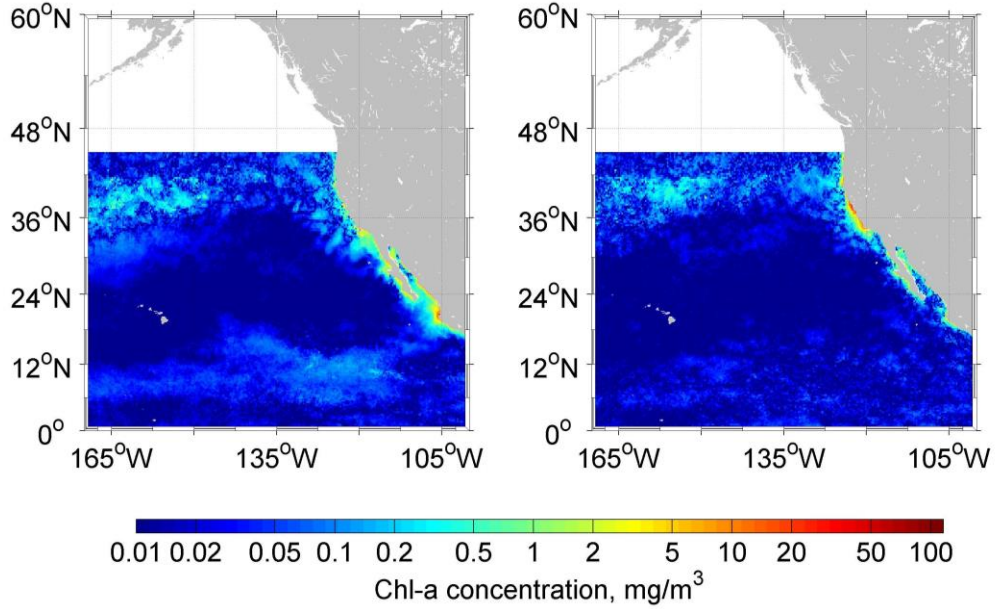
An EOF analysis was conducted on the Synoptic Monthly Anomaly ( $\hat{C}$ ) for Chl-a concentration from Equation (9) to analyze inter-annual variability of the surface Chl-a concentration. The EOF Modes represent the spatial component of the surface Chl-a concentration Synoptic Monthly Anomaly ( $\hat{C}$ ), which capture maximum variance. The variance contained in the first six EOFs is shown in Table 7. In the current research, the analysis effort was concentrated on Mode 1 and Mode 2. The subsequent Modes were not relevant in adding significance to the analysis of identifying patterns in the data. Mode 1 contained 15% of variance, and Mode 2 contained 8% of variance. This indicates that Mode 1 and Mode 2 combined contain a cumulative variance of 23%. This variance is not nearly as high as the Mode 1 and Mode 2 for acceleration potential (combined variance was 57%) suggesting that not all variability is being captured or identified within the first two Modes. In addition, all six Chl-a EOF Modes cumulatively do not add up to the cumulative variance found in acceleration potential. For this reason, Mode 1 was only analyzed for statistical significance and correlation to climatological indices, EMI and MEI.

Table 7. Variances of the First Six Leading EOFs of Synoptic Monthly Anomaly ( $\hat{C}$ ).

EOF $\hat{C}$	Variance	Cumulative Variance
1	0.15	0.15
2	0.08	0.23
3	0.07	0.30
4	0.06	0.36
5	0.06	0.42
6	0.05	0.47

Figure 23 represents EOF Mode 1 (left panel) and Mode 2 (right panel). The color bar indicates Chl-a concentration in  $\text{mg/m}^3$  with warm colors signifying higher concentration and cool colors signifying lower concentration.

Figure 23. EOF Analysis of Mode 1 and Mode 2 from Chl-a Concentration  
Synoptic Monthly Anomaly ( $\hat{C}$ ).



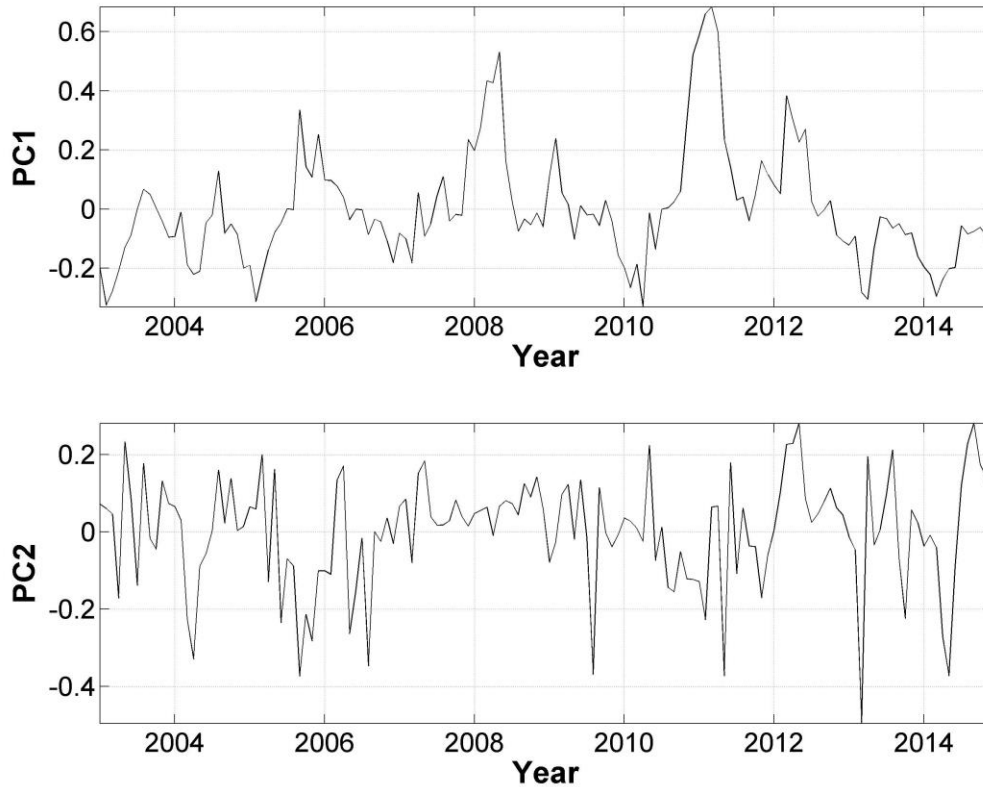
First two EOF Modes of Synoptic Monthly Anomaly of the Chl-a concentration. EOF Mode 1 (left panel) identifies 15% of the total non-seasonal variability and EOF Mode 2 (right panel) identifies an additional 8% of the total non-seasonal variability obtained from Synoptic Monthly Anomaly ( $\hat{C}$ ).

In Mode 1 and Mode 2, Figure 23, the same patterns can be identified as observed in Climatological Monthly Mean ( $\bar{C}$ ) and Climatological Monthly Anomaly ( $C$ ). With the exception of the Alaska Gyre, being excluded from the analysis due to lack of data, all of the same features can be identified, the anticyclonic North Pacific Gyre (located between 36°N–12°N, 105°W–165°W, CC (located along the west coast of North America) and the cyclonic circulation in the tropical northern Pacific (located south of 12°N). Both Modes display patchiness as a result of high spatial variability at the mesoscale level. In addition, the amplitudes of the Chl-a concentration are comparable to the Climatological Monthly Mean ( $\bar{C}$ ) and Climatological Monthly Anomaly ( $C$ ) with a few differences. The North Pacific Gyre is characterized by lower Chl-a concentrations due to the anticyclonic rotation of the gyre resulting in downwelling and decreased biological production resulting in a maximum Chl-a concentration of 0.02 mg/m<sup>3</sup>. The amplitudes observed in the CC are similar to previously analyzed monthly fields. Of

particular note, are the amplitudes observed in Mode 1 as compared to Mode 2. Mode 2 has a higher concentration near Cape Mendocino (42°N, 127°W), San Francisco Bay, and Monterey Bay (37–38°N, 122°W), and Point Conception (34°N and 120°W) than Mode 1. These areas were identified as upwelling centers along the CC and have a maximum value of approximately 38 mg/m<sup>3</sup>. In Mode 1 the region off the coast of Mexico located at 21°N, 105°W has significantly higher concentration than in Mode 2 with a value of 13 mg/m<sup>3</sup>.

The EOF PC represents the temporal component of the Chl-a concentration Synoptic Monthly Anomaly ( $C$ ). Figure 24 is the EOF PCs computed for the Chl-a concentration Synoptic Monthly Anomaly ( $\bar{C}$ ). For both graphs the x axis represents the respective PC and the y axis represents the time in years. PC1 has a maximum value of 0.68 and a minimum value of -0.33, see Figure 24. When PC1 is positive, it indicates enhanced Chl-a concentration during the respective year and when PC1 is negative it indicates a declined Chl-a concentration. The higher the positive value the larger the deviation from the Total Time Mean ( $\bar{\bar{C}}$ ). PC2 was not analyzed due to the low correlation value found from the EOF Mode analysis.

Figure 24. Principal Components of Synoptic Monthly Anomaly for Chl-a Concentration ( $\tilde{C}$ ).



This image shows a time series of the Chl-a concentration PCs of the Climatological Monthly Anomaly ( $\tilde{C}$ ). The y axis shows the coefficient and the x axis shows the respective year. Large peaks indicate significant correlation with the year.

#### J. CORRELATIONS BETWEEN PRINCIPAL COMPONENT 1 AND CLIMATOLOGICAL INDICES

There is a connection between the inter-annual variability of the surface Chl-a concentration in the CCS and climate variability. The connection has been estimated by the Pearson Correlation coefficient between the climate indices EMI and MEI and the Chl-a PC1.

PC1 had strong negative correlation with both EMI and MEI. Between PC1 and EMI the correlation coefficient of -0.79, with a two month lag, and with MEI the correlation coefficient was -0.69, with a two month lag. Such strong and statistically

significant negative correlation reflects the CC response to the tropical Pacific El Nino conditions. The main signature of this response is weak coastal upwelling that results in low primary productivity and reduced surface Chl-a concentration (for example see Jacox et al. 2015).

The weakening of the coastal upwelling is a combination of two processes: the thermocline depth change due to the tropical signal transferred with the coastally trapped Kelvin waves, and variations in large scale wind forcing. Thermocline depth can affect the upwelling strength in both the coastal regions and open ocean. Shifts in location of atmospheric pressure centers weaken or reverse upwelling favorable winds and reduce offshore Ekman transport or induce the onshore transport. The CC can weaken as a result of large scale changes in wind direction, wind strength, and a change in the ocean pressure gradient due to warming in the eastern tropical Pacific and consequently, affecting how the Chl-a is produced within the North Pacific Gyre and distributed from the areas of higher biological productivity. To separate effects of all these forcing mechanisms, additional datasets will need to be used to extend the time coverage for the Chl-a dataset.

This suggests that during a positive EMI/MEI, when El Nino Modoki or El Nino signatures are present, PC1 will have a negative value. The environmental forcing with a positive EMI corresponds to tropical central Pacific warming (El Nino Modoki indication) that causes lower pressure gradient. A lower pressure gradient causes a weaker North Pacific Gyre (negative PC1). A weaker North Pacific Gyre causes slowing of geostrophic flow and in turn a lower Chl-a concentration in the CC. The environmental forcing with a negative EMI corresponds to tropical central Pacific not warming (no indication of El Nino Modoki conditions) that causes higher pressure gradient of geostrophic flow. A higher pressure gradient causes a stronger North Pacific Gyre (positive PC1). A stronger North Pacific Gyre causes increased geostrophic flow and elevated Chl-a concentration in the CC. PC1 and MEI the environmental forcing with a positive MEI corresponds to tropical eastern Pacific warming (El Nino indication). The warming of tropical eastern Pacific causes lower pressure gradient. A lower pressure gradient causes a weaker North Pacific Gyre (negative PC1). A weaker North Pacific

Gyre causes slowing of geostrophic flow causing a lower Chl-a concentration in the CC. The environmental forcing with a negative MEI corresponds to tropical eastern Pacific with cooler waters (no indication of El Nino conditions). The cooler tropical eastern Pacific causes higher pressure gradient of geostrophic flow. A higher pressure gradient causes a stronger North Pacific Gyre (positive PC1). A stronger North Pacific Gyre causes increased geostrophic flow causing elevated Chl-a concentration in the CC.

THIS PAGE INTENTIONALLY LEFT BLANK



## V. CONCLUSION

This research identified inter-annual variability within the CCS, an eastern branch of the North Pacific Gyre, moving southward along the West Coast of North America and Baja California, Mexico (Hickey 1979). The CCS is known to be effected by El Nino, a climatological inter-annual mode of variability in the Pacific Ocean. While the effect of the traditional El Nino on the CCS is relatively well described, specific impacts of recently defined El Nino Modoki (Ashok et al. 2007) have not been studied in detail. To analyze the CCS inter-annual variability and to relate it to climatological inter-annual modes of variability, two long term datasets of in situ (SMG-WOD) and remotely sensed (MODIS-A) data were used, as well as two climatological indices, MEI and EMI.

The SMG-WOD was developed at the Naval Postgraduate School from the WOD and is the largest collection of oceanographic data (Boyer et al. 2013). OSD was applied to the WOD data to produce 3D synoptic monthly gridded temperature and salinity fields. The SMG-WOD is an ideal dataset to analyze long-term spatial and temporal variability of the CCS with a  $1^\circ \times 1^\circ$  horizontal resolution and 28 vertical layers (Chu et al. 2003a,b; 2004; 2005). This research focused on using the SMG-WOD in the north eastern Pacific and the CCS [ $0^\circ$ – $54^\circ$ N,  $165^\circ$ W– $105^\circ$ W] from January 1945 to December 2014. To compensate for the limited horizontal resolution of SMG-WOD near the coast, MODIS-A monthly composite fields for surface Chl-a concentration was also analyzed. The MODIS-A dataset has a 4.6 km resolution and contains surface Chl-a concentration in  $\text{mg}/\text{m}^3$  from July 2002 to December 2014. The climatological indices, MEI and EMI were used to compare data to well-known and identifiable inter-annual variations that have an impact on the CCS. MEI is calculated from six observed variables and identifies ENSO oscillation patterns (Jacox et al. 2015; Ashok et al. 2007). EMI is calculated from sea surface temperature anomalies in three regions of the tropical Pacific: east, west, and central, which characterizes El Nino Modoki oscillation patterns (Ashok et al. 2007).

Acceleration potential ( $\psi$ ) at the isopycnal surface of ( $\sigma_\theta$ )  $26.9 \text{ kg}/\text{m}^3$  relative to the 1000 dbar was calculated for the SMG-WOD temperature and salinity data to represent geostrophic circulation below surface. Next, a composite analysis was

conducted for the acceleration potential ( $\psi$ ) and Chl-a concentration ( $C$ ). The calculated fields included Climatological Monthly Mean ( $\bar{\psi}$ ), Total Time Mean ( $\bar{\bar{\psi}}$ ), Climatological Monthly Anomaly ( $\tilde{\psi}$ ), and Synoptic Monthly Anomaly ( $\hat{\psi}$ ). Synoptic Monthly Anomaly ( $\hat{\psi}$ ) represents inter-annual variability and was the main focus of this research. EOF analysis was conducted on Synoptic Monthly Anomaly acceleration potential ( $\hat{\psi}$ ) and Chl-a ( $\hat{C}$ ) to identify patterns of the maximum variance within the CCS. Finally, correlation coefficients were calculated to determine correlations between the inter-annual variability and EMI/MEI.

Results for acceleration potential and Chl-a composite analysis identified three major features from the Total Time Mean, the cyclonic Alaska Gyre, the anticyclonic North Pacific Gyre, and the northern portion of the cyclonic circulation in the northern tropical Pacific, see Figures 14 and 20. These circulation patterns are well known and agree with previous studies of large scale circulation, see Castro et al. (2001). Climatological Monthly Anomaly ( $\tilde{\psi}$  and  $C$ ) values was calculated showing different results for the acceleration potential and surface chlorophyll concentration in long term seasonal variability. Acceleration potential Climatological Monthly Anomaly ( $\tilde{\psi}$ ) demonstrated weak seasonal variability despite the highly variable seasonal fluctuations of the CCS, Figure 15. A contributing factor to this result may be attributed to the low horizontal resolution along the coast and the inability to identify coastal fluctuations of upwelling, downwelling, and flow reversal of the CU and DC. On the other hand, the Chl-a concentration Climatological Monthly Anomaly ( $C$ ) indicated large seasonal variability in the CCS and small seasonal variability in the North Pacific Gyre and in the northern tropical Pacific, Figure 22. The large seasonal variability was also identified in Climatological Monthly Mean ( $\bar{C}$ ), see Figure 21.

EOF analysis was conducted on the Synoptic Monthly Anomaly fields for acceleration potential ( $\hat{\psi}$ ) and Chl-a concentration ( $\hat{C}$ ). EOF Modes represent spatial patterns and capture maximum variance within the north eastern Pacific region. EOF Mode 1 for acceleration potential contained 35% variance and Mode 2 contained 22%

variance for a combined variance of 57% suggesting that over half of the inter-annual variability in the CCS is represented in the first two Modes. Mode 1 contours represent strengthening of the geostrophic flow of the North Pacific Gyre and consequently increasing the CC velocity for a positive PC1 (Figure 16 left panel). In the negative phase, Mode 1 pattern will weaken the acceleration potential gradients and decrease the geostrophic velocity in the CC. The positive phase of EOF Mode 2 for acceleration potential represents an offshore flow and consequently coastal upwelling within the CC (Figure 16 right panel). A negative phase represents a general pattern of the onshore flow with reduced upwelling or downwelling in the coastal region of the CC. PCs represents the temporal component of the maximum variance for the north eastern Pacific region, see Figure 17. A positive PC1 signifies an anticyclonic gyre that strengthens the North Pacific Gyre and consequently enhances the CC, meaning the geostrophic flow anomaly is stronger. When PC1 is negative, it signifies a cyclonic gyre that weakens the anticyclonic geostrophic flow of the North Pacific Gyre and consequently reduces the geostrophic flow of the CC. A positive PC2 signifies an offshore geostrophic flow that enhances coastal upwelling. When PC2 is negative, it signifies an onshore geostrophic flow that suppresses coastal upwelling or enhances coastal downwelling, and potentially the DC as a surface expression of the CU may be present.

There is a connection between the acceleration potential inter-annual variability (PC1 and PC2) and the climate indices EMI and MEI. For PC1, at the 0.05 significance level, a correlation coefficient of -0.15 was calculated between PC1 and EMI. The statistically significant (but not strong) negative correlation suggests that during El Nino Modoki (positive EMI), PC1 will be negative, resulting in slowing of the geostrophic flow in the CC. When PC1 is positive, EMI index will be negative, resulting in increased geostrophic flow in the CC. There was a correlation coefficient of -0.31 between PC2 and MEI at the .05 significance level that indicates negative correlation (statistically significant but not strong). This suggests that a positive MEI, (when El Nino conditions exist) PC2 will have a negative value resulting in onshore geostrophic flow leading to coastal downwelling or reduced upwelling in the CC. When PC2 is positive, MEI will be negative resulting in offshore flow leading to enhanced coastal upwelling in the CC.

EOF Mode 1 for the synoptic monthly anomaly of the Chl-a concentration contained 15% variance and Mode 2 contained 8% variance for a combined variance of 23% suggesting not all non-seasonal variability is being captured by the first two modes. For this reason, Mode 1 was only analyzed for correlation to climatological indices, EMI and MEI. In Figure 23, Mode 1 and Mode 2 identify the same circulation patterns as observed in Climatological Monthly Mean ( $\bar{C}$ ) and Climatological Monthly Anomaly ( $C$ ) and patchiness as a result of high spatial variability at mesoscale level. Mode 1 has higher Chl-a concentration variability off the coast of Baja California, Mexico. Mode 2 has a higher concentration near upwelling centers in the CC. A positive PC1, Figure 24, signifies enhanced Chl-a concentration during the respective year and when PC1 is negative it signifies a decline surface Chl-a concentration.

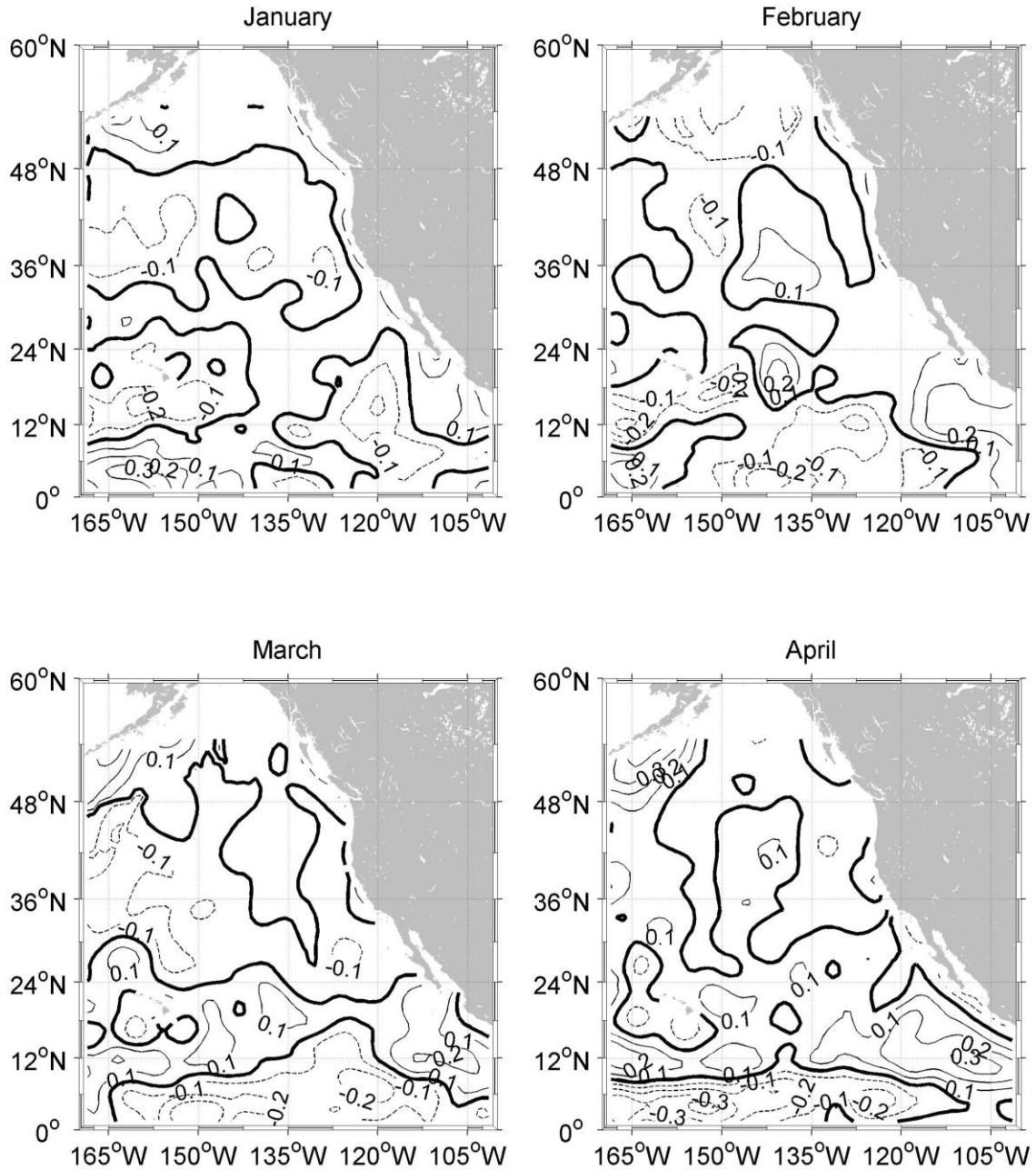
Connection between Chl-a concentration inter-annual variability (PC1) and the climate indices EMI and MEI has been estimated using correlation coefficients. For PC1 there was a strong negative correlation with both EMI and MEI. Between PC1 and EMI the correlation coefficient of -0.79, with a two month lag, and with MEI the correlation coefficient was -0.69, with a two month lag. This suggests that during a positive EMI/MEI, (when El Nino Modoki or El Nino events occur) PC1 will have a negative value resulting in slowing of the geostrophic flow causing a lower Chl-a concentration in the CC. When PC1 is positive, EMI/MEI will be negative resulting in increased geostrophic flow and enhanced Chl-a concentration in the CC.

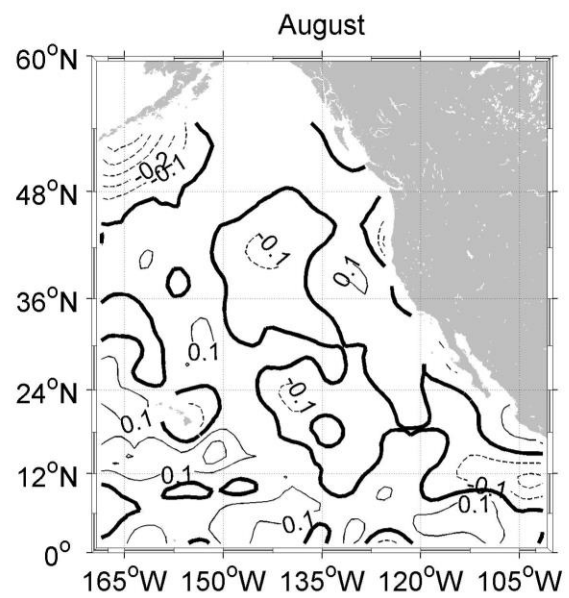
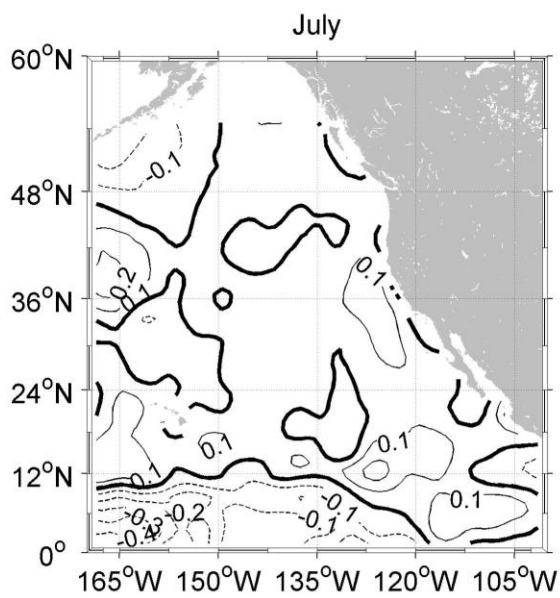
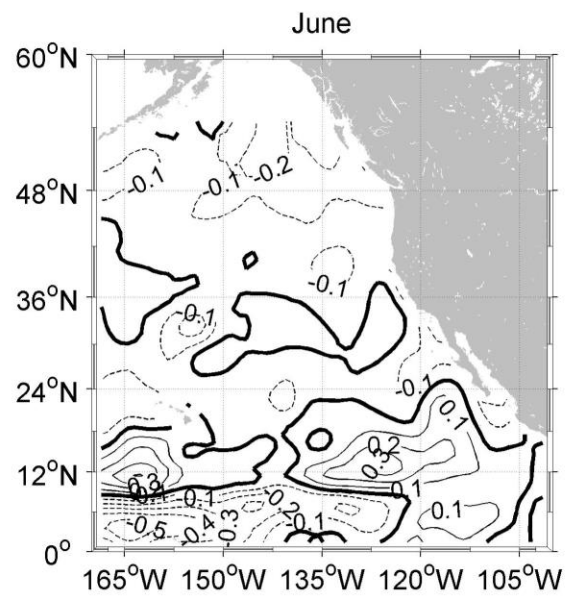
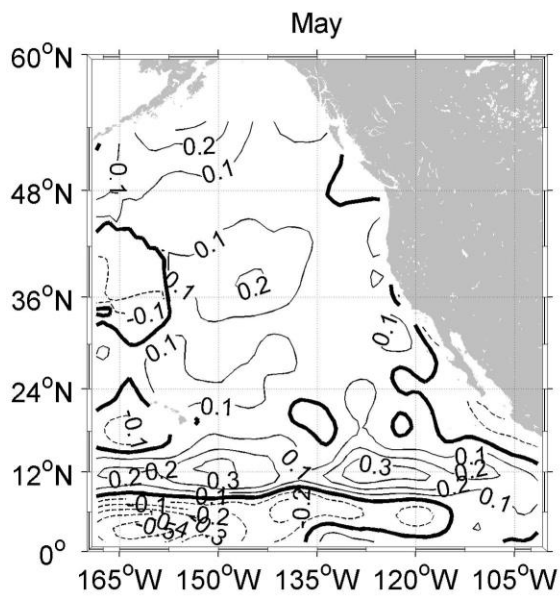
For prospective future research of the CCS there are three areas that can be further investigated. Acceleration potential at the isopycnal surface of ( $\sigma_\theta$ ) 26.9 kg/m<sup>3</sup> relative to the 1000 dbar was a good intermediate level reference point for the majority of the eastern North Pacific, however, during some seasons the isopycnal surface outcropped to the surface north of 54°N and this region was not included in the calculations. Since the scope of this research was on the CCS this limitation did not impact the analysis of the CCS. A deeper isopycnal surface can also be used to include the northernmost part of the Alaska Gyre into the analysis. A second opportunity for continued research, is analyzing the Climatological Monthly Anomaly for Chl-a ( $C$ ), Figure 22, band of high seasonal

variability located at 36°N. This particular feature is present in all monthly fields. It was hypothesized in the current research it is an effect of the monthly migration of the North Pacific Gyre. However, since the focus was on the CCS no other investigation was conducted in determining other potential causes. The third research possibility is to expand the dataset for the Chl-a concentration using other satellite sources, such as SeaWiFS. This is not a trivial problem because the data from the satellites must be manipulated in order to remove possible bias when merging the data products from two different systems. By tackling the compatibility issues it would expand the Chl-a dataset from 2002–2014 (MODIS-A) to 1997–present.

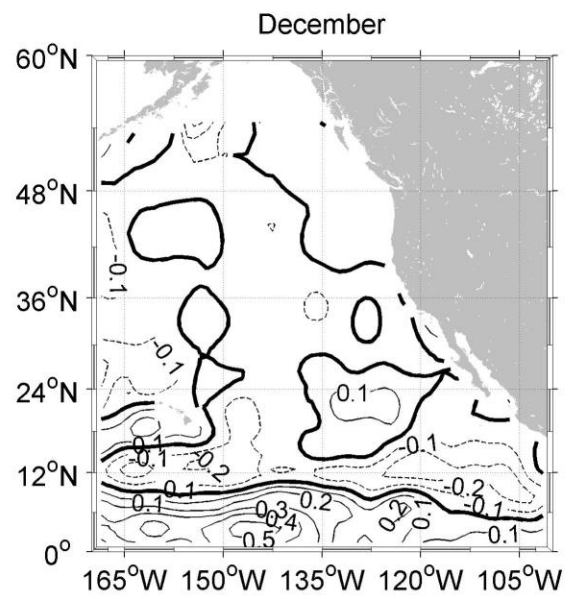
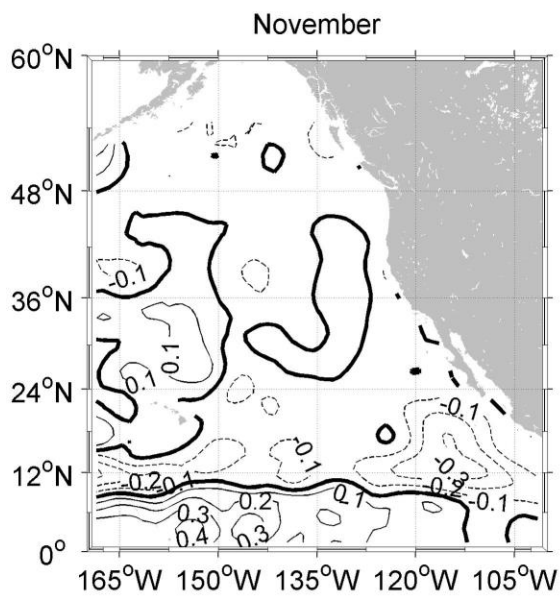
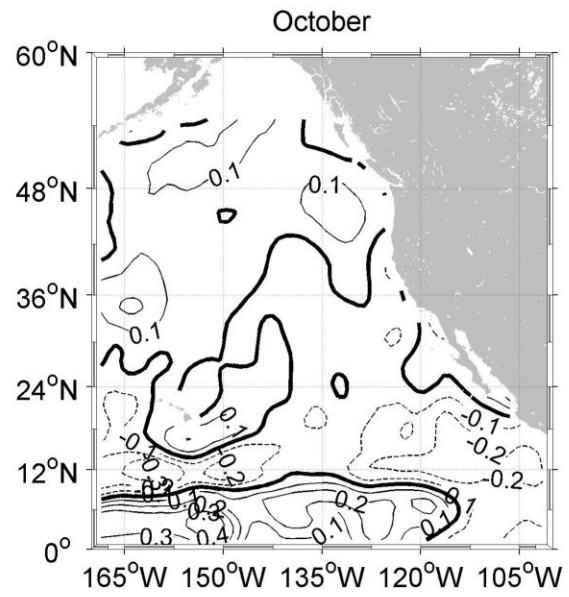
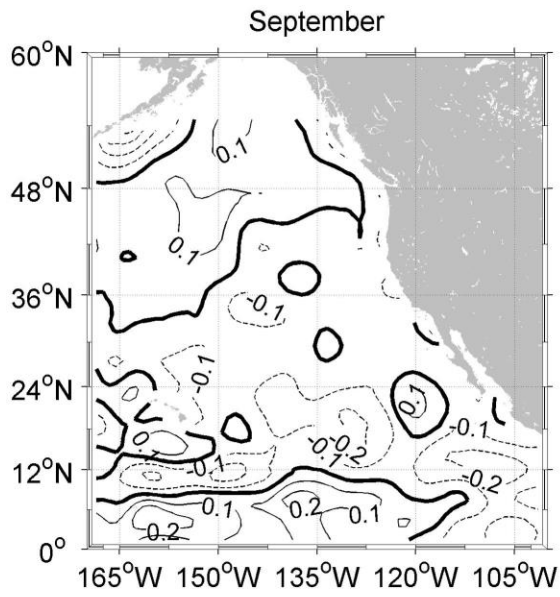
THIS PAGE INTENTIONALLY LEFT BLANK

**APPENDIX A. CLIMATOLOGICAL MONTHLY ANOMALY FOR  
ACCELERATION POTENTIAL ( $\tilde{\psi}$ ) MONTHS JANUARY–  
DECEMBER (1945–2014).**



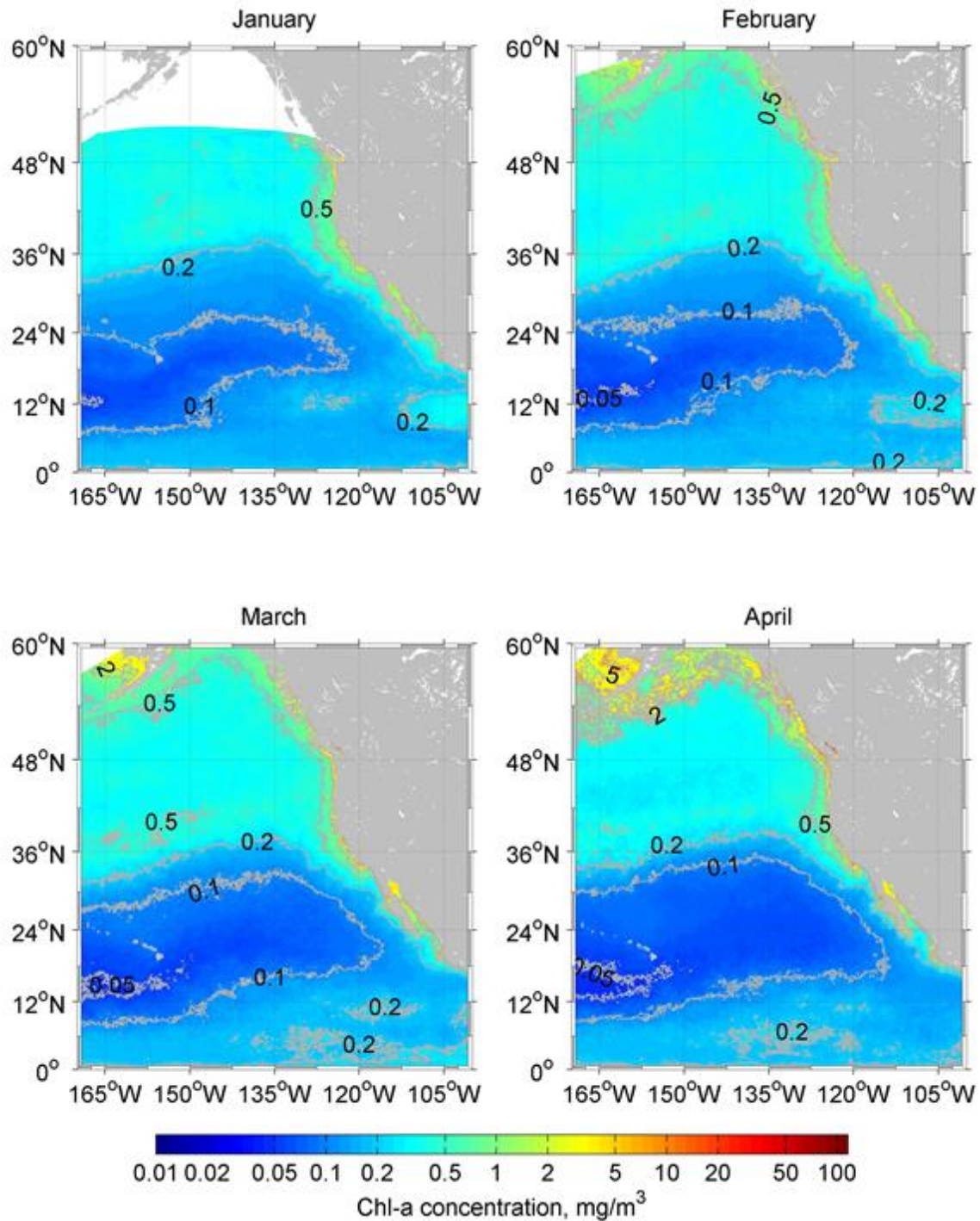


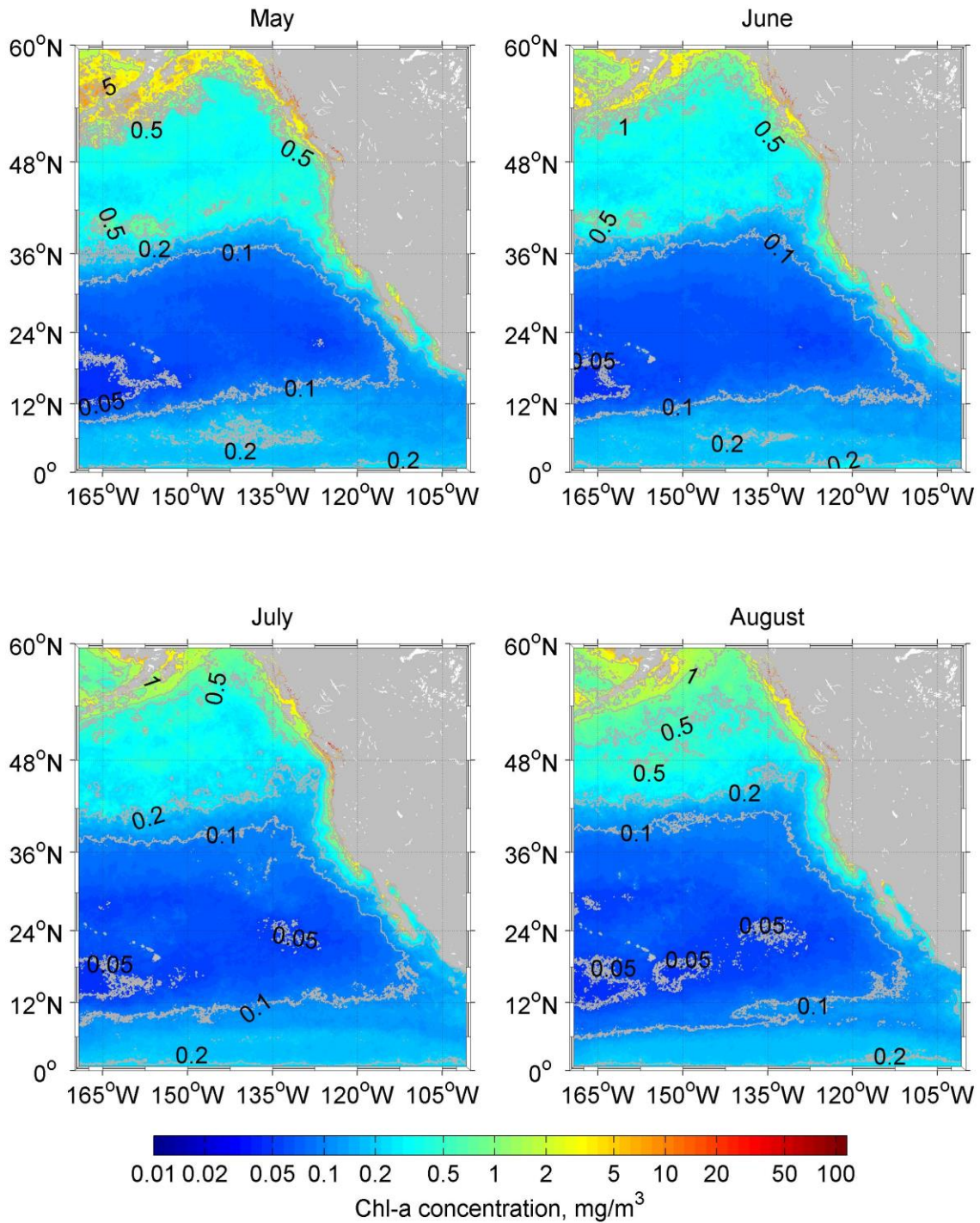




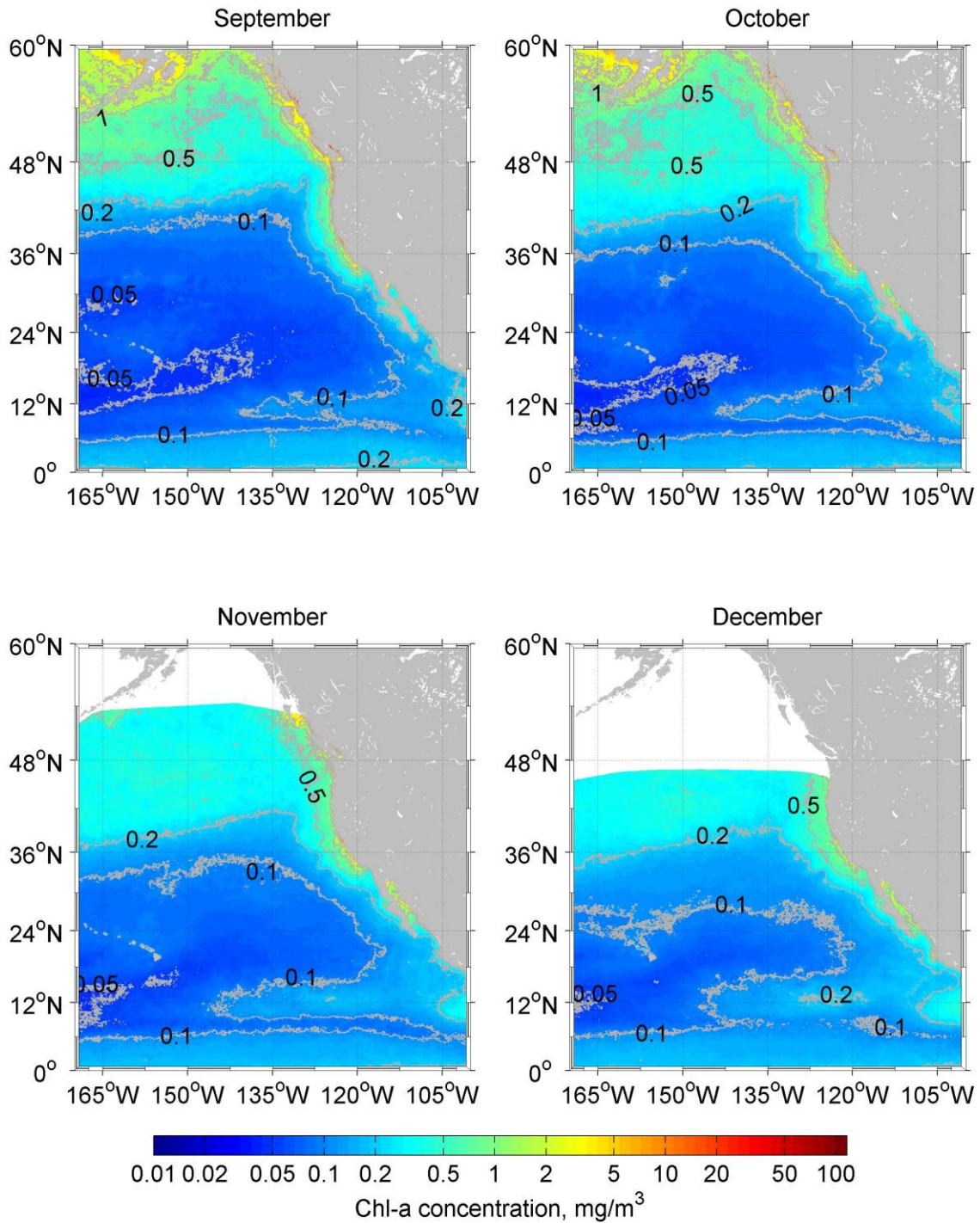
THIS PAGE INTENTIONALLY LEFT BLANK

**APPENDIX B. CLIMATOLOGICAL MONTHLY MEAN FOR  
CHLOROPHYLL-A CONCENTRATION ( $\bar{C}$ ) MONTHS JANUARY–  
DECEMBER (2002–2014).**



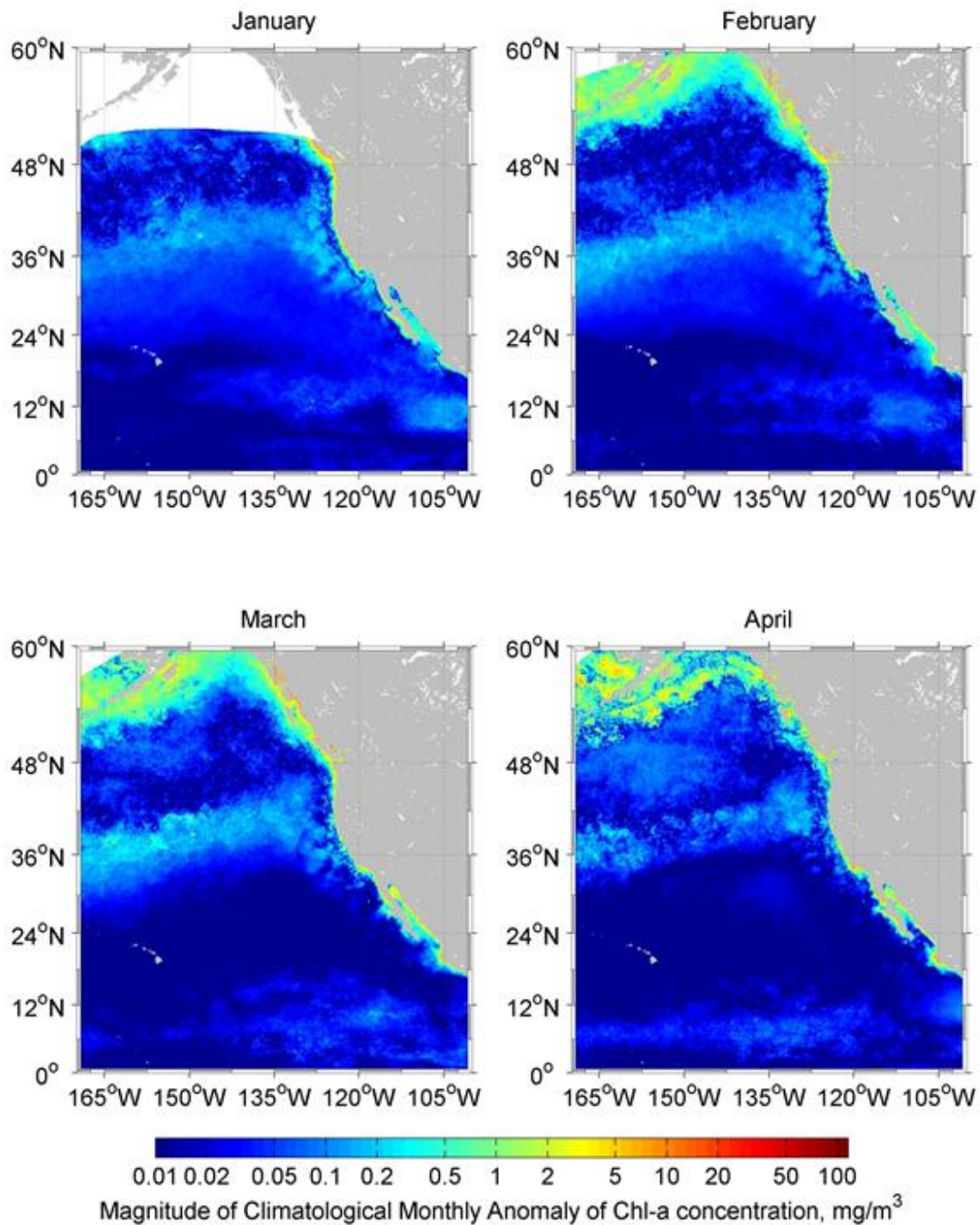


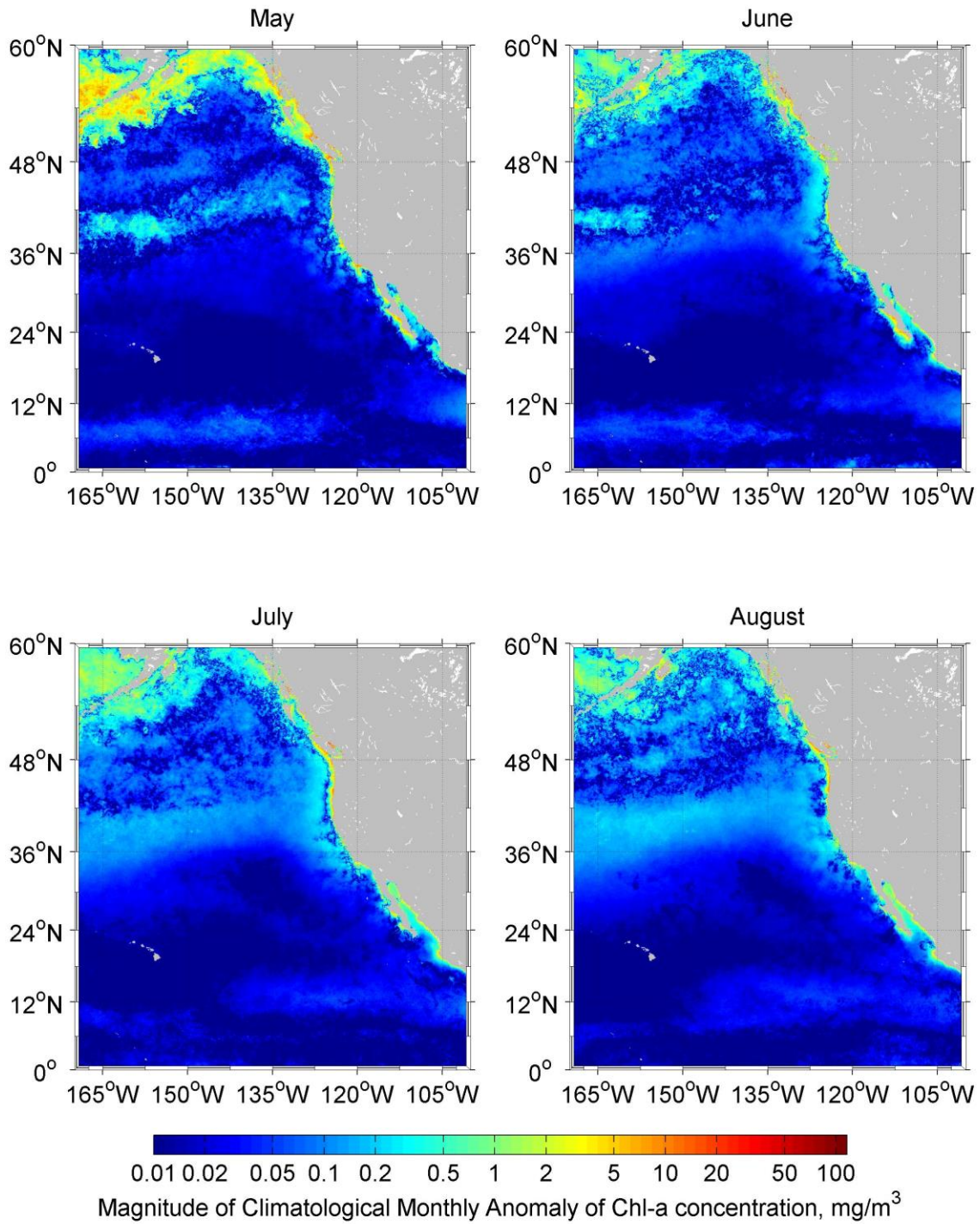




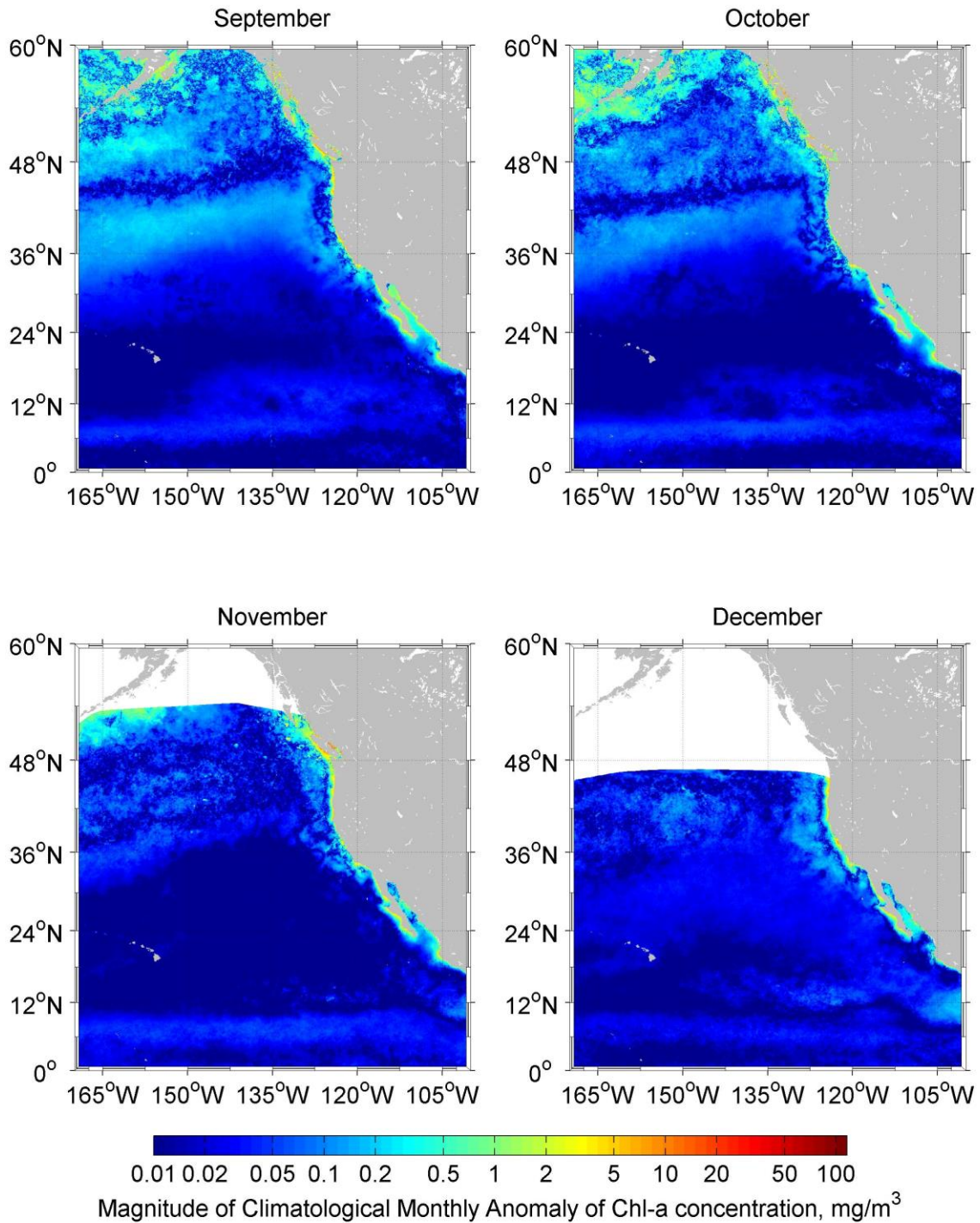
THIS PAGE INTENTIONALLY LEFT BLANK

# **APPENDIX C. CLIMATOLOGICAL MONTHLY ANOMALY FOR CHLOROPHYLL-A CONCENTRATION ( *C* ) MONTHS JANUARY– DECEMBER (2002-2014).**









THIS PAGE INTENTIONALLY LEFT BLANK

## LIST OF REFERENCES

- Ashok, K., S. K. Behera, S. A. Rao, H. Weng, and T. Yamagata, 2007: El Niño Modoki and its possible teleconnection, *Journal of Geophysical Research*, **112**, C11007, doi:10.1029/2006JC003798.
- Bennett, K. F., 2004: Seasons in the Sea-A month-to-month- guide to Central California sea life, Accessed 18 April 2016. [Available online at <http://www.seasonsintthesea.com/jan-feb/phys.shtml>.]
- Boyer, T. P., J. I. Antonov, O. K. Baranova, C. Coleman, H. E. Garcia, A. Grodsky, D. R. Johnson, R. A. Locarnini, A.V. Mishonov, T. D. O'Brien, C. R. Paver, J. R. Reagan, D. Seidov, I. V. Smolyar, and M. M. Zweng, 2013: *World Ocean Database 2013*. Sydney Levitus, Ed.; Alexey Mishonov, Technical Ed., NOAA Atlas NESDIS 72, 209 pp. [Available online at <http://doi.org/10.7289/V5NZ85MT>.]
- Bjerknes, J., 1969: Atmospheric teleconnections from the equatorial Pacific. *Monthly Weather Review*, **97**, 163–172.
- Castro, C. G., F. P. Chavez, and C.A. Collins, 2001: Role of the California Undercurrent in the export of denitrified waters from the eastern tropical North Pacific. *Global Biogeochemical Cycles*, **15**, 819–830.
- Chhak, K., and E. Di Lorenzo, 2007: Decadal variations in the California Current upwelling cells. *Geophysical Research Letters*, **314**, L14604, doi:10.1029/2007GL030203.
- Choi, H., 2015: East Sea Spatial and Temporal Variability of Thermohaline Structures and Circulation Identified from Observational (T, S) Profiles. M.S. thesis, Oceanography Department, Naval Postgraduate School, 161 pp. [Available online at <http://calhoun.nps.edu/handle/10945/47921>.]
- Chu, P. C., L. M. Ivanov, T. P. Korzhova, T. M. Margolina, and O. M. Melnichenko, 2003a: Analysis of sparse and noisy ocean current data using flow decomposition. Part 1: Theory. *Journal of Atmospheric and Oceanic Technology*, **20**, 478–491.
- Chu, P. C., L. M. Ivanov, T. P. Korzhova, T. M. Margolina, and O. M. Melnichenko, 2003b: Analysis of sparse and noisy ocean current data using flow decomposition. Part 2: Application to Eulerian and Lagrangian data. *Journal of Atmospheric and Oceanic Technology*, **20**, 492–512.
- Chu, P. C., L. M. Ivanov, and T. M. Margolina, 2004. Rotation method for reconstructing process and field from imperfect data. *International Journal of Bifurcation and Chaos*, **14**, 2991–2997.

- Chu, P. C., L. M. Ivanov, and T. M. Margolina, 2005a: Seasonal variability of the Black Sea chlorophyll-a concentration. *Journal Maritime Systems*, **56**, 243–261, doi:10.1016/j.jmarsys.2005.01.001.
- Chu, P. C., L. M. Ivanov, and O. V. Melnichenko, 2005b: Fall-winter current reversals on the Texas-Louisiana continental shelf. *Journal of Physical Oceanography*, **35**, 902–910, doi: 10.1175/JPO2703.1.
- Chu, P. C., L. M. Ivanov, O. V. Melnichenko, and N. C. Wells, 2007: On long baroclinic Rossby waves in the tropical North Atlantic observed from profiling floats. *Journal of Geophysical Research*, **112**, C05032, doi:10.1029/2006JC003698.
- Chu, P. C., 2011: Global upper ocean heat content and climate variability. *Ocean Dynamics*, **61**, 1189–1204, doi:10.1007/s10236-011-0411-x.
- Chu, P. C., Y. Chen, and S. Lu, 1998: Temporal and Spatial Variabilities of Japan Sea Surface Temperature and Atmospheric Forcings. *Journal of Oceanography*, **54**, 273–284.
- Chu, P. C., H. Tseng, C. P. Chang, and J. M. Chen, 2011: Global upper ocean heat content and climate variability. *Ocean Dynamics*, **61**, 1189–1204.
- Chu, P. C., H. Tseng, C. P. Chang, and J. M. Chen, 2007: South China Sea warm pool detected in spring from the Navy's Master Oceanographic Observational Data Set (MOODS). *Journal of Geophysical Research*, **102**, 15761–15771.
- Chu, P. C., R. T. Tokmakian, C. W. Fan, C. L. Sun, 2015: Optimal spectral decomposition (OSD) for ocean data assimilation. *Journal of Atmospheric and Oceanic Technology*, **32**, 828–841.
- Chu, P. C., C. W. Fan, 2016: Synoptic monthly gridded world ocean database (SMG-WOD). *Geoscience Data Journal*, submitted for publication.
- Chu, P. C., and C. W. Fan, 2016: Synoptic monthly gridded three dimensional (3D) World Ocean Database temperature and salinity from January 1945 to December 2014 (NCEI Accession 0140938). Version 1.1. NOAA National Centers for Environmental Information. Dataset. [Available online at <http://data.nodc.noaa.gov/cgi-bin/iso?id=gov.noaa.nodc:0140938>.]
- Davis, R. E., 1985: Drifter observations of coastal surface currents during CODE: the method and descriptive view. *Journal of Geophysical Research*, **90**, 4741–4755.
- Di Lorenzo, E., and Coauthors, 2008: North Pacific Gyre Oscillation links ocean climate and ecosystem change. *Geophysical Research Letters*, **35**, L08607, doi:10.1029/2007GL032838.

- Douglass, E., D. Roemmich, D. Stammer, 2006: Inter-annual variability in the northeast Pacific circulation. *Journal of Geophysical Research*, **111**, C04001, doi:10.1029/2005JC003015
- Djavidnia, S., F. Melin, and N. Hoepffner, 2010: Comparision of global Ocean color data records. *Ocean Science*, **6**, 61–76.
- Evans, J. D., 1996: *Straightforward Statistics for the Behavioral Sciences*, Brooks/Cole Publishing Company, 600 pp.
- Hannachi, A., 2004: A Primer for EOF Analysis of Climate Data: Department of Meteorology, University of Reading, 33 pp. [Available online at <http://www.met.rdg.ac.uk/~han/Monitor/eofprimer.pdf>.]
- Hickey, B., 1979: The California Current System- hypotheses and facts. *Progress in Oceanography* **8**, 191–279.
- Huntsberger, D. V., and P. Billingsley, 1973: Regression and Correlation. *Elements of Statistical Inference*, 3<sup>rd</sup> ed. Allyn and Bacon, Inc., 218–243.
- Hu, C., Z. Lee, and B. Franz, 2012: Chlorophyll a algorithms for oligotrophic oceans: A novel approach based on three-band reflectance difference. *Journal Geophysics Research*, **117**, C01011, doi:10.1029/2011JC007395.
- Jacox, M. G., S. J. Bogard, E. L. Hazen, and J. Fiechter, 2015: Sensitivity of the California Current nutrient supply to wind, heat, and remote ocean forcing. *Geophysical Research Letters*, **42**, 5950–5957, doi:10.1002/2015GL065147.
- Japan Agency for Marine-Earth Science and Technology (JAMSTEC), 2016: Modoki ENSO. Accessed 11 April 2016. [Available online at: [http://www.jamstec.go.jp/frcgc/research/d1/iod/enmodoki\\_home\\_s.html.en](http://www.jamstec.go.jp/frcgc/research/d1/iod/enmodoki_home_s.html.en).]
- Japan Agency for Marine-Earth Science and Technology (JAMSTEC Modoki dataset), cited 2016: Modoki ENSO Data Links. Accessed 11 April 2016. [Available online at <http://www.jamstec.go.jp/frcgc/research/d1/iod/DATA/emi.monthly.txt>.]
- Karaaslan, N., 2015: Eastern Mediterranean Sea Spatial and Temporal Variability of Thermohaline Structure and Circulation Identified from Observational (T, S) Profiles. M.S. thesis, Oceanography Department, Naval Postgraduate School, 145 pp. [Available online at <http://calhoun.nps.edu/handle/10945/47978>.]
- King, J. R., 2005: Report of the Study Group on Fisheries and Ecosystem Responses to Recent Regime Shifts, North Pacific Maritime science Organization Scientific Report, **28**, 162 pp.

- King, J. R., V. N. Agostini, C. J. Harvey, G. A. McFarlane, M. G. Foreman, J. E. Overland, E. Di Lorenzo, N. A. Bond, and K. Y. Aydin, 2011: Climate Forcing and the California Current ecosystem, *Journal of Marine Science*, **68**, 1199–1216.
- Lorenz, E. N., 1970: Climate change as a mathematical problem. *Journal of Applied Meteorology*, **9**, 325–329.
- Mantua, N. J., S. R. Hare, Y. Zhang, J. M. Wallace, and R. C. Francis, 1997: A Pacific Inter-decadal Climate Oscillation with Impacts on Salmon Production. *Joint Institute for the Study of the Atmosphere and Oceans*, **379**, 1069–1079.
- McDougall, T. J., 1989: Streamfunctions for the lateral velocity vector in a compressible ocean. *Journal of Marine Research*, **47**, 267–284.
- McGowan, R., D. R. Cayan, and L. M. Dorman, 1998: Climate-ocean variability and ecosystem response in the Northeast Pacific, *Science*, **281**, 210–217.
- Moderate Resolution Imaging Spectroradiometer Aqua Chlorophyll-a database (MODIS-A), 2016a: Physical Oceanography Distributed Active Archive Center / MODIS Aqua Level 3 Global Monthly Mapped 4 km Chlorophyll a v2014.0. Accessed 23 January 2016. [Available online at [http://podaac.jpl.nasa.gov/dataset/MODIS\\_Aqua\\_L3\\_CHLA\\_Monthly\\_4km\\_V2014.0\\_R](http://podaac.jpl.nasa.gov/dataset/MODIS_Aqua_L3_CHLA_Monthly_4km_V2014.0_R).]
- Montgomery, R. B., 1937. A suggested method for representing gradient flow in isentropic surfaces. *Bulletin of the American Meteorological Society*, **18**, 210–212.
- National Aeronautics and Space Administration EarthData (NASA), 2016: Ocean Color Data. Accessed 11 April 2016. [Available online at [http://oceandata.sci.gsfc.nasa.gov/MODIS-Aqua/Mapped/Monthly/4km/chlor\\_a](http://oceandata.sci.gsfc.nasa.gov/MODIS-Aqua/Mapped/Monthly/4km/chlor_a).]
- National Oceanic and Atmospheric Administration (NOAA), 2016: About our Agency. Accessed 11 April 2016. [Available online at <http://www.noaa.gov/about-our-agency>.]
- National Ocean and Atmospheric Administration / National Centers for Environmental Information (NOAA/NCEI), 2016: About. Accessed 11 April 2016. [Available online at <http://www.nodc.noaa.gov/about>.]
- National Oceanic and Atmospheric Administration (NOAA El Nino), 2016: NOAA gets U.S. Consensus for El Nino/La Nina Index Definitions. Accessed 11 April 2016. [Available online at <http://www.noaanews.noaa.gov/stories/s2095.htm>.]
- National Oceanic and Atmospheric Administration Earth Systems Research Laboratory (NOAA MEI), 2016: NOAA Multivariate ENSO Index (MEI). Accessed 11 April 2016. [Available online at <http://www.esrl.noaa.gov/psd/enso/mei/>.]



- National Oceanic and Atmospheric Administration (NOAA MEI dataset), 2016: Multivariate ENSO index dataset. Accessed 11 April 2016. [Available online at <http://www.esrl.noaa.gov/psd/enso/mei/table.html>.]
- National Oceanic and Atmospheric Administration and National Centers for Environmental Information (NOAA GSHHG), 2016: GSHHG - A Global Self-consistent, Hierarchical, High-resolution Geography Database. Accessed 23 January 2016. [Available online at <http://www.ngdc.noaa.gov/mgg/shorelines/gshhs.html>.]
- Ocean Biology Processing Group, 2015. MODIS Aqua Level 3 Global Monthly Mapped 4 km Chlorophyll a v2014.0. Ver. 2014.0. PO.DAAC, CA, USA. Dataset accessed [216-01-26].
- Pavlova, Y. V., 1966: Seasonal variations of the California Current, *Oceanology*, **6**, 806–814.
- Richman, M. B., 1986: Rotation of principal components. *Journal of Climatology*, **6**, 293–335.
- Reid, J. L. Jr., 1965: Physical oceanography of the region near Point Arguello. Technical report, Institute of Marine resources, University of California, IMR Reference 65–19
- Reid, J. L. Jr., and R. A. Schwartzlose, 1962: Direct Measurements of the Davidson Current off Central California. *Journal of Geophysical Research*, **67**, 2491–2497.
- Reid, J. L. Jr., G. I. Roden, and J. G. Wyllie, 1958: Studies of the California Current System. Scripps Institute of Oceanography, New Series 998, Progress from 1 July 1956 to 1 January 1958, 27–56. [Available online at [http://calcofi.org/publications/calcofireports/v06/Vol\\_06\\_Reid\\_etal.pdf](http://calcofi.org/publications/calcofireports/v06/Vol_06_Reid_etal.pdf).]
- Roughgarden, J., S. Gaines, and H. Possingham, 1988: Recruitment dynamics in the complex life cycles. *Science*, **241**, 1397–1560.
- Scripps Institute of Oceanography (SCRIPS): Satellite Geodesy, 2015: Global Topography. Accessed 23 January 2016. [Available online at [http://topex.ucsd.edu/marine\\_topo/](http://topex.ucsd.edu/marine_topo/).]
- Shanks, A. L., and G. L. Eckert, 2005: Population persistence of California Current Fishes and Benthic Crustaceans: A Marine Drift Paradox. *Ecological Monographs*, **74**, 505–524.
- Simmons, A. J., G. W. Branstator, and J. M. Wallace, 1983: Barotropic wave propagation, instability and atmospheric teleconnections patterns. *Journal of Atmospheric Science*, **40**, 1363–1392.

- Smith, J. D., B. Hickey, and J. Beck, 1976: Observations from moored current meters on the Washington continental shelf from February 1971–February 1974. University of Washington Special Report #65, 383 pp.
- Smith, R. D., and P. R. Gent, 2002: Reference manual for the Parallel Ocean Program (POP): Ocean component of the Community Climate System Model (CCSM 2.0 and 3.0). Los Alamos National Laboratory Tech. Rep. LA-UR-02-2484, 75 pp. [Available online at <http://www.cesm.ucar.edu/models/ccsm3.0/pop/doc/manual.pdf>.]
- Sun, L. C., and Coauthors, 2010: The data management system for the Global Temperature and Salinity Profile Programme (GTSP). *Proceedings of the OceanObs 2009: Sustained Ocean Observations and Information for Society (Vol. 2)*. 2009, Venice, Italy, ESA Publication, doi:10.5270/OceanObs09.cwp.86.
- Sverdrup, H. U., and R. H. Flemming, 1941: *The Oceans: Their Physics, Chemistry, and General Biology*. Prentice Hall, 1087 pp.
- Talley, L. D., G. L. Pickard, W. J. Emery, and J. H. Swift, 2011: *Descriptive Physical Oceanography an Introduction*, sixth edition. Elsevier Inc., 555 pp.
- Third Fleet, 2016: Commander, U.S. Third Fleet: Home page. Accessed 26 April 2016. [Available online at <http://www.c3f.navy.mil/>.]
- Thomas, A. C., and P. T. Strub, 2001: Cross-shelf plankton pigment variability in the California Current. *Continental Shelf Research*, **21**, 157–1190.
- Watson, G. W., and N. W. Casey, 2007: Sampling biases in MODIS and SeaWiFS ocean chlorophyll data. *Remote Sensing of Environment*, **111**, 25–35.
- World Ocean Database (WOD), 2016: World Ocean Database NOAA/NCEI. Accessed 11 2016. [Available online at [https://www.nodc.noaa.gov/OC5/WOD/pr\\_wod.html](https://www.nodc.noaa.gov/OC5/WOD/pr_wod.html).]
- World Ocean Atlas Database (WOA), 2016: World Ocean Atlas 2013 version 2 NOAA/NCEI. Accessed 11 2016. [Available online at <https://www.nodc.noaa.gov/OC5/woa13/>.]
- Weng, H, S. K. Behera, and T. Yamagata, 2009: Anomalous winter climate conditions in the Pacific Rim during recent El Nino Modoki and El Nino events. *Climate Dynamics*, **32**, 663–674. doi:10.1007/s00382-008-0394-6.
- Wolter, K., and S. Timlin, 1998: Measuring the strength of ENSO events: How does 1997/98 rank?. *Royal Meteorological Society*, **53**, 269–324.



## **INITIAL DISTRIBUTION LIST**

1. Defense Technical Information Center  
Ft. Belvoir, Virginia
2. Dudley Knox Library  
Naval Postgraduate School  
Monterey, California